ORSAY
N°D'ORDRE: 8367

Université d'Orsay

École doctorale Rayonnement et Environnement

Beam Orbit Control in TESLA Superconducting Cavities from Dipole Mode Measurements

by:

RITA PAPARELLA

Soutenue le 22 Septembre 2006 dans le Grand Amphithêatre de l'INSTN devant la commission d'examen:

WITTENBERG KAY
BAMBADE PHILIP
BABOI NICOLETA
NAPOLY OLIVIER
DEBU PASCAL

2003-2006

To my brother, Emanuele. My best wishes for a future full of great opportunities. I'm fond of you.

Abstract

The electron–positron collider ILC in its baseline version should reach a center–of–mass energy of 500 GeV, five times higher than the SLC, the first and only linear collider built at SLAC, and 2.5 times higher than LEP. The luminosity of ILC, a measure for event rate a collider can deliver, is about 1000 times higher than that of LEP at 200 GeV. Both, energy and luminosity are prerequisites for new discoveries. In a second phase, by adding more cooling and radiofrequency power the energy range of the ILC could be extended to about 1 TeV without increasing the length of the machine. In addition, with some modifications, the ILC could be operated with high luminosity at lower energies, between 90 and 200 GeV center–of–mass energy.

The knowledge of the electromagnetic interaction between a beam and the surrounding vacuum chamber is necessary in order to optimize the accelerator performance in terms of stored current. Many instability phenomena may occur in the machine because of the fields produced by the beam and acting back on itself. Basically, these fields, *wake–fields*, produce an extra voltage, affecting the longitudinal dynamics, and a transverse kick which deflects the beam.
In this thesis we present the results of theoretical and experimental investigations to demonstrate the possibility of using the dipolar wake fields of the superconducting accelerating to measure the beam transverse position.

After an introduction to the ILC project and to the TESLA technology, of superconducting RF cavities, we will approach the problem from an analytical point of view in chapter 2. The expression of the wake fields in a cylindrical cavity will be investigated and the electromagnetic field modes derived from Maxwell's equations in an original way. Graphical solutions of a Matlab program simulating the fields due to a particle passing through a pill-box cavity along a generic path will be shown.

The interaction of the beam with higher order modes (HOM) in the TESLA cavities has been studied in the past at the TESLA Test Facility (TTF) in order to determine whether the modes with the highest loss factor are sufficiently damped. Starting from the results obtained before 2003, HOM signals has been better observed and examined in order to use dipole modes to find the electric center of each cavity in the first TTF accelerating module. The results presented in chapter 3 will show that by monitoring the HOM signal amplitude for two polarizations of a dipole mode, one can measure electrical center of the modes with a resolution of 50 μm. Moreover, a misalignment of the first TTF module with respect to the gun axis has been predicted using cavity dipole modes.

Alternatives to this method are described in the last chapter. A time domain HOM data acquisition setup has been conceived at SLAC and fabricated with the additional help of DESY and CEA. The beam has been moved by pairs of correctors for each transverse plane by using a system capable of monitoring simultaneously one dipole mode from all 40 cavities at TTF. HOM signals have been used for beam position monitoring and alignment, and cavity relative misalignments in the cold modules has been measured. The results of this study, prove the benefit and the usefulness of using dipole modes as beam position monitor and to provide a cross–check of the mechanical measurements.

Contents

List of Figures

List of Tables

Chapter 1

Introduction

1.1 General introduction and motivation

Accelerators are of fundamental importance in building our picture of nature at the level of its smallest constituents. Accelerators have provided the experimental evidence that supports the Standard Model presently accepted as the basis of our understanding of particle physics.

According to the Standard Model, matter is composed of few elementary particles, leptons and quarks. The interactions among these are mediated by force-carrying particles. The electromagnetic force is unified at high energies with the weak force into the electroweak interaction. Nevertheless, some prediction of this model remain to be proved. It is hoped that future particle accelerators will provide the tool to answer some of these questions. Among these is the so-called Higgs mechanism that could explain the observed masses of the $W_{\pm}$ and Z_0 intermediate vector bosons, as well as those of the elementary fermions. Based on the successful unification of the electric and magnetic forces, and of these with the weak interaction, it is believed that at higher energies the electroweak force is unified with the strong force. The favored theory implies the existence of a super-symmetric partner of each matter and force-carrying particle.

So far, circular colliders were the main tool in experimental particle physics. Currently under construction is the Large Hadron Collider (LHC) at CERN, a proton-proton storage ring with 14 TeV center-of–mass (c.m.) energy, which will produce collisions in 2007 in order to investigate these questions.
Circular e^+e^- colliders become inefficient at energies higher than that of LEP, 200 GeV c.m., due to synchrotron radiation which is emitted by charged particles traveling on a curved trajectory. The energy loss per revolution is proportional to the fourth power of the energy divided by the rest mass and inversely proportional to the trajectory radius. The amount of radiated power is therefore much higher for electrons than for heavier particles.The solution is to build linear colliders. An electron-positron linear collider with energies up to 1 TeV c.m. is nowadays considered to be the next step for experimental studies in particle physics. But the advantage of circular accelerators of using an injected beam many times at a very high collision rate is lost. Therefore one has to use beams with many particle bunches in order to increase the collision rate.
In addition, the beam size at the interaction point (IP) must be extremely small, in the nanometer range, to achieve the required high interaction rate of the particles. In order to focus the bunches to these very small spot sizes over distances larger than the bunch length, very small *emittances* must be created and transported to the IP. The main source of emittance growth are the so called wake fields[1] that are excited by charged particles in the interaction with their environment, typically the accelerating structures, and act on the following particles. One can distinguish between longitudinal effects, mainly an increase in the energy spread, from transverse ones, specifically an increase in the transverse emittance. In fact, if the accelerator structures are "perfectly" aligned on the beam trajectory there is no transverse emittance growth. Thus, controlling the transverse emittance involves taking in account the alignment of the structure to minimize the transverse wake fields.

---

[1] wake fields can be decomposed in the higher order modes (HOM), resonant electromagnetic fields.

Longitudinal wake fields vary approximately with the second power of the accelerator frequency, while the transverse ones scale with the third power (see section 2.4.3). For this reason, lower RF frequency accelerators are preferable in order to preserve small emittances[2], leading to a higher luminosity. For the TESLA technology, i.e. superconducting cavities of 1.3 GHz RF frequency, this advantage of the lower frequency combines with the higher efficiency, due to the superconducting technology used, to give the higher luminosity.
This thesis deals with the study of the dipolar Higher Order Modes (HOM) of TESLA cavities, and with demonstrating their use in measuring cavity misalignment and in controlling the beam orbit inside the modules of the TESLA Test Facility (TTF) linac.

1.2 The linear collider approach

The development of the accelerators started about eighty years ago, and has since been advanced by many new ideas and technologies which extended the attainable energy by a factor of around 10 every decade.
This development of accelerators has led to important applications in many

---

[2] The oscillation amplitude of the bunch tail relative to the bunch head is characterized by the dimensionless growth parameter:

$$\Upsilon = -\frac{N r_0 W_{\perp,1} L_0}{4 k_\beta \gamma L} \ , \tag{1.1}$$

where L_0 is the total linac length, $W_{\perp,1}$ is here the transverse wake function (for the definition see 2.4.2) for one cavity period, r_0 is the classical radius of the particle, L is the cavity period, N the number of particles, k_β the betatron wave number and γ the relativistic number. For short bunches, $W_{z,1} < 0$, the parameter Υ is positive.
To preserve the beam emittance it is necessary to have $|\Upsilon \mathbf{\hat{y}}| \ll$ transverse beam size, where $\widehat{y}$ is the unit transverse vector [Cha93]. This means the beam must be injected on the linac axis with an accuracy better than a fraction of a per cent of the beam size, which is difficult to achieve. The beam acceleration has an important stabilizing effect because, as its energy increases, the beam becomes more rigid and less vulnerable to the wake fields.

fields of science including solid state physics, chemistry and biology. Especially electron storage rings are used for modern research: today they may be considered the most important spin–off of particle physics.

The most powerful accelerator concept to reach high energies is that of colliders, in which elementary particles are made to collide head–on. Among existing facilities, electron–positron colliders are considered as precision tools for particle physics. Since electrons and their anti–particles, the positrons, are elementary point–like particles, they annihilate each other in the collision. The resulting center of mass (c.m.) energy is converted into new particles. The properties of these new particles are measured in the detectors surrounding the interaction point. These features were essential for many discoveries made with electron–positron colliders, including new quarks and leptons and the particle mediating the strong interaction, the gluon, as well as for precision tests of the Standard Model.

Except for the Stanford Linear Collider (SLC), electron–positron colliders have so far been built as storage rings. However, the only way to reach electron energies substantially above 200 GeV c.m., achieved by LEP, is by accelerating electrons and positrons on a straight line. Each linear accelerator consists of a large series of electromagnetic radiofrequency resonators (cavities), which generate the required electric fields to accelerate the electrons and positrons.

A major challenge for all linear collider concepts is to obtain a large luminosity of electrons and positrons at the interaction point. This requires very small spot sizes of the beams at the collision point and high beam powers. In 1997 the feasibility of the concept has been demonstrated by the successful operation of the Stanford Linear Collider at its design luminosity and a c.m. energy of 92 GeV.

Over the past decades, several groups world–wide have been pursuing different linear collider concepts. Already in 1971 a group at the Institute of Nuclear Physics in Novosibirsk started detailed design work for a linear collider of several hundred GeV, addressing many of the relevant problems. Several years later, groups at CERN, at the Stanford Linear Accelerator Center (SLAC) in California, and the Japanese National Laboratory for High Energy Physics (KEK) in Tsukuba began work on linear collider designs. All these concepts were based on normal–conducting copper cavities.

The TESLA approach differs from the other designs by the choice of superconducting accelerating structures as its basic technology. As will be shown, the TESLA linear collider based on superconducting accelerating structures is well suited to meet the requirements needed for a large luminosity, namely very small beam sizes and high beam power. The advantage of the superconducting technology, has been acknowledged from the very beginning of the research and development on linear colliders, but the technology was considered to be more expensive than conventional technologies and not suited for high accelerating gradients.

By a focused development program started in 1992, by the international TESLA collaboration in co–operation with industry, a prototype superconducting linear accelerator was built, the TESLA Test Facility (TTF), in order to gain long term operating experience and costing knowledge. As a result superconducting RF cavity structures capable of generating gradient over 30 MV/m, five times larger than before 1990, were developed, and a reduction of the cost per meter of accelerator by a factor of four was achieved, leading to about 2 k€/MV cost of accelerating cryomodules.

The development of linear accelerators for particle physics has also led to an ideal accelerator for a light source with completely new properties: an X–ray Free–Electron Laser (XFEL) producing X–rays with true laser properties, as first proposed by the Stanford Linear Accelerator project LCLS, and then by the XFEL project at DESY. The photon emission is based on SASE: the laser light is generated when electrons travel through an ondulator magnet structure, after having been linearly accelerated to provide electron beams of the necessary quality. Using the TESLA Test Facility accelerator, laser light was generated for the first time in the wavelength range from 180 nm to 13 nm. This was a first proof of principle that such an X–ray laser can be built and has stimulated intense activities in the field of X–ray FELs world–wide.

Summarizing the work of the past decade the following milestones in accelerator technology and development have been reached:

- Superconducting cavities exceeding an accelerating gradient of 30 MV/m are being produced by industry, thus fulfilling the needs for a 500 GeV c.m. collider.

- Using a new surface treatment, gradients greater than 40 MV/m have been reached in single cell cavities, giving access to energies of 1 TeV.

- The Free-Electron Laser based on SASE principle has been demonstrated at wavelengths of 13-180 nm.

- Other technology challenging components needed for the accelerator, like high–power, high efficiency multi–beam klystrons, and high power input couplers have successfully been developed, built and operated at the TESLA Test Facility.

1.3 The ILC project

On the 20th August 2004, the International Technology Recommendation Panel (ITRP) recommended that the International Linear Collider (***ILC***) should be based on the 1.3 GHz superconducting RF technology developed by the TESLA Collaboration. This recommendation has been endorsed by the International Committee for Future Accelerators, ICFA. Laboratories and research groups around the world are now committed to the ILC as their next big project for elementary particle physics.

An electron-positron annihilation is a very well defined physical process. This explains the key role electron-positron colliders have played in the past for the progress of particle physics. Most of these advantages stem from the following three unique strengths:

- A well defined initial state: this means that one knows that the interaction originates from an $e^{-}e^{+}$ annihilation at a precise energy. In the case of the ILC one can in addition define the spin alignment (the polarization) of the initial particles, providing a powerful discrimination on electroweak interactions which depend crucially on this alignment.

- Comparable rates for standard physics and new physics. Higgs production for example has a rate comparable to other process with the same final state topology.

- Very favorable environment for measurements. Backgrounds are expected to be low. Particles can be observed very close to the collision point, allowing for excellent precision on the decay points of particles with long lifetimes. The final states of most events can be completely reconstructed.

A sketch of the overall layout of the ILC linear collider is shown in figure 1.1. The electron beam is generated in a polarized laser–driven gun. After a short section of conventional linac, the beam is accelerated to 5 GeV in superconducting structures identical to the ones used for the main linac. The baseline design assumes that the electrons are stored in a damping ring of about 6 km circumference.
The positron injection system has to provide a total charge of about $5 \cdot 10^{13} e^{+}$ per beam pulse, which is not realistically feasible with a conventional (electron on thick target) source. Instead, positrons are produced from γ–conversion in a thin target, after which they are preaccelerated in conventional 200 MeV L–band linac, followed by a 5 GeV superconducting accelerator. The photons are generated by passing the high–energy electron beam through an undulator.
The undulator–based positron source requires an electron beam energy greater than 150 GeV for full design positron beam intensity. At center–of-mass energies below 300 GeV the luminosity is reduced due to a lower positron beam current. If lower energy running at maximum luminosity becomes important,

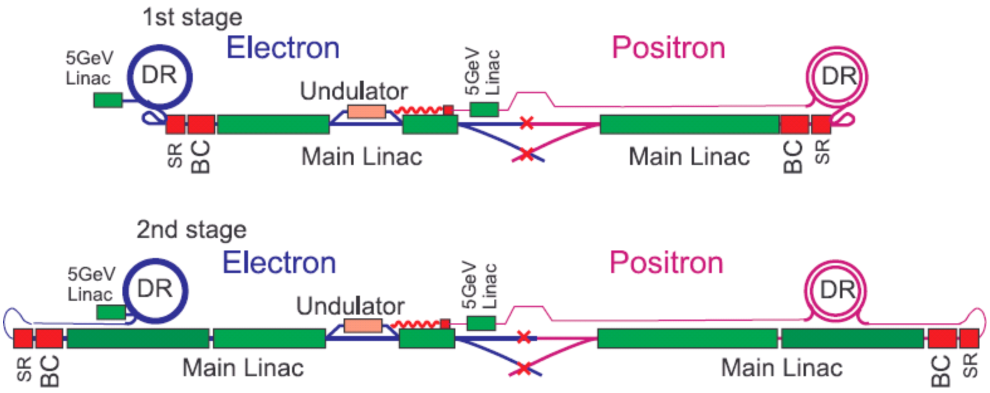

Figure 1.1: Sketch of the overall layout of ILC: 1^{st} stage 500 GeV c.m. energy; 2^{nd} stage 1 TeV c.m. energy.

additional electron beam pulses and bypass–beamlines are foreseen to drive the positron source independently from the (lower–energy) beam used for physics.
Each main linear accelerator is made of roughly ten–thousand one–meter long superconducting cavities. Group of eight cavities are installed in a common cryostat (cryomodule); the current design is based on that used in the TTF linac, modified to be more compact and cost–effective. The cryomodules also contain superconducting magnets for beam focusing and steering, beam position monitors, and high-order mode absorbers [fig. 1.2].
The **RF**–power is generated by one 10 MW klystron powering three modules (24 cavities).
The beam transport between the linac and the IP, the so–called beam delivery system, consists of collimation, beam diagnostics chromatic correction, and final focus sections.

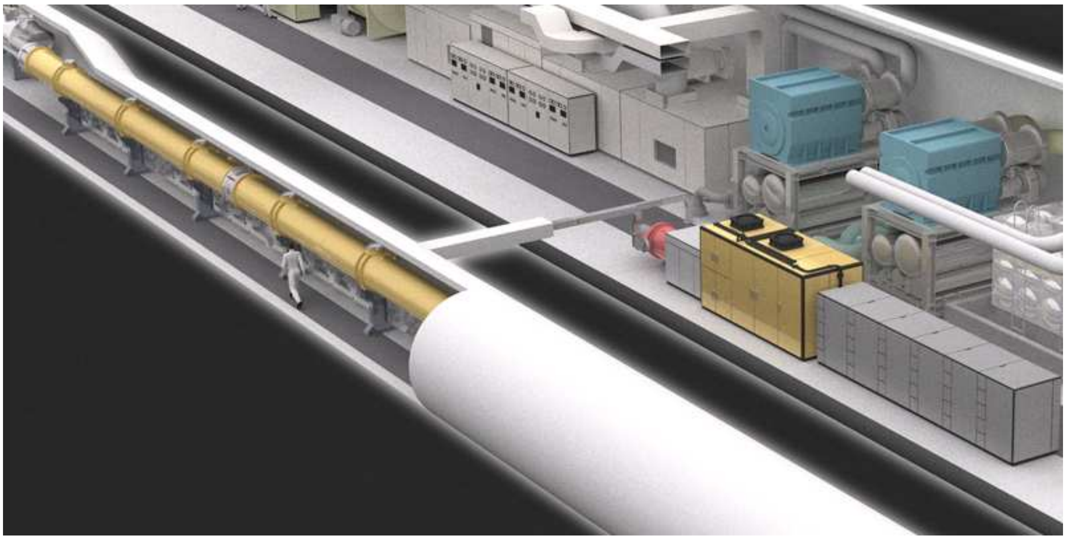

Figure 1.2: Sketch of the 5 m diameter ILC linac tunnel, and klystron and modulator hall.

The choice of superconducting RF also allows one to use a long RF–pulse (1 ms) allowing to accelerate a large number of bunches (2820) with a relatively large bunch spacing (308 ns at $E_{cm} = 500$ GeV). Three benefits result directly from this long bunch train:

- A fast (MHz) bunch-to-bunch feedback can be used to correct the orbit within one beam pulse. Such a feedback system will maintain the beams in collision at the IP, making ILC relatively insensitive to mechanical vibrations of focusing elements which could otherwise lead to serious luminosity reduction.

- In the event of an emergency, a fast safety system can "turn off" the beam within a fraction of a pulse.

- A moderate peach RF power of about 350 kW per cavity entirely converted into beam energy leading to a high efficiency acceleration.

1.4 ILC Parameters for 500 GeV c.m.

The ILC design accelerating gradient at $E_{cm} = 500$ GeV is $E_{acc} = 31.5$ MV/m and the quality factor[3] $Q_0 = 10^{10}$. Thanks to the small dissipated power in the cavity walls, a high average beam power (2×10 MW) can be accelerated while keeping the electrical power consumption within acceptable limits (100 MW). Besides the center–of-mass energy of the colliding beams, a second key parameter for a linear collider is the luminosity L, given by:

---

[3] The quality factor is defined as:

$$Q_0 = \frac{\omega U}{P_{dissipated}} \ ,$$

where ω is the modes frequency, U is the stored energy in the electromagnetic field and $P_{dissipated}$ the power dissipated in the walls.

$$L = \frac{n_b N_e^2 f_{rep}}{4\pi\sigma_x^*\sigma_y^*} \tag{1.2}$$

where

n_b number of bunches per pulse
N_e number of electrons (positrons) per bunch
f_{rep} pulse repetition frequency
$\sigma_{x,y}^*$ horizontal (vertical) beam size at interaction point

Introducing the average beam power $P_b = E_{cm} n_b N_e f_{rep}$, the luminosity can be written as:

$$L = \frac{P_b}{E_{cm}} \times \frac{N_e}{4\pi\sigma_x^*\sigma_y^*} \times H_D \tag{1.3}$$

An important constraint on the choice of IP parameters is the effect of beamstrahlung: the particles emit hard synchrotron radiation in the strong electromagnetic space-charge field of the opposing bunch. The average fractional beam energy loss from beamstrahlung is approximately given by [Che91]:

$$\delta_E \approx 0.86 \frac{r_e^3 N_e^2 \gamma}{\sigma_z(\sigma_x^* + \sigma_y^*)^2} \tag{1.4}$$

where

r_e the classical electron radius
γ relativistic factor E_{beam}/m_0c^2

Beamstrahlung causes a reduction and a spread of the collision energy and leads to background in the detector. The energy loss δ_E is therefore limited typically to a few percent. By choosing a large aspect ratio $R = \sigma_x^*/\sigma_y^* >> 1$, δ_E becomes independent of the vertical beam size and the luminosity can be increased by making σ_y^* as small as possible. Since $\sigma_y^* = 1/2 \approx \sqrt{(\epsilon_{y,N}\beta_y^*/\gamma)}$, this is achieved by a small vertical beta function at IP (β_y^*) and a small normalized vertical emittance ($\epsilon_{y,N}$). The lower limit on β_y^* is given by the bunch length ('hourglass effect'); setting $\beta_y^* = \sigma_z$, the luminosity can be expressed as:

$$L \approx 5.76 \cdot 10^{20} m^{-3/2} \times \frac{P_b}{E_{cm}} \times \left(\frac{\delta_E}{\epsilon_{y,N}} \right)^{1/2} \times H_D \qquad (1.5)$$

As a consequence, to achieve the desired high luminosity, with a limited power and energy loss, bunches with small vertical emittances are required.

In high energy linear accelerators, the particles grouped in bunches gain energy in accelerating structures and are transversally focused by magnetic quadrupoles. In addition, one needs steering magnets to correct for the misalignments of various components and diagnostics elements such as beam position monitors in order to measure the properties of the beam.
The primary sources of transverse emittance dilution are the transverse wake fields excited in the accelerating sections in the presence of misalignments, and the dispersive errors caused by the focusing magnets. If the wake fields are too strong, they can degrade the quality of the beam by increasing its energy spread and transverse emittance. The longitudinal and transverse wake fields per unit length of accelerator scale approximatively as f^2 and f^3 respectively (see section 2.4.3): hence the wake fields in the ILC ($f = 1.3$ GHz) are considerably weaker compared to those of machines based on S–band ($f = 3$ GHz) or X–band ($f = 11.4$ GHz) technologies.
For ILC, the low RF frequency and corresponding large irises of the accelerating structures result in much smaller wake field kicks for a given misalignment than in higher frequency room-temperature designs. Furthermore, a given residual magnetic dispersion generates less emittance blow–up, because the beam energy spread is kept small along most of the accelerator.
The relatively low frequency of the ILC linac is ideally suited for accelerating and *conserving* ultra-small emittance beams.
The small wake fields and low energy spread ultimately result in relatively

relaxed alignment tolerances for the various components (focusing magnets, beam position monitors, accelerating structures), for which modern optical survey techniques are sufficient.

Table 1.1 lists all important ILC linac parameters relevant to beam dynamics issues.

	ILC collider
Accelerating gradient $E_{acc}[MV/m]$	31.5
Injection energy $E_i[GeV]$	5
Bunch charge $N_e[10^{10}]$	2.0
Bunch spacing $\Delta t_b[ns]$	308
Bunch length $\sigma_z[\mu m]$	300
Norm. design emittance $\epsilon_x, \epsilon_y[10^{-6}m]$	9.6, 0.04
Norm. emittance at injection $\epsilon_x, \epsilon_y[10^{-6}m]$	8, 0.02
Beam size at injection $\sigma_{x,i}, \sigma_{y,i}[\mu m]$	320, 16
Beam size at linac exit $\sigma_{x,f}, \sigma_{y,f}[\mu m]$	30,1
Initial uncorr. energy spread $\sigma_{E,i}/E[\%]$	2.5
Off–crest RF phase Φ_{RF} [°]	5
Correlated energy spread $\delta_{cor}[10^{-4}]$	3
Total spread $\sigma_{E,f}/E$ at linac exit $[10^{-4}]$	6

Table 1.1: Overview of beam parameters in the main linac

1.5 Overview of the Tesla Test Facility linac

The major challenge for the TESLA collaboration was to prove the feasibility and reliability of accelerating gradients well above 25 MV/m, i.e. high enough for the 500 GeV linear collider. The TTF linac at DESY Hamburg was constructed to show that the high gradients achieved in cavity tests, could be maintained during the assembly into a linac test string, and then successfully operated with auxiliary systems to accelerate an electron beam to a few hundreds MeV. The basic characteristics of the TTF linac were designed to be as consistent as possible with the parameters of the TESLA design. The original proposal for the TTF was for a linac test string of four cryogenic modules, each containing eight superconducting 9–cell TESLA structures. The initial goal was 15 MV/m, which was at that time substantially higher than superconducting cavities operated at other accelerator laboratories. Shortly after finishing the first design of the TTF linac, it became clear that the test linac would be almost ideal to drive a Free Electron Laser (FEL) based on the principle of the Self Amplified Spontaneous Emission (SASE): therefore, the overall layout was changed e.g. introducing a two–stage bunch compression in order to increase the peak current, and the FEL became part of the TTF project (see Fig. 1.3).

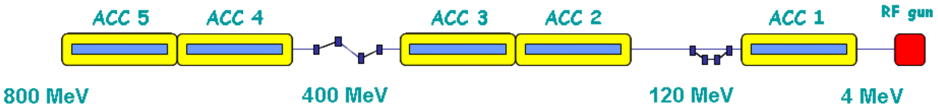

Figure 1.3: Schematic layout of Tesla Test Facility phase 2 linac.

The TTF linac program for the accelerator modules was planned to check many of the aspects of the operation in the linear collider:

- gradient achievable in a standard linac module;
- input coupler and Higher Order Modes (HOM) coupler performance;
- RF control of multi–cavity systems;
- Lorentz force detuning and microphonic noise effects;

- RF conditioning of cavities and couplers;
- vacuum performance / failure recovery potential;
- cryostat design and cryogenic operation / heat load;
- dark current;
- energy and beam position feedback control;
- diagnostic;
- bunch compression;
- alignment and emittance preservation.

In its present set-up, the test facility linac consists of the following sections:

- a RF photo–injector;
- five accelerator modules;
- two bunch compressor sections;
- a collimator section;
- three undulators;
- a high energy beam analysis area / photon beam diagnostics.

The injector area includes the electron gun, focusing lenses, and beam steerers. The TTF linac comprises five cryomodules, each 12.2 m in length. Each cryomodule contains eight 9–cell cavities, a superconducting quadrupole–steerer doublet, and a cold cavity type beam position monitor. Each accelerating cavity has an input coupler for RF power, a pickup antenna to measure the cavity field amplitude and phase, two HOM damping couplers,

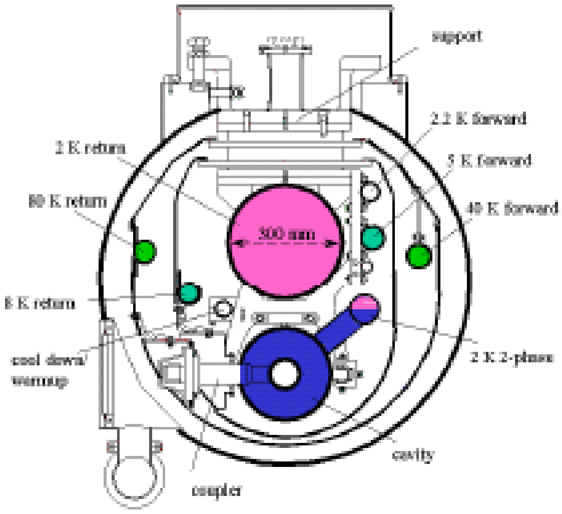

Figure 1.4: Cross section of cryo-module

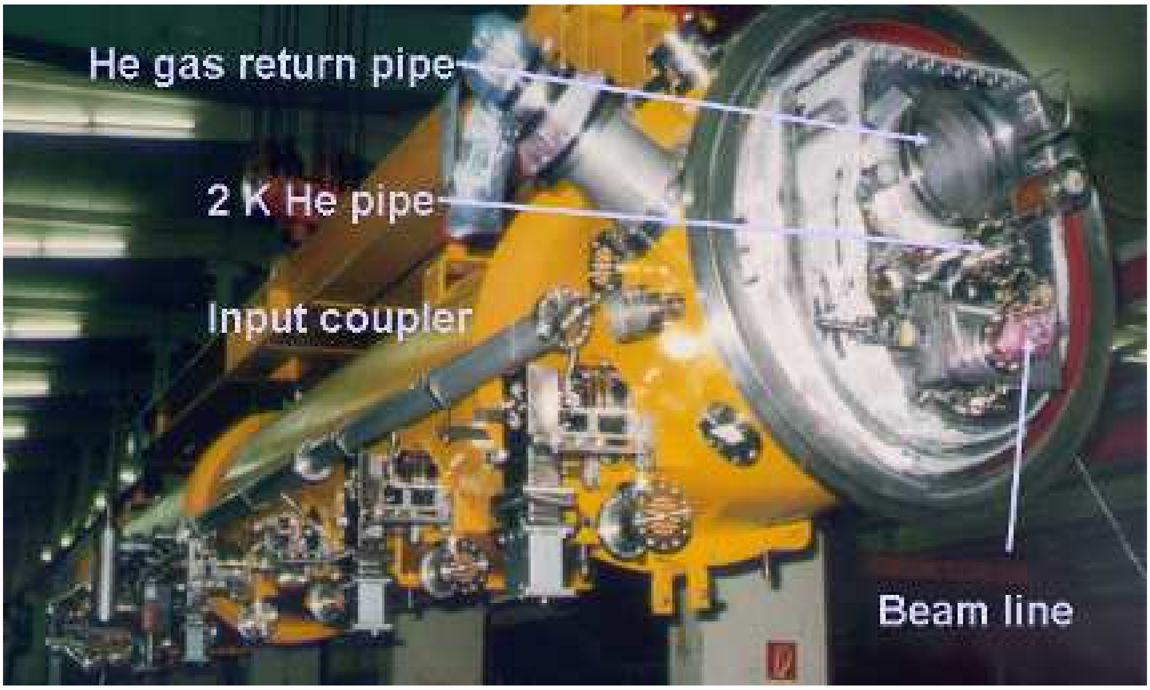

Figure 1.5: TTF Cryo-module

and a frequency tuning mechanism (Figs. 1.5, 1.4).

Recently, stimulated by the users of the FEL and the first exciting results obtained, the suggestion was made to find a compact name for the TTF/VUV–FEL facility which is more attractive and easier to pronounce in different languages. On April 6^{th}, 2006, the DESY Directorate decided for the new name: FLASH, standing for **F**reie–Elektronen–**LAS**er in **H**amburg, or equivalent in other languages.

1.6 Design of the TESLA cavities

The TESLA cavities are RF structures of 9–cell niobium resonators, of 1 m length, (fig. 1.6) cooled by superfluid Helium to 2 K and operating at L–band frequency (1.3 GHz).

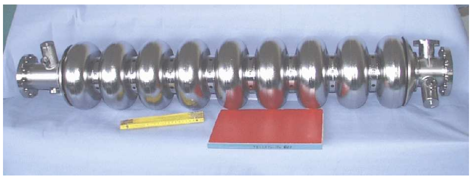

Figure 1.6: The 9–cell niobium TESLA cavity.

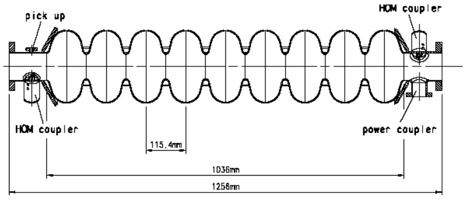

Figure 1.7: Side view of 9–cell cavity with the main coupler port and two higher–order mode couplers

Each of the eight cavities of each module is incased in a titanium helium vessel. The accelerating field is carried by the fundamental TM mode with a frequency of 1.3 GHz, which is powered by a coaxial input coupler in a standing wave pattern (see Fig. 1.7). The cavity iris diameter is 7 cm, inversely proportional to the RF frequency. To adjust the fundamental frequency, a mechanical tuning system driven by a stepping motor is mounted to the vessel.

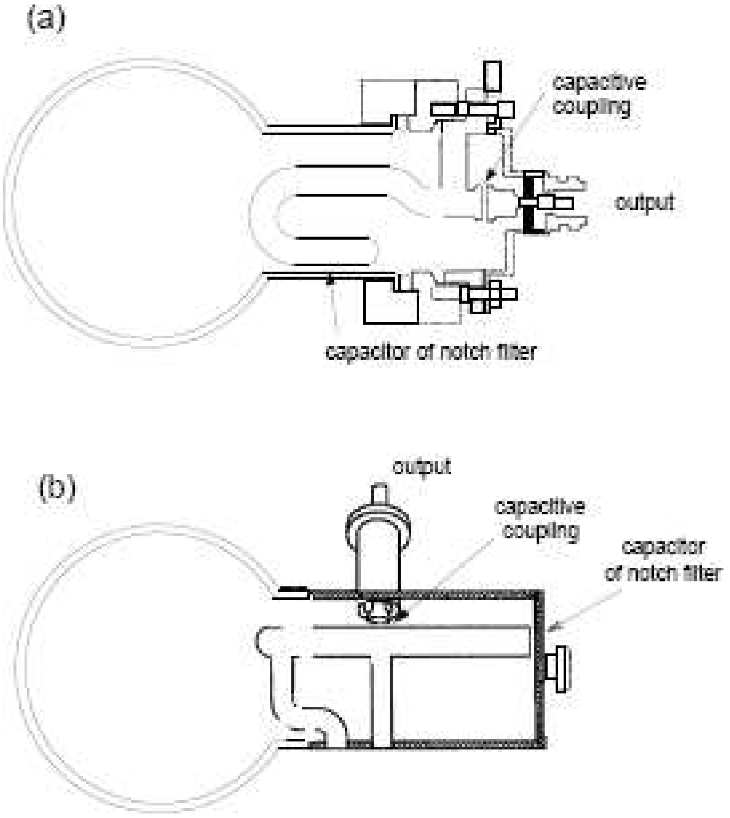

Figure 1.8: HOM couplers installed at either side of the TESLA cavities (courtesy N. Baboi). Two types are used at the TTF cavities: (a) a demountable Saclay type and (b) a welded DESY type.

One of the primary sources of transverse emittance dilution in the TESLA modules are the transverse wake fields of higher frequency modes excited in the accelerating cavities by long trains of intense bunches. These higher–order modes must be damped to avoid multi–bunch instabilities and beam breakup. The lower the quality factors Q (see the definition at section 2.6.2) of the HOMs the lower the amplitude of the fields will be which are excited by the bunch train. The quality factor of the HOMs are reduced by HOM couplers, which are mounted on the beam pipes at both ends of each TESLA cavity (Figs. 1.7, 1.8). To damp not only monopole and dipole but also quadrupole modes and modes of even higher azimuthal order, the angle between two HOM couplers of one cavity is chosen as 115°. Another problem might arise from ”trapped modes”, which are concentrated in the center cells and have low field amplitudes in the end cells and therefore are badly coupled to the HOM dampers. By an asymmetric shaping of the end cells, the field of some of these modes is enhanced at one or both of the cavity ends.

Most losses occur at low frequencies, where the conductivity of the superconducting surface is several orders higher than that of normal conducting walls. Part of this power is extracted by input– and HOM–couplers, but high frequency fields propagate along the structure and are reflected at normal and superconducting surfaces. In order to reduce the losses at 2 K and 4 K, a special HOM absorber operates at 70 K, where the cooling efficiency is much higher. The absorber basically consists of a pipe of absorbing material mounted in a cavity–like shielding, and integrated into the connection between two modules.

1.7 Thesis purpose, motivation and overview

Controlling beam alignment in the cavities is important in order to avoid transverse kicks on the beam from the dipolar HOMs, which may lead both to a single–bunch deformation and to beam break–up along the bunch train. The same HOM signals can be used to monitor the offset of the beam with respect to the cavity axis, since their amplitude is proportional to it. To improve the alignment tolerances for the collider, and the XFEL, the beam–based method should achieve a centering resolution significantly better than 500 μm obtained by the cavity mechanical alignments.

This thesis aims at demonstrating the potential of using the dipole signals for measuring the cavity alignment in the cryo–modules and monitoring the beam position in the cavities.

The principle of measuring the beam position with respect to the electric axis of a cavity by the detection of the beam generated dipole modes is not new. RF beam position monitors are based on this principle.
Using dipole modes generated in the X–band accelerating structures was also foreseen in the warm collider designs, like NLC at SLAC and JLC at KEK, to align the structures at the micrometer level and reduce the wake fields.

The difficulty for the TESLA cavities comes from two factors:

- The mechanical tolerance for the cavity construction, and particularly the relative position of the nine cell centers, is of the same order of magnitude, $\sim 400\ \mu m$ r.m.s., as the tolerance (Table 1.2) for the global alignment of the cavities in the cryo-modules. Therefore the "beam–based alignment" (i.e. cavity misalignment observation by using the beam trajectory as reference axis and the dipole modes as high resolution signal, with a better precision than that provided by the mechanical alignment) is subject to a basic difficulty since the position of the electric axis of the cavities, corresponding to a zero–amplitude signal is as badly known as the position of the cavities themselves.

- The dipole mode polarization planes are also unknown, because of the imperfections of the axial symmetry of the cavities. In comparison, a cavity BPM for the beam position monitors based on RF cavities, where this planes are fixed by the position of the RF antennas and correspond usually to the horizontal and vertical planes.

The general purpose of this thesis is to show that, despite these two difficulties, the dipole modes can be used to monitor the beam position with a resolution better than the mechanical alignment. This in turn opens the possibility to use the beam signal to probe the alignment tolerances in the cryomodules as well as the cryomodule alignment, by using the beam axis as

Alignment Tolerances	
Quadrupole postion	$\sigma_{quad} = 300\ \mu$m
Cavity position	$\sigma_{cav} = 300\ \mu$m
Cavity angle (pitch)	$\sigma'_{cav} = 200\ \mu$rad
BPM position	$\sigma_{bpm} = 200\ \mu$m
BPM resolution	$\sigma_{res} = 10\ \mu$m
Cryomodule position	$\sigma_{module} = 200\ \mu$m

Table 1.2: Tolerances for the cavity alignment (r.m.s.) for the ILC design.

a reference.

The knowledge of the electromagnetic interaction between a beam and the surrounding vacuum chamber is necessary in order to optimize the accelerator performance in terms of stored current, emittance, luminosity, and then, as it will be shown in this work, beam diagnostics and alignment.

In the first part of this thesis, analytical approaches to the problem will be described. The aim is a better understanding of the response of the electromagnetic field, due to the passage of the beam inside a cavity, with wake fields propagation. The wake field of a bunch of charged particles traversing a resonant cavity is of great interest for particle accelerators and storage rings, as it permits calculating the coupling impedance as well as the evaluation of the energy loss of the bunched beam. The only geometry which permits exact analytic calculations of the wake fields is the closed cylindrical cavity, commonly called "pill–box". Several different approaches to calculate the electromagnetic modes and wake field of a bunch of particles traversing a pill–box cavity have been published in the literature, but we want to obtain these results by using an original method. Finally, the mode–analysis can be generalized to arbitrary cavities, for which the wake fields is obtained in terms of loss parameters of each of the resonant modes.

In the second part, the alignment of the beam through the cavities has been experimentally studied at TTF, using the HOM signals generated by the beam in the superconducting 9–cell TESLA cavities. The method consists of moving the beam in position and angle and monitoring selected dipole mode amplitudes with a spectrum analyzer. The beam is aligned when the signal is minimum with a resolution of the order of 50 μm.
The exact frequency values of each mode in all 40 TTF cavities have been found using a spectrum analyzer, and first studies on the possibility to align the beam in cavities have been made. Also first study on cavity eccentricities and modes polarizations, have been performed for the first accelerating cryomodule, and its large misalignment with respect to the gun has been discovered.

The third part of this thesis presents the experimental results on the monitoring of dipole modes by using an alternative data acquisition setup. A time–domain based waveform recorder system that captures information from each mode has been built at SLAC with the following properties:

- possibility of monitoring dipole mode amplitude and phase;
- monitored several modes at the same time;
- stored data from several cavities at the same time.

By steering the beam through the TTF cryomodules, the HOM signals are used to estimate the residual internal alignment errors of the cavities with a resolution about two orders of magnitude lower than that of cavity mechanical alignments.

Chapter 2

Analytical resolution model

2.1 The Accelerating gap

RF acceleration is obtained by creating a RF field inside one or more gaps of the vacuum chamber which is supposed to be metallic. These accelerating gaps can be obtained with two conceptually different devices:

- drift tubes
- cavity resonators

First we study the behavior of a gap (no matter how it is made). We make the hypothesis that the electric field E_z is uniform along the axis of the gap and depends sinusoidally on time t:

$$E_z = E_0 \ \cos(\omega t + \varphi) \ . \tag{2.1}$$

The phase φ is defined in such a way that the particle crosses the middle of the gap ($z = 0$) at $t = 0$. The voltage gain is then (Fig. 2.1):

$$V = E_0 \int_{-G/2}^{+G/2} \cos(\omega t + \varphi)\; dz\ . \tag{2.2}$$

Usually, for electrons, the energy imparted in a single pass is small compared with the kinetic energy of the particle. In this case we assume that the speed of the particle does not change during the transit. Consequently $z = \beta ct$ and Eq.(2.2) becomes:

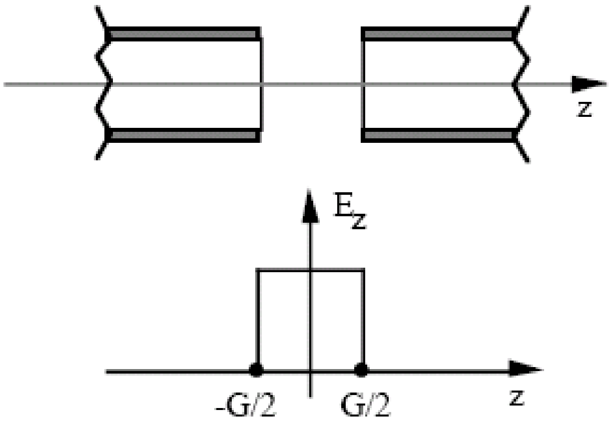

Figure 2.1: RF gap.

$$V = E_0 \int_{-G/2}^{+G/2} \cos\left(\frac{\omega z}{\beta c} + \varphi\right) dz = 2E_0\ \cos\varphi\ \frac{\sin\frac{\omega G}{2\beta c}}{\frac{\omega}{\beta c}}\ . \tag{2.3}$$

Rearranging we write:

$$V = E_0 G\ \cos\varphi\ \frac{\sin\frac{\omega G}{2\beta c}}{\frac{\omega G}{2\beta c}} = E_0 G \tau\ \cos\varphi\ , \tag{2.4}$$

where τ is the transit–time or gap factor.
Defining the transit angle $\theta = \frac{\omega G}{\beta c} = \frac{2\pi G}{\beta c T} = 2\pi \frac{G}{\lambda_p}$, where $\lambda_p = vT$ is the distance covered by the particle during one period T of the RF field, the transit–time factor becomes:

$$\tau = \frac{\sin \theta/2}{\theta/2} \ . \tag{2.5}$$

2.2 The drift tube: the synchronous condition

Schematically we can imagine that a portion of the vacuum chamber is replaced by a shorter tube which is connected with the RF voltage. In Fig.2.2 G is the gap length and L is the distance between the centers of the two gaps. If the free–space wavelength of the electric field is much larger than the physical length L–G, then we can assume that the whole drift tube has the same voltage. Consequently if the electric field in gap (1) is:

$$E_{z,1} = \frac{V_0}{G} \ \cos(\omega t + \varphi) \tag{2.6}$$

then in the gap (2) we have:

$$E_{z,2} = -\frac{V_0}{G} \ \cos(\omega t + \varphi) \ . \tag{2.7}$$

It is then evident that the energy gained by the particle passing through gap (1) will be doubled if and only if:

$$\frac{\omega L}{\beta c} = \pi \ . \tag{2.8}$$

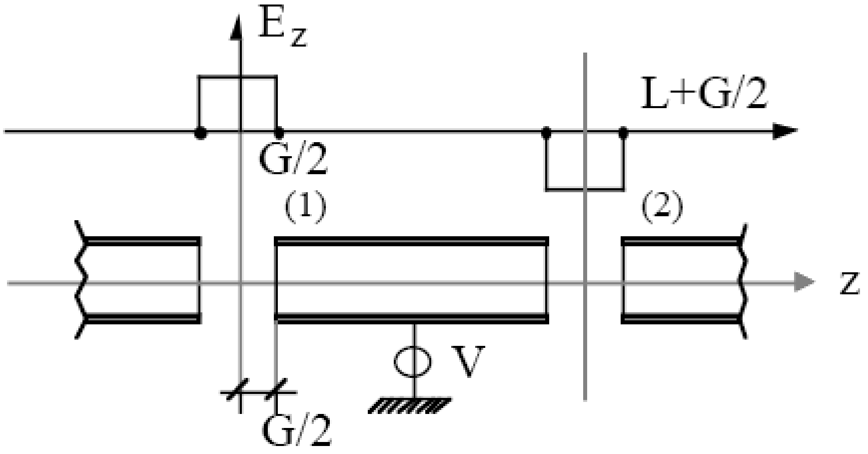

Figure 2.2: The physical length of the drift tube is L–G, while G is the length of each gap.

Nevertheless to find the effect of the drift tube, we proceed as in the previous case and evaluate the integral:

$$V = E_0 \left\{ \int_{-G/2}^{+G/2} \cos(\omega t + \varphi) dz - \int_{L-G/2}^{L+G/2} \cos(\omega t + \varphi) dz \right\} , \tag{2.9}$$

where $E_0 = \frac{V_0}{G}$ in Eq. 2.6.
Using the same substitution as above, $z = \beta c t$, and integrating, we obtain the general formula:

$$V = E_0 G \, \frac{\sin \theta/2}{\theta/2} \left[\cos\varphi - \cos\left(\varphi + \frac{\omega L}{\beta c} \right) \right] . \tag{2.10}$$

It is then confirmed that if $\frac{\omega L}{\beta c} = \pi$, then:

$$V = 2 E_0 G \tau \cos\varphi \ . \tag{2.11}$$

If $\lambda_p = \beta c T$ is the distance covered by the particle during one RF period, then the synchronism condition (2.8) becomes:

$$L = \frac{\lambda_p}{2} = \frac{\beta\lambda}{2} \ . \tag{2.12}$$

2.3 Cavity resonators

When calculating the electromagnetic fields in a completely enclosed cavity, we have to solve the field equations within the cavity for certain boundary conditions around its surface. A common approach is to expand the electric and magnetic fields in terms of orthogonal eigenfunctions of the Laplacian operator [Sla50].

These functions are solutions of the vacuum wave equations

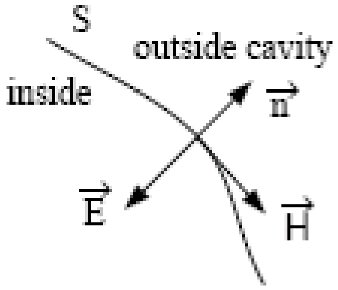

Figure 2.3: Boundary conditions at a perfect conducting surface S with outer normal **n**.

$$\left(\nabla^2 - \frac{1}{c^2}\frac{\partial^2}{\partial t^2}\right)\mathbf{E} = 0 \tag{2.13}$$

$$\left(\nabla^2 - \frac{1}{c^2}\frac{\partial^2}{\partial t^2}\right)\mathbf{B} = 0 \ , \tag{2.14}$$

satisfying the boundary conditions for a perfectly conducting cavity surface

$$\mathbf{n} \times \mathbf{E} = 0 \qquad \mathbf{n} \cdot \mathbf{B} = 0 \ . \tag{2.15}$$

Here **n** is the outer normal to the cavity surface S. Accordingly the electric field **E** has no tangential component over S, whereas the magnetic field **H** has no component parallel to **n**, see figure 2.3.

To solve the inhomogeneous problem of the electromagnetic field excited by a charged current, in a standard theoretical study, we would go, from the basis of the Maxwell equations, through the following steps (see also [Sla50] and [Lie01]):

- define a set of orthogonal eigenfunctions for the field in a cavity,
- expand the time dependent electric and magnetic fields in a cavity in terms of these eigenfunctions,
- use the Maxwell equations to find relations between the time dependent expansion coefficients.

But, in the fifth paragraph of this chapter, we will still focus on an alternative and novel resolution model.

2.4 Wake fields

The electromagnetic interaction of an intense charged particle beam with its vacuum chamber surroundings plays an important role for the beam dynamics and collective beam instabilities in an accelerator. When the geometry of the walls changes, the wall currents can not keep up with the bunch (middle in Fig. 2.4). A part of the electromagnetic field generated by the charge remains behind. When the beam tube narrows again (right), reflections of the field may occur. This constitutes the so–called *wake fields.* Another charge, following the first one, interacts with these fields, leading to a change in this energy or an orbit deflection. Thus, wake fields, generated by a moving particle in the accelerator pipe and objects such as RF cavities, bellows, monitors, etc., affect the motion of particles in the tail part of the beam causing the parasitic loss, beam energy spread, and instabilities. The effect of wake fields is usually of the same order of magnitude as the space charge effect. While the space charge forces approach zero in the ultrarelativistic limit, wake fields remain finite for an ultrarelativistic beam due to resistivity of the accelerator walls and non–smoothness of the chamber. The effect of wake fields is an increasingly important issue, since operating regimes are continually moving towards higher current and shorter bunches. To avoid collective beam instabilities that limit the accelerator performance, an accurate numerical modeling of wake fields and their interaction with the beam is necessary.

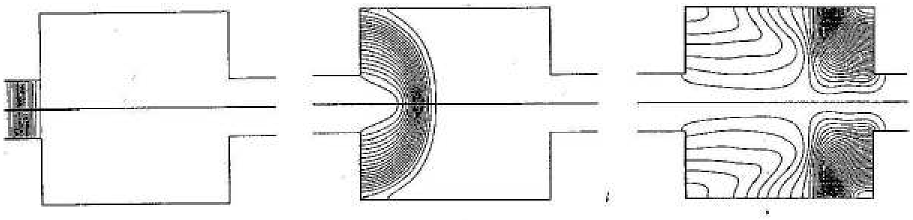

Figure 2.4: Wake field generation when a Gaussian bunch passes a change in geometry in the vacuum pipe. Three moments in time are shown.[By courtesy of N. Baboi]

In this section we show how the longitudinal and transverse wake fields can be calculated from the eigenmodes of the empty cavity. Historically a simpler, though less rigorous method, employing energy conservation arguments was first used to do the same thing ([Mor69], [Wat58]). The more direct method is employed here.

2.4.1 Overview on the normal mode expansion of fields in a cavity

The electric field $\mathbf{E}(\mathbf{x},t)$ and the magnetic induction $\mathbf{B}(\mathbf{x},t)$ can be written in terms of a vector potential $\mathbf{A}(\mathbf{x},t)$ and a scalar potential $\Phi(\mathbf{x},t)$ (in mks units) as:

$$\begin{cases} \mathbf{B} = \nabla \times \mathbf{A} \\ \mathbf{E} = -\frac{\partial \mathbf{A}}{\partial t} - \nabla \Phi \\ \nabla \cdot \mathbf{E} = \frac{\rho}{\epsilon_0} \ . \end{cases} \tag{2.16}$$

In the Coulomb gauge

$$\begin{cases} \nabla \cdot \mathbf{A} = 0 \\ -\nabla^2 \Phi = \frac{\rho}{\epsilon_0} \ , \end{cases} \tag{2.17}$$

Maxwell's equation

$$\nabla \times \mathbf{B} = \mu_0 \mathbf{j} + \frac{1}{c^2} \frac{\partial \mathbf{E}}{\partial t}$$

becomes [Ban85]:

$$\nabla^2 \mathbf{A} - \frac{1}{c^2} \frac{\partial^2 \mathbf{A}}{\partial t^2} - \frac{1}{c^2} \frac{\partial \nabla \Phi}{\partial t} = -\mu_0 \mathbf{j} \ , \tag{2.18}$$

where the symbol ∇^2 is the *vector Laplacian operator*, defined as:

$$\nabla^2 \mathbf{A} \equiv \nabla \left(\nabla \cdot \mathbf{A} \right) - \nabla \times \left(\nabla \times \mathbf{A} \right) \ . \tag{2.19}$$

Note that the vector Laplacian operator, like the scalar Laplacian, is a negative self-adjoint operator.

Let us restrict the domain of interest to be within a closed cavity with perfectly conducting walls. We expand the vector potential in terms of the set $\mathbf{a}_\lambda$ as:

$$\mathbf{A}(\mathbf{x},t)=\sum_\lambda q_\lambda(t)\mathbf{a}_\lambda(\mathbf{x}) \tag{2.20}$$

where

$$\nabla^2\mathbf{a}_\lambda+\frac{\omega_\lambda^2}{c^2}\mathbf{a}_\lambda=0\ , \tag{2.21}$$

with $\nabla\cdot\mathbf{a}_\lambda=0$, and with $\mathbf{a}_\lambda\times\widehat{n}=0$ on the metallic surface. The $\mathbf{a}_\lambda$ are orthogonal and complete in that they can be used to compose any transverse $\mathbf{A}$ satisfying the metallic boundary condition at any particular instant in time. By a transverse field we mean here one with zero divergence everywhere. Similarly, we expand the scalar potential as:

$$\Phi(\mathbf{x},t)=\sum_\mu r_\mu(t)\phi_\mu(\mathbf{x}) \tag{2.22}$$

where

$$\nabla^2\phi_\mu+\frac{\Omega_\mu^2}{c^2}\phi_\mu=0\ , \tag{2.23}$$

with $\phi_\mu=0$ on the metallic surface. The ϕ_μ are orthogonal and complete in that they can be used to compose any potential ϕ satisfying the metallic boundary condition $\phi=0$ on the metallic surface at any instant in time. The ϕ_μ are needed whenever source terms are present within the cavity. Note that in general the complete sets of the eigenvalues for the vector Laplacian operator and for the scalar Laplacian operator are different.

Now substituting 2.20 and 2.22 into 2.18, gives:

$$\sum_{\lambda} \left(\ddot{q}_\lambda + \omega_\lambda^2 q_\lambda\right) \mathbf{a}_\lambda + \sum_{\mu} \dot{r}_\mu \nabla \phi_\mu = \mu_0 c^2 \mathbf{j} \ . \tag{2.24}$$

Taking the scalar product of Eq. 2.24 with $\mathbf{a}_{\lambda'}$ and integrating over the cavity volume V gives:

$$\sum_{\lambda} \Big\{ \left(\ddot{q}_\lambda + \omega_\lambda^2 q_\lambda\right) \int_V \mathbf{a}_{\lambda'} \cdot \mathbf{a}_\lambda \, \mathrm{d}V \Big\} + \sum_{\mu} \Big\{ \dot{r}_\mu \int_V \mathbf{a}_{\lambda'} \cdot \nabla \phi_\mu \, \mathrm{d}V \Big\} = \mu_0 c^2 \int_V \mathbf{j} \cdot \mathbf{a}_{\lambda'} \, \mathrm{d}V \, . \tag{2.25}$$

The second integral of Eq. 2.25 can be written as:

$$\int_V \mathbf{a}_{\lambda'} \cdot \nabla \phi_\mu \, \mathrm{d}V = \int_V \nabla \cdot \left(\phi_\mu \mathbf{a}_{\lambda'}\right) \, \mathrm{d}V - \int_V \phi_\mu \left(\nabla \cdot \mathbf{a}_{\lambda'}\right) \, \mathrm{d}V \, . \tag{2.26}$$

The first integral on the right side of the above equation vanishes since $\phi_\mu = 0$ on the boundary (by the divergence theorem); the second term vanishes since the Coulomb gauge is used. Thus, if we normalize the $\mathbf{a}_\lambda$ as [Ban85]

$$\frac{\epsilon_0}{2} \int_V \mathbf{a}_{\lambda'} \cdot \mathbf{a}_\lambda \ \mathrm{d}V = U_\lambda \delta_{\lambda\lambda'} \ , \tag{2.27}$$

where $\delta_{\lambda\lambda'}$ is the Kronecker delta and U_λ is the energy density stored in the electromagnetic field due to the mode λ and using the identity $\mu_0 \epsilon_0 c^2 = 1$, we obtain [Ban83][1]:

$$\ddot{q}_\lambda + \omega_\lambda^2 q_\lambda = \frac{1}{2U_\lambda} \int_V \mathbf{j} \cdot \mathbf{a}_\lambda \ \mathrm{d}V \, . \tag{2.28}$$

Note that whenever there is no current in the cavity, the q_λ vary sinusoidally at frequencies ω_λ (if they are not identically zero). In this case $\mathbf{A}$ can be

---

[1] $c^2 = \frac{1}{\mu_0 \epsilon_0}$.

written as:

$$\mathbf{A}(\mathbf{x},t) = \sum_{\lambda} C_{\lambda}\mathbf{a}_{\lambda}\left(\mathbf{x}\right) cos(\omega_{\lambda}t + \theta_{\lambda}) \tag{2.29}$$

where the C_{λ} and θ_{λ} are constants depending on how the modes were generated. Therefore we see that the $\mathbf{a}_{\lambda}$ are the eigenmodes of the empty cavity and the corresponding ω_{λ} are the resonant frequencies.
Note that, from Eq. 2.21, the frequencies ω_{λ} scale naturally like the inverse of the structure dimension, i.e. $\omega_{\lambda} \propto a^{-1}$, where a is a characteristic length of the structure.

Similarly, beginning with Maxwell's equation $\nabla \cdot \mathbf{E} = \frac{\rho}{\epsilon_0}$, combined with the 3^{rd} equation in Eqs. 2.16, gives:

$$\begin{aligned} \nabla \cdot \left(-\frac{\partial \mathbf{A}}{\partial t} - \nabla \Phi \right) &= \frac{\rho}{\epsilon_0} \\ \Rightarrow \quad -\nabla \left(-\frac{\partial \mathbf{A}}{\partial t} \right) - \nabla^2 \Phi &= \frac{\rho}{\epsilon_0} \ , \end{aligned}$$

and then, from the Coulomb gauge and from 2.22 we get:

$$\begin{aligned} -\nabla^2 \Phi &= \frac{\rho}{\epsilon_0} \\ \Rightarrow \quad \sum_{\mu} r_{\mu}\left(t\right) \left[-\nabla^2 \phi_{\mu}\left(\mathbf{x}\right) \right] &= \frac{\rho}{\epsilon_0} \ . \end{aligned} \tag{2.30}$$

Now, recalling Eq. 2.23 we obtain:

$$\sum_{\mu} r_{\mu} \frac{\Omega_{\mu}^2}{c^2} \phi_{\mu} = \frac{\rho}{\epsilon_0} \ ; \tag{2.31}$$

if we take the scalar product of 2.31 with $\phi_{\mu'}$ and integrate over the volume V:

$$r_{\mu} \frac{\Omega_{\mu}^2}{c^2} \int_V \phi_{\mu} \cdot \phi_{\mu'} \, \mathrm{d}V = \frac{\rho}{\epsilon_0} \ . \tag{2.32}$$

We normalize in this way:

$$\frac{1}{2\mu_0}\int_V \phi_\mu \cdot \phi_{\mu'} \ \ \mathrm{d}V = T_\mu \delta_{\mu\mu'} \ , \tag{2.33}$$

and substituting in 2.32 we get

$$r_\mu = \frac{1}{2\Omega_\mu^2 T_\mu}\int_V \rho\phi_\mu \ \ \mathrm{d}V \, . \tag{2.34}$$

Whenever there are no charges in the cavity, all the r_λ (and thus also Φ) are zero.

Thus, given the homogeneous solutions ($\mathbf{a}_\lambda$, ϕ_μ) and the sources $\mathbf{j}$, ρ, we can solve for the q_λ, r_μ from Eqs. 2.28 and 2.34. These in turn allows us to solve for $\mathbf{E}$ and $\mathbf{B}$ by way of Eqs. 2.16, 2.20 and 2.22. The electric field is given by

$$\mathbf{E} = -\sum_\lambda \left(\dot{q}_\lambda \mathbf{a}_\lambda\right) - \sum_\mu \left(r_\mu \nabla\phi_\mu\right) \tag{2.35}$$

and the magnetic induction is

$$\mathbf{B} = \sum_\lambda q_\lambda \nabla \times \mathbf{a}_\lambda \ . \tag{2.36}$$

The stored energy is given by

$$\begin{aligned}\varepsilon &= \frac{1}{2}\int_V \left(\epsilon_0 \mathbf{E}^2 + \mathbf{B}^2/\mu_0\right) \ \ \mathrm{d}V \\ &= \sum_\lambda \left(\dot{q}_\lambda^2 U_\lambda + \omega_\lambda^2 q_\lambda^2 U_\lambda\right) + \sum_\mu r_\mu^2 \Omega_\mu^2 T_\mu \ . \end{aligned} \tag{2.37}$$

2.4.2 Longitudinal and transverse wake potentials

Consider a closed, empty (vacuum, no sources) cavity with perfectly conducting walls. An exciting particle with charge Q traverses the cavity at velocity $v = c$. We arrange our axes such that this charge enters the cavity at $z = 0$ at time $t = 0$ and follows the z–axis. It leaves at $z = L$. The longitudinal wake potential W_z (more precisely, the δ–function longitudinal wake potential) is defined as the total voltage lost by a test charge following at a distance s on the same path and also at $v = c$, divided by Q. Thus

$$W_z(s) = -\frac{1}{Q}\int_0^L \mathrm{d}z \; E_z(z, (z+s)/c) \qquad (2.38)$$

where $E_z(z,t)$ is the z component of $\mathbf{E}$ on the z–axis due to the exciting charge. Note that since a signal cannot travel faster than the speed of the light, $W_z = 0$ for $s < 0$.

The usefulness of this definition is that W_z can be used as a Green's function for computing the voltage loss within an ultra-relativistic bunch of arbitrary shape. In this case the voltage loss per unit total charge, noted $\mathtt{W}_z$, is also called the wake potential, or sometimes the bunch wake to differentiate it from W_z. The two wakes are connected by

$$\mathtt{W}_z(s) = \int_0^\infty \mathrm{d}s' \; I'(s-s')W_z(s') \; , \qquad (2.39)$$

where $I'(s)$ is the charge distribution of the bunch. Note that $cI'(s)$ simply equals the current distribution $I(t = s/c)$. Approximating the bunch as rigid is normally valid since a high energy beam does not change its shape over the length of a cavity. Approximating the speed as $v = c$ is valid since the wake fields of a cavity turn out to be independent of the energy of the bunch at high energies. This approach differs greatly from the more difficult method (which still needs to be done for low energy beams) of self consistently solving for the fields in the cavity and the beam motion.

To calculate W_z we need first to find the fields in the cavity due to the exciting charge. The source terms due to the exciting charge are

$$\begin{aligned} \rho(\mathbf{x},t) &= Q\delta(x)\delta(y)\delta(z-ct) \\ \mathbf{j}(\mathbf{x},t) &= \hat{z}c\rho(\mathbf{x},t) \ . \end{aligned} \tag{2.40}$$

Eq. 2.28 becomes

$$\ddot{q}_\lambda + \omega_\lambda^2 q_\lambda = \frac{Qc}{2U_\lambda} \begin{cases} 0 & t<0 \\ a_{\lambda z}(0,0,ct) & 0<t<L/c \\ 0 & t>L/c \ , \end{cases} \tag{2.41}$$

where $a_{\lambda z}(x,y,z)$ is the z–component of $\mathbf{a}_\lambda$. Using the initial condition $q(0) = \dot{q}(0) = 0$ (no fields in the cavity before the charge enters) and by variation of parameters, we get

$$q_\lambda(t) = \frac{Qc}{2U_\lambda\omega_\lambda}\int_0^{min(t,L/c)} dt' \ \sin\omega_\lambda(t-t')a_{\lambda z}(0,0,ct') \ . \tag{2.42}$$

Similarly, substituting 2.40 into 2.34, we get:

$$r_\mu(t) = \frac{Q}{2\Omega_\mu^2 T_\mu} \begin{cases} 0 & t<0 \\ \phi_\mu(0,0,ct) & 0<t<L/c \\ 0 & t>L/c \end{cases} \tag{2.43}$$

where the three arguments of ϕ_μ represent respectively its x, y and z dependence.

With the above two equations and Eqs. 2.35–2.37 we can construct the fields and stored energy due to the exciting charge for all time solely in terms of the empty cavity solutions $\mathbf{a}_\lambda$, ϕ_μ, ω_λ.

From Eqs. 2.37 and 2.42, we see that the energy left in the cavity after the exciting charge has left ($t > L/c$) is

$$\begin{aligned}\varepsilon &= \sum_\lambda \left(\dot{q}_\lambda^2 + \omega_\lambda^2 q_\lambda^2\right) U_\lambda \\ &= Q^2 \sum_\lambda \frac{|V_\lambda|^2}{4U_\lambda} \ , \end{aligned} \tag{2.44}$$

where

$$V_\lambda = \int_0^L \mathrm{d}z \ \exp\left(\mathbf{i}\omega_\lambda z/c\right) a_{\lambda z}(0,0,z) \ . \tag{2.45}$$

Defining the *loss factor* k_λ as:

$$k_\lambda = \frac{|V_\lambda|^2}{4U_\lambda} \ , \tag{2.46}$$

the stored energy becomes simply [Ban85]:

$$\varepsilon = Q^2 \sum_\lambda k_\lambda \ . \tag{2.47}$$

Thus k_λ gives the amount of energy deposited in mode λ by the exciting charge, hence the name loss factor.

Since the potential V_λ, for the dipole modes in a cylindrical cavity, depends linearly on the offset where it is calculated, it is useful for our following calculations, to normalize this quantity by the cavity (or iris) radius, and then Eq. 2.46 becomes:

$$k_\lambda = \frac{|V_\lambda|^2}{4U_\lambda a^2} \ , \tag{2.48}$$

The variables on the right side of Eq. 2.46 can have the following physical interpretation: suppose that the mode λ of the empty cavity has been excited by whatever method; from the definition of U_λ (2.27) we see that it can represent the energy stored in this mode, up to a multiplicative constant. If now a test charge traverses the cavity at $v = c$ along the z–axis, then $|V_\lambda|^2$ can be thought of as the square of the maximum voltage it can gain (with respect to time of entrance) from this mode, up to the same multiplicative constant. Thus, just like the eigenfrequency ω_λ, k_λ is a property of the empty cavity depending on its shape. Unlike ω_λ it depends also on the integration path used for calculating V_λ.

Now, back to the calculation of the wake potential in terms of the normal mode solutions of the cavity, it can be shown [Ban85] that the problem is solved in three pieces (test charge enters before, at the same moment, or after the exiting charge). Combining Eqs. 2.35 and 2.38 yields:

$$\begin{aligned} W_z(s) = & \frac{1}{Q}\left[\sum_\lambda \int_0^L \mathrm{d}z\ \dot{q}_\lambda\left(\frac{z+s}{c}\right) a_{\lambda z}(0,0,z)\right. \\ & \left. + \sum_\mu \int_0^L \mathrm{d}z\ r_\mu\left(\frac{z+s}{c}\right)\frac{\partial\phi_\mu}{\partial z}(0,0,z)\right] , \end{aligned} \tag{2.49}$$

then substituting for q_λ, r_μ from Eqs. 2.42 and 2.43, and integrating, give us our final results:

$$W_z(s) = \begin{cases} \sum_\lambda k_\lambda 2\cos\left(\frac{\omega_\lambda s}{c}\right)\ exp\left(-\frac{\omega_\lambda}{2Q_\lambda}\frac{s}{c}\right) & s > 0 \\ \sum_\lambda k_\lambda & s = 0 \\ 0 & s < 0\ . \end{cases} \tag{2.50}$$

Here Q_λ is the *quality factor*, defined as:

$$Q_\lambda = \frac{\omega_\lambda \epsilon_\lambda}{P_\lambda} \tag{2.51}$$

with ϵ_λ is the energy stored in the λ mode, and P_λ is the power loss at the walls.
Note that due to the symmetry introduced by taking the velocities to be c, W_λ does not depend on the scalar potential solutions ϕ_λ, even if the test charge enters while the exciting charge is still in the cavity $(0 < s < L)$. For $v \neq c$ however, the scalar potential solutions can become important. W_λ then becomes very complicated, and the general usefulness of the wake potential concept is lost. Note also that, since W_λ is expressible as a sum of cosines, its maximum value is at $s = 0^+$.

The transverse wake potential can be determined from the longitudinal one, by using the Panofsky–Wenzel theorem:

$$\nabla_\perp W_z(\mathbf{r}, s) = \partial_s \mathbf{W}_\perp(\mathbf{r}, s) \tag{2.52}$$

For significant case of $s > 0$, we obtain [Pal94],[Ban85]

$$\mathbf{W}_{\perp\lambda}(s) = \sum_\lambda 2k_{\perp\lambda} \frac{c}{\omega_\lambda} \sin\left(\omega_\lambda \frac{s}{c}\right) \exp\left(-\frac{\omega_\lambda}{2Q_\lambda} \frac{s}{c}\right) \tag{2.53}$$

where $k_{\perp\lambda}$ is the normalized transverse loss factor as defined in Eq. 2.48.

2.4.3 Scaling of wake fields effects with frequency.

Let us now restrict our interest to cylindrically symmetric structures. We will now use polar coordinates (r, ϑ) to denote transverse position. The exciting charge traverses at $r = r'$, $\vartheta = 0$ (on the x–axis). Let the tube radius of the structure be denoted by a. In such a structure all the modes depend on ϑ as $e^{im\vartheta}$, where m is an integer. The $m = 0, 1, 2$ modes are called respectively the longitudinal (monopole), dipole, quadrupole modes. Therefore the m–pole component of the wakes can be written as a sum over all the m–pole modes as [Ban85]:

$$W_{z,m} = \left(\frac{r'}{a}\right)^m \left(\frac{r}{a}\right)^m \cos(m\vartheta) \sum_n 2k_{mn}(a) \cos\left(\frac{\omega_{mn}s}{c}\right) \ , \tag{2.54}$$

for $s > 0$, where k_{mn} is the loss factor defined before (2.46); while for $m \neq 0$, from the Panofsky–Wenzel theorem (2.52):

$$\mathbf{W}_{\perp,m} = m \left(\frac{r'}{a}\right)^m \left(\frac{r}{a}\right)^{m-1} \left(\widehat{\mathbf{r}} \cos(m\vartheta) - \widehat{\vartheta} \sin(m\vartheta)\right) \sum_n \frac{2k_{mn}(a)}{\omega_{mn}a/c} \sin\left(\frac{\omega_{mn}s}{c}\right) \ . \tag{2.55}$$

For $m = 0$, $\mathbf{W}_{\perp,m} = 0$. In the above equations $k_{mn}(a)$ is the loss factor calculated at $r = a$.

To get the total wake field we need to sum over all the multiple contribution. Normally bunches remain near the axis and (r/a), (r'/a) can be considered small. Then the longitudinal wake field is dominated by the longitudinal modes ($m = 0$) whereas the transverse wake field is dominated by the dipole modes ($m = 1$). Thus normally we can approximate the wakes as:

$$W_z \simeq \sum_n 2k_{0n}(a) \cos\left(\frac{\omega_{0n}s}{c}\right) \qquad s > 0 \tag{2.56}$$

$$\mathbf{W}_\perp \simeq \left(\frac{r'}{a}\right) \widehat{\mathbf{x}} \sum_n \frac{2k_{1n}(a)}{(\omega_{1n}a/c)} \sin\left(\frac{\omega_{1n}s}{c}\right) \qquad s > 0 \ . \tag{2.57}$$

Note that the longitudinal wake is approximately independent of the transverse position of both the exciting charge and the test charge. The transverse wake depends on the exciting charge as the first power of its offset. The transverse wake is in the x–direction and is independent of the test charge's transverse position.

From its definition, see Eq. 2.46, it follows that the the loss factor $k_{mn}(a)$ scales like the inverse of the length, i.e. like ω_{mn}, while the loss factor per meter, of course, scales as ω_{mn}^2.
Now, using the Taylor series, one can show that:

$$W_z \approx \omega_{0n} \cdot \left(1 - \frac{\omega_{0n}^2 s^2}{c^2}\right) \qquad \omega_{0n} \sim c/a \ , \quad k_{0n} \approx \omega_{0n} \quad \text{[Mon85]}$$

$$\Rightarrow W_z \approx \omega_{0n} \tag{2.58}$$

$$\Rightarrow \frac{W_z}{g} \approx \frac{\omega_{0n} 2}{\lambda} \approx \omega_{0n}^2 \ ,$$

where $g = \lambda/2$ the tube length and λ is the wave–length. Hence the longitudinal wake fields per unit length scale approximatively as f^2. As for he transverse potential, at short distances:

$$\mathbf{W}_\perp \approx \frac{k_{1n}}{\omega_{1n}} \cdot \frac{c}{a} \left(\frac{\omega_{1n} s}{c}\right) \qquad \omega_{0n} \sim c/a \text{ [Mon85]}, \quad k_{1n} \approx \omega_{1n} \approx 1/a$$

$$\Rightarrow \frac{\mathbf{W}_\perp}{g} \approx \frac{2\omega_{1n}^2}{\lambda} \approx \omega_{1n}^3 \ , \tag{2.59}$$

the transverse wake fields per unit of length scale approximatively as f^3.

2.5 Fields in a pill–box cavity: alternative method

2.5.1 Calculation of the vector potential A

As saw in the section 2.4.1, one needs to solve:

$$\begin{cases} \triangle \mathbf{A} - \frac{1}{c^2}\partial_t^2 \mathbf{A} = 0 \\ \nabla \cdot \mathbf{A} = 0 \\ \mathbf{A} \mid_{\partial V} \times \mathbf{n} = 0 \end{cases} \tag{2.60}$$

In a pill–box cavity like the one in Fig. (2.5), $\mathbf{A}(r, \vartheta, z, t)$ is defined from

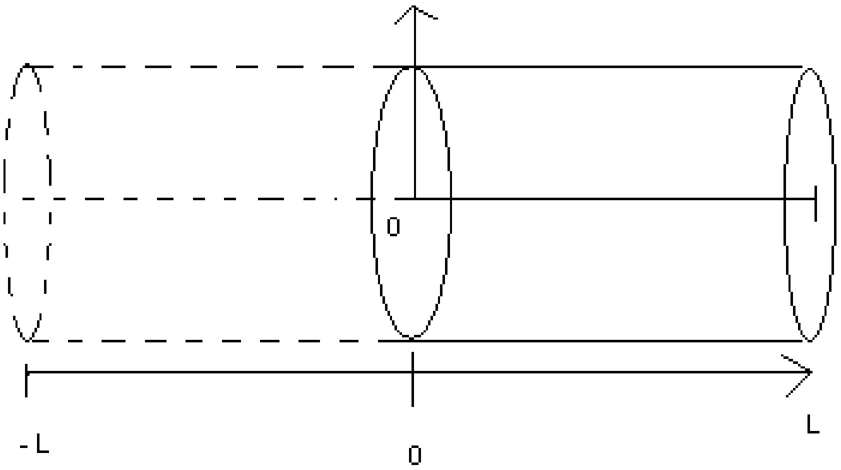

Figure 2.5: Pill–box cavity with length extension from $-L$ to L.

$z = 0$ to $z = L$; from the Coulomb gauge we have:

$$\nabla \cdot \mathbf{A} = 0 \ \Rightarrow \ \frac{1}{r}\partial_r \left(rA_r\right) + \frac{1}{r}\partial_\vartheta A_\vartheta + \partial_z A_z = 0 \tag{2.61}$$

and recalling the boundary conditions:

$$\begin{aligned} (A_r, A_\vartheta) \mid_{z=0,L} &= 0 \\ \Rightarrow \partial_z A_z \mid_{z=0,L} &= 0 \ . \end{aligned} \tag{2.62}$$

- **Extension of the field A over $[-L, L]$ to a periodic C^∞ function**

We define a function $\widetilde{\mathbf{A}}$ in this way[2]:

---

[2] from this moment we will use the notation:

$$\begin{aligned} 0^+ &= \ 0 + \varepsilon \\ 0^- &= \ 0 - \varepsilon \\ L^- &= \ L - \varepsilon \\ -L^+ &= -L + \varepsilon \ , \end{aligned}$$

where ε is an infinitesimally small number ($\varepsilon \to \infty$).

✓ $\widetilde{A}_z$

$$\widetilde{A}_z\left(r,\vartheta,z\right)=\left\{\begin{array}{lll} A_z\left(r,\vartheta,z\right) & for & z\in[0,L] \\ A_z\left(r,\vartheta,-z\right) & for & z\in[-L,0]\end{array}\right. \tag{2.63}$$

and we have:

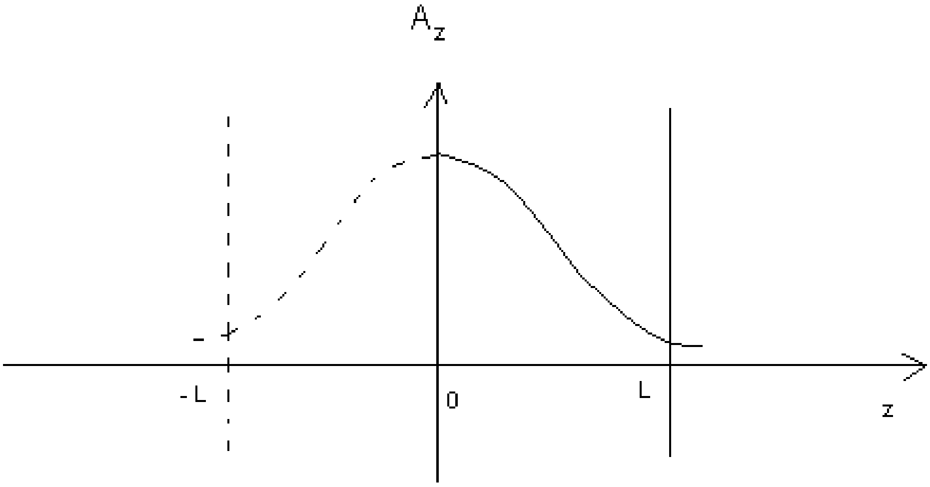

Figure 2.6: $\widetilde{A}_z$.

– Continuity at $z=0$:

$$\widetilde{A}_z\left(r,\vartheta,0^-\right)=\widetilde{A}_z\left(r,\vartheta,0^+\right)\equiv A_z\left(r,\vartheta,0^+\right)$$

– Periodicity at $z=\pm L$:

$$\widetilde{A}_z\left(r,\vartheta,L^-\right)=\widetilde{A}_z\left(r,\vartheta,-L^+\right)\equiv A_z\left(r,\vartheta,L^-\right)$$

✓ $\widetilde{A}_{r,\vartheta}$

$$\widetilde{A}_{r,\vartheta}\left(r,\vartheta,z\right)=\left\{\begin{array}{lll} A_{r,\vartheta}\left(r,\vartheta,z\right) & for & z\in[0,L] \\ -A_{r,\vartheta}\left(r,\vartheta,-z\right) & for & z\in[-L,0]\end{array}\right. \tag{2.64}$$

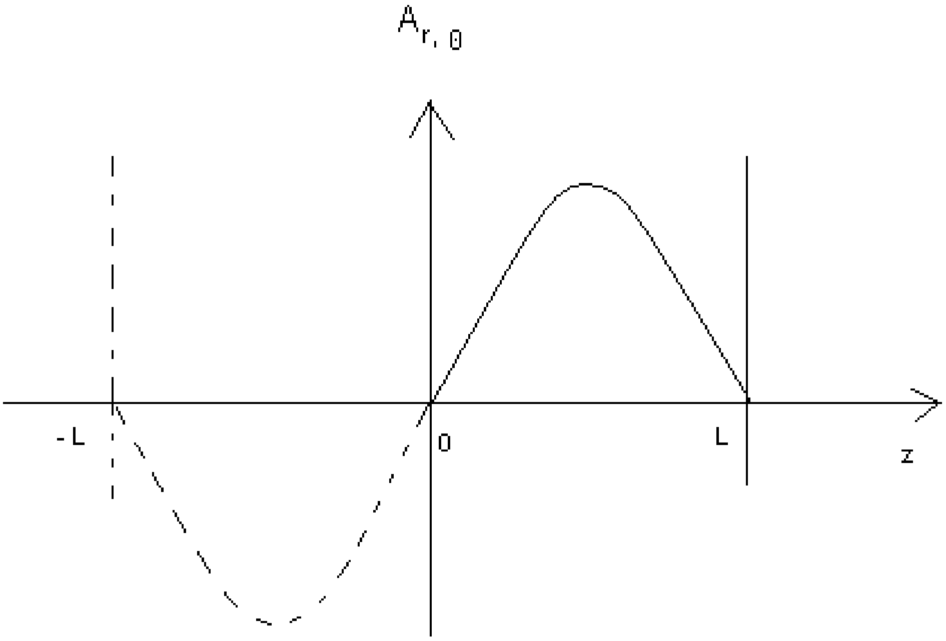

Figure 2.7: $\widetilde{A}_{r,\vartheta}$.

where we have again:

- Continuity at $z = 0$:

$$\widetilde{A}_{r,\vartheta}\left(r,\vartheta,0^-\right) = \widetilde{A}_{r,\vartheta}\left(r,\vartheta,0^+\right) \equiv 0$$

- Periodicity at $z = \pm L$:

$$\widetilde{A}_{r,\vartheta}\left(r,\vartheta,L^-\right) = \widetilde{A}_{r,\vartheta}\left(r,\vartheta,-L^+\right) \equiv 0 \ .$$

✓ By construction one finds now:

- (even derivatives):

$\partial_z^{2p}\widetilde{A}_z\left(z \to 0^+\right) = \partial_z^{2p}\widetilde{A}_z\left(z \to 0^-\right) \equiv \partial_z^{2p}A_z\left(0^+\right)$

– (odd derivatives):

$$\partial_z^{2p+1}\widetilde{A}_{r,\vartheta}\left(z \to 0^+\right) = \partial_z^{2p+1}\widetilde{A}_{r,\vartheta}\left(z \to 0^-\right) \equiv \partial_z^{2p+1}A_{r,\vartheta}\left(0^+\right)$$

and idem for L^- and $-L^+$.

- **Demonstration of the continuity of $(\partial_z^{2p+1}A_z)$ and $(\partial_z^{2p}A_{r,\vartheta})$**

✓ for $z \leq 0$, $\quad \partial_z^{2p}\widetilde{A}_{r,\vartheta}(z) = -\partial_z^{2p}A_{r,\vartheta}(-z) = -\partial_z^{2p}\widetilde{A}_{r,\vartheta}(-z)$

$\Rightarrow \quad \partial_z^{2p}\widetilde{A}_{r,\vartheta}(z)$ continuous at $z = 0$ if $\quad \partial_z^{2p}A_{r,\vartheta}\,|_{z=0^+,L^-} = 0$;

✓ for $z \leq 0$, $\quad \partial_z^{2p+1}\widetilde{A}_z(z) = -\partial_z^{2p+1}A_z(-z) = -\partial_z^{2p+1}\widetilde{A}_z(-z)$

$\Rightarrow \quad \partial_z^{2p+1}\widetilde{A}_z(z)$ continuous at $z = 0$ if $\quad \partial_z^{2p+1}A_z\,|_{z=0^+,L^-} = 0$.

From Coulomb gauge: $\partial_z A_z = -\left(\frac{1}{r}\partial_r(rA_r) + \frac{1}{r}\partial_\vartheta A_\vartheta\right)$

$\Rightarrow \quad \partial_z A_z\,|_{z=0^+,L^-} = 0$ from boundary conditions, and also:

$\partial_z^{2p+1}A_z = -\left(\frac{1}{r}\partial_r\left(r\left(\partial_z^{2p}A_r\right)\right) + \frac{1}{r}\partial_\vartheta\left(\partial_z^{2p}A_\vartheta\right)\right)$,

and therefore: $\partial_z^{2p+1}A_z\,|_{z=0^+,L^-} = 0 \quad$ if $\quad \partial_z^{2p}A_r\,|_{z=0^+,L^-} = \partial_z^{2p}A_\vartheta\,|_{z=0^+,L^-} = 0 \quad \forall\ (r,\vartheta)$.

✓ Even derivatives of A_r and A_ϑ:

$$(\triangle\mathbf{A})_r \cdot \tfrac{1}{c}\partial_t^2 A_r = \tfrac{1}{r}\partial_r\left(r\partial_r A_r\right) + \tfrac{1}{r^2}\partial_\vartheta^2 A_r + \partial_z^2 A_r - \tfrac{A_r}{r^2} - \tfrac{2}{r^2}\partial_\vartheta A_\vartheta - \tfrac{1}{c^2}\partial_t^2 A_r = 1,$$

$$\Rightarrow \quad \partial_z^2 A_r = -\tfrac{1}{c^2}\partial_t^2 A_r - \tfrac{1}{r}\partial_r\left(r\partial_r A_r\right) - \tfrac{1}{r}\partial_\vartheta^2 A_r + \tfrac{A_r}{r^2} + \tfrac{2}{r^2}\partial_\vartheta A_\vartheta,$$

$$\Rightarrow \quad \partial_z^2 A_r\,|_{z=0^+,L^-} = 0\ .$$

$$(\triangle\mathbf{A})_\vartheta - \tfrac{1}{c^2}\partial_t^2 A_\vartheta = \tfrac{1}{r}\partial_r\left(r\partial_r A_\vartheta\right) + \tfrac{1}{r^2}\partial_\vartheta^2 A_\vartheta + \partial_z^2 A_\vartheta - \tfrac{A_\vartheta}{r^2} + \tfrac{2}{r^2}\partial_\vartheta A_r - \tfrac{1}{c^2}\partial_t^2 A_\vartheta = 0,$$

$$\Rightarrow \quad \partial_z^2 A_\vartheta = \tfrac{1}{c^2}\partial_t^2 A_\vartheta - \tfrac{1}{r}\partial_r\left(r\partial_r A_r\right) - \tfrac{1}{r^2}\partial_\vartheta^2 A_\vartheta + \tfrac{A_\vartheta}{r^2} - \tfrac{2}{r^2}\partial_\vartheta A_r,$$

$$\Rightarrow \quad \partial_z^2 A_\vartheta\,|_{z=0^+,L^-} = 0\ ;$$

and then, by recurrence we obtain:

$$\left(\partial_z^{2p}A_r,\partial_z^{2p}A_\vartheta\right)|_{z=0^+,L^-}=0,$$

$$\Rightarrow\left(\partial_z^{2p+2}A_r,\partial_z^{2p+2}A_\vartheta\right)|_{z=0^+,L^-}=0\ .$$

Conclusion: From $\mathbf{A}$, solution of Maxwell Equation on $[0,L]$, and the boundary conditions, we know that $\widetilde{\mathbf{A}}$ is C^∞ periodic, of period $2L$, then:

$$\begin{aligned}A_z\left(r,\vartheta,z,t\right)&=\sum_{p=0}^{\infty}\int\mathrm{d}\omega e^{-i\omega t}\cos\left(\frac{p\pi z}{L}\right)A_z^{(p)}\left(r,\vartheta;\omega\right)\\A_{r,\vartheta}\left(r,\vartheta,z,t\right)&=\sum_{p=1}^{\infty}\int\mathrm{d}\omega e^{-i\omega t}\sin\left(\frac{p\pi z}{L}\right)A_{r,\vartheta}^{(p)}\left(r,\vartheta;\omega\right)\\k_p&=\frac{p\pi}{L}\ .\end{aligned}\tag{2.65}$$

- **Solving for $\mathbf{A}^{(p)}\left(r,\vartheta;\omega\right)$**

From the wave equation and the Coulomb gauge:

$$\begin{cases}\triangle\mathbf{A}-\frac{1}{c^2}\partial_t^2\mathbf{A}=0\ \Rightarrow\ \triangle\mathbf{A}\left(r,\vartheta,z;\omega\right)+\frac{\omega^2}{c^2}\mathbf{A}\left(r,\vartheta,z;\omega\right)=0\\\nabla\cdot\mathbf{A}=0\end{cases}\tag{2.66}$$

Let us now introduce the differential operator:

$$\Box_s=\frac{1}{r}\partial_r\left(r\partial_r\right)+\frac{1}{r^2}\partial_\vartheta^2+\left(\frac{\omega^2}{c^2}-k_p^2\right)\ ,\tag{2.67}$$

and then consider:

- the $r-$component of the wave equation 2.66:

$$\Box_s A_r^{(p)}\left(r,\vartheta;\omega\right)-\frac{A_r^{(p)}}{r^2}\left(r,\vartheta;\omega\right)-\frac{2}{r^2}\partial_\vartheta A_\vartheta^{(p)}\left(r,\vartheta;\omega\right)=0\ ;\qquad(2.68)$$

- the $\vartheta-$component of the wave equation:

$$\Box_s A_\vartheta^{(p)}\left(r,\vartheta;\omega\right)-\frac{A_\vartheta^{(p)}}{r^2}\left(r,\vartheta;\omega\right)-\frac{2}{r^2}\partial_\vartheta A_r^{(p)}\left(r,\vartheta;\omega\right)=0\ ;\qquad(2.69)$$

- the $z-$component of the wave equation:

$$\Box_s A_z^{(p)}\left(r,\vartheta;\omega\right)=0\ ;\qquad(2.70)$$

- the Coulomb gauge fixing:

$$\frac{1}{r}\partial_r\left(rA_r^{(p)}\right)+\frac{1}{r}\partial_\vartheta A_\vartheta^{(p)}-k_pA_z^{(p)}=0\ .\qquad(2.71)$$

We use now the identity:

$$\begin{aligned}\frac{1}{r^2}\partial_r\left(r\partial_r\left(r\phi\right)\right)&=\frac{1}{r}\partial_r\left(r\partial_r\phi\right)+\frac{2}{r}\partial_r\phi+\frac{\phi}{r^2}\\&=\frac{1}{r}\partial_r\left(r\partial_r\phi\right)+\frac{2}{r^2}\partial_r\left(r\phi\right)-\frac{\phi}{r^2}\ ,\quad\forall\phi\qquad(2.72)\end{aligned}$$

and then:

$$\Box_s\phi=\tfrac{1}{r}\left(\Box_s\left(r\phi\right)+\tfrac{\phi}{r}-\tfrac{2}{r}\partial_r\left(r\phi\right)\right)\ ,\qquad\forall\phi\ .\qquad(2.73)$$

Replacing ϕ by $A_r^{(p)}$:

- from Eq. 2.68 ⇒

$$\Box_s\left(rA_r^{(p)}\right)-\frac{2}{r}\left(\partial_r\left(rA_r^{(p)}\right)+\partial_\vartheta A_\vartheta^{(p)}\right)=0\ ;\qquad(2.74)$$

- from Eq. 2.69 ⇒

$$\Box_s\left(rA_\vartheta^{(p)}\right)-\frac{2}{r}\left(\partial_r\left(rA_\vartheta^{(p)}\right)-\partial_\vartheta A_r^{(p)}\right)=0\ .\qquad(2.75)$$

Notice that:

$$\begin{aligned} \tfrac{1}{r}\partial_r\left(rA_r^{(p)}\right)+\tfrac{1}{r}\partial_\vartheta A_\vartheta^{(p)} &= k_pA_z^{(p)}=\tfrac{k_p}{i\omega}E_z \\ \tfrac{1}{r}\partial_r\left(rA_\vartheta^{(p)}\right)-\partial_\vartheta A_r^{(p)} &= \left(\nabla\times\mathbf{A}^{(p)}\right)_z=B_z^{(p)}\ . \end{aligned} \tag{2.76}$$

Therefore:

- ∘ from Eq. 2.74 ⇒

$$\Box_s\left(rA_r^{(p)}\right)=\frac{2k_p}{i\omega}E_z^{(p)}\ ; \tag{2.77}$$

- ∘ from Eq. 2.75 ⇒

$$\Box_s\left(rA_\vartheta^{(p)}\right)=2B_z^{(p)}\ ; \tag{2.78}$$

- ∘ from Eq. 2.70 ⇒

$$\Box_sA_z^{(p)}=0\ ; \tag{2.79}$$

- ∘ from Eq. 2.71 ⇒

$$\tfrac{1}{r}\partial_r\left(rA_r^{(p)}\right)+\tfrac{1}{r}\partial_\vartheta A_\vartheta^{(p)} = k_pA_z^{(p)}\ . \tag{2.80}$$

One can now expand the fields into multiple components:

$$\phi^{(p)}\left(r,\vartheta;\omega\right)=\sum_{m=0}^{\infty}e^{im\vartheta}\phi^{(p,m)}\left(r;\omega\right)\ ,\quad\forall\phi\ , \tag{2.81}$$

in such a way that:

$$\begin{aligned} &\Box_s=\tfrac{1}{r}\partial_r\left(r\partial_r\right)+\left(\left(\tfrac{\omega^2}{c^2}-k_p^2\right)-\tfrac{m^2}{r^2}\right) \\ &\gamma_p^2\equiv\left(\tfrac{\omega^2}{c^2}-k_p^2\right)\ . \end{aligned} \tag{2.82}$$

For the TM modes, $B_z\equiv 0$:

- $A_z^{(p,m)}$

$$\begin{aligned} &\Box_s A_z^{(p,m)}(r;\omega) = 0 \\ &\Rightarrow\ A_z^{(p,m)}(r;\omega) =\ C_z^{(p,m)} J_m(\gamma_p r)\ , \end{aligned} \tag{2.83}$$

where $C_z^{(p,m)}$ is a constant;

- $A_\vartheta^{(p,m)}$

$$\begin{aligned} &\Box_s (rA_\vartheta)^{(p,m)}(r;\omega) = 0 \\ &\Rightarrow\ A_\vartheta^{(p,m)}(r;\omega) =\ \tfrac{1}{r} C_\vartheta^{(p,m)} J_m(\gamma_p r)\ , \end{aligned} \tag{2.84}$$

where $C_\vartheta^{(p,m)}$ is a constant;

- $A_r^{(p,m)}$

$$\begin{aligned} B_z^{(p)} = 0 \quad &\Rightarrow\ \partial_r \left(rA_\vartheta^{(p,m)} \right) =\ imA_r^{(p,m)} \\ &\Rightarrow\ A_r^{(p,m)}(r;\omega) =\ C_r^{(p,m)} J'_m(\gamma_p r) \\ &\Leftrightarrow \gamma_p C_\vartheta^{(p,m)} = imC_r^{(p,m)}\ , \end{aligned} \tag{2.85}$$

where $C_r^{(p,m)}$ is a constant;

- from Eq. 2.80

$$\frac{1}{r}\partial_r\left(r\left(imA_r^{(p,m)}\right)\right)+\frac{(im)^2}{r}A_\vartheta^{(p,m)}=imk_pA_z^{(p,m)}$$

$$\Rightarrow\frac{1}{r}\partial_r\left(r\partial_r\left(rA_\vartheta^{(p,m)}\right)\right)-\frac{m^2}{r^2}\left(rA_\vartheta^{(p,m)}\right)=imk_pA_z^{(p,m)}$$

$$\Rightarrow\underline{\Box_s\left(rA_\vartheta^{(p,m)}\right)}-\gamma_p^2\left(rA_\vartheta^{(p,m)}\right)+\underline{\frac{m^2}{r^2}\left(rA_\vartheta^{(p,m)}\right)}-\underline{\frac{m^2}{r^2}\left(rA_\vartheta^{(p,m)}\right)}=imk_pA_z^{(p,m)}$$

where the underlined components annihilate themselves,

$$\Rightarrow\gamma_p^2\left(rA_\vartheta^{(p,m)}\right)=-imk_pA_z^{(p,m)}$$

$$\Rightarrow\gamma_p^2C_\vartheta^{(p,m)}=-imk_pC_z^{(p,m)}\ ;\tag{2.86}$$

- from the boundary conditions:

$$A_\vartheta^{(p,m)}(R;\omega)=A_z^{(p,m)}(R;\omega)=0$$

$$\Rightarrow\ \gamma_pR=\lambda_{mn}\ ,\quad \lambda_{mn}=n^{th}\ zero\ of\ J_m(\lambda)\ \text{ with } n\geq 1\ ;\tag{2.87}$$

$$\Rightarrow\ \tfrac{\omega_{mnp}^2}{c^2}=k_p^2+\left(\tfrac{\lambda_{mn}}{R}\right)^2\ ,$$

and then:

$$\begin{cases} A_r^{(p,m)}(r;\omega) & =-C_{mnp}\gamma_pk_pJ_m'\left(\lambda_{mn}\frac{r}{R}\right)\\ A_\vartheta^{(p,m)}(r;\omega) & =-C_{mnp}(-im)\,k_p\frac{1}{r}J_m\left(\lambda_{mn}\frac{r}{R}\right)\\ A_z^{(p,m)}(r;\omega) & =C_{mnp}\gamma_p^2J_m\left(\lambda_{mn}\frac{r}{R}\right)\ . \end{cases}\tag{2.88}$$

For the TE modes, $E_z = 0 \;\Rightarrow\; A_z = 0$:

- $A_r^{(p,m)}$

$$\begin{aligned} \Box_s \left(r A_r^{(p,m)} \right)(r;\omega) &= 0 \\ \Rightarrow\; A_r^{(p,m)}(r;\omega) &= \tfrac{1}{r} C_r^{(p,m)} J_m(\gamma_p r) \;, \end{aligned} \tag{2.89}$$

  where $C_r^{(p,m)}$ is a constant;

- $A_\vartheta^{(p,m)}$

$$\tfrac{1}{r}\left(\partial_r \left(r A_r^{(p,m)} \right) \right) + \tfrac{im}{r} A_\vartheta^{(p,m)} = 0$$

$$\Rightarrow\; A_\vartheta^{(p,m)}(r;\omega) = C_\vartheta^{(p,m)} J'_m(\gamma_p r) \tag{2.90}$$

$$\Leftrightarrow \quad im C_\vartheta^{(p,m)} = \gamma_p C_r^{(p,m)} \;;$$

- from the boundary conditions:

$$A_\vartheta^{(p,m)}(R;\omega) = 0$$

$$\begin{aligned} &\Rightarrow\; \gamma_p R = \lambda'_{mn} \;, \quad \lambda'_{mn} = n^{th}\; zero\; of\; J'_m(\lambda) \text{ with } n \geq 1 \;; \\ &\Rightarrow\; \tfrac{\omega^2_{mnp}}{c^2} = k_p^2 + \left(\tfrac{\lambda'_{mn}}{R} \right)^2 \;, \end{aligned} \tag{2.91}$$

  and therefore:

$$\begin{cases} A_r^{(p,m)}(r;\omega) &= C'_{mnp} \frac{im}{r} J_m\left(\lambda'_{mn} \frac{r}{R} \right) \\ A_\vartheta^{(p,m)}(r;\omega) &= C'_{mnp} \gamma_p J'_m\left(\lambda'_{mn} \frac{r}{R} \right) \\ A_z^{(p,m)}(r;\omega) &= 0 \;, \end{cases} \tag{2.92}$$

  and recalling from Eq. 2.16

$$\begin{cases} \mathbf{E} = -\partial_t \mathbf{A} \\ \mathbf{B} = \nabla \times \mathbf{A} \end{cases}$$

2.5.2 Single–cell accelerating cavities

In free space, waves of any frequency can propagate. The phase velocity and the group velocity of such waves are the speed of the light and one can demonstrate that such waves have a purely transverse polarization, so that they are not usable for acceleration of charged particles.

Moreover, in a regular cylindrical waveguide only waves above a cutoff frequency [3] can propagate and such waves can have a longitudinal electric field component; the group velocity of such waves are below the speed of light, but the phase velocity is above the speed of the light, thus a regular waveguide is also an unacceptable device for acceleration of beams [Ten03].

The problem with the regular waveguide is that, with a phase velocity exceeding c, the accelerating phase of the wave will overtake the particles which are to be accelerated, and ultimately the decelerating phase will overlap those particles. One solution, then is to consider using the accelerating phase to accelerate the particles, and then to separate the wave from particles, before the decelerating phase can interact with them (Fig. 2.8). It would appear that, by applying conducting boundary conditions in the longitudinal degree of freedom, we at the last have created a time–dependent electric field which is useful for acceleration of particles. We can now write, after imposing the reality condition, the general solutions to the time–dependent fields in a

---

[3] $\omega_c = \frac{1}{\sqrt{\mu\epsilon}} \frac{\lambda_{mn}}{R}$ where R is the waveguide radius and λ_{mn} is the n^{th} zero of the Bessel's equation of the first kind, J_m

TE_{mnp} mode:

$$\begin{aligned}
E_r &= \sum_{mnp} \left(-\frac{m\omega_{mnp}}{r\gamma_p^2}\right)\ b_{mnp}\ \cos\left(\omega_{mnp}t + m\vartheta\right)\ \sin\left(\frac{p\pi z}{L}\right) J_m\left(\frac{\lambda'_{mn}}{R}r\right) \\
E_\vartheta &= \sum_{mnp} \left(\frac{\omega_{mnp}}{\gamma_p}\right)\ b_{mnp}\ \sin\left(\omega_{mnp}t + m\vartheta\right)\ \sin\left(\frac{p\pi z}{L}\right) J'_m\left(\frac{\lambda'_{mn}}{R}r\right) \\
E_z &= 0 \qquad\qquad (2.93) \\
B_r &= \sum_{mnp} \left(\frac{p\pi}{\gamma_p L}\right)\ b_{mnp}\ \cos\left(\omega_{mnp}t + m\vartheta\right)\ \cos\left(\frac{p\pi z}{L}\right) J'_m\left(\frac{\lambda'_{mn}}{R}r\right) \\
B_\vartheta &= \sum_{mnp} \left(\frac{mp\pi}{rL\gamma_p^2}\right)\ b_{mnp}\ \cos\left(\omega_{mnp}t + m\vartheta\right)\ \cos\left(\frac{p\pi z}{L}\right) J_m\left(\frac{\lambda'_{mn}}{R}r\right) \\
B_z &= \sum_{mnp} b_{mnp}\ \cos\left(\omega_{mnp}t + m\vartheta\right)\ \sin\left(\frac{p\pi z}{L}\right) J_m\left(\frac{\lambda'_{mn}}{R}r\right)\ ,
\end{aligned}$$

where λ'_{mn} is the n^{th} zero of the derivative of the Bessel's equation of the first kind, J_m and $\gamma_p = \sqrt{\frac{\omega^2}{c^2} - \left(\frac{p\pi}{L}\right)^2}$ (see Eq. 2.82), and a TM_{mnp} mode:

$$\begin{aligned}
E_r &= \sum_{mnp} \left(-\frac{p\pi}{\gamma_p L}\right)\ a_{mnp}\ \cos\left(\omega_{mnp}t + m\vartheta\right)\ \sin\left(\frac{p\pi z}{L}\right) J'_m\left(\frac{\lambda_{mn}}{R}r\right) \\
E_\vartheta &= \sum_{mnp} \left(\frac{mp\pi}{rL\gamma_p^2}\right)\ a_{mnp}\ \sin\left(\omega_{mnp}t + m\vartheta\right)\ \sin\left(\frac{p\pi z}{L}\right) J_m\left(\frac{\lambda_{mn}}{R}r\right) \\
E_z &= \sum_{mnp} a_{mnp}\ \cos\left(\omega_{mnp}t + m\vartheta\right)\ \cos\left(\frac{p\pi z}{L}\right) J_m\left(\frac{\lambda_{mn}}{R}r\right) \qquad (2.94) \\
B_r &= \sum_{mnp} \left(\frac{m\omega_{mnp}}{r\gamma_p^2 c^2}\right)\ a_{mnp}\ \cos\left(\omega_{mnp}t + m\vartheta\right)\ \cos\left(\frac{p\pi z}{L}\right) J_m\left(\frac{\lambda_{mn}}{R}r\right) \\
B_\vartheta &= \sum_{mnp} \left(-\frac{\omega_{mnp}}{\gamma_p c^2}\right)\ a_{mnp}\ \sin\left(\omega_{mnp}t + m\vartheta\right)\ \cos\left(\frac{p\pi z}{L}\right) J'_m\left(\frac{\lambda_{mn}}{R}r\right) \\
B_z &= 0\ ,
\end{aligned}$$

where λ_{mn} is the n^{th} zero of the Bessel's equation of the first kind, J_m.

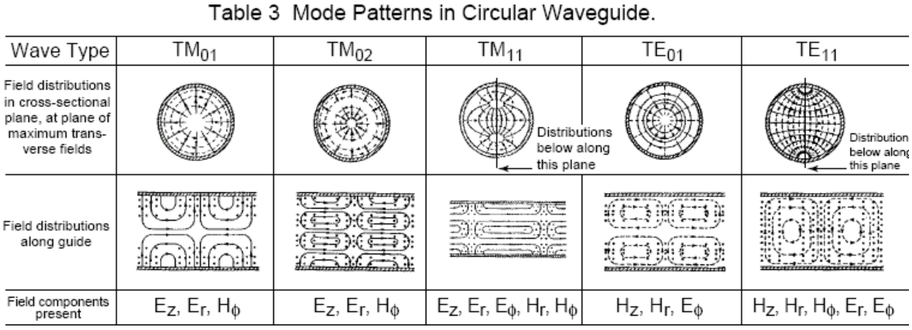

Table 3 Mode Patterns in Circular Waveguide.

Wave Type	TM_{01}	TM_{02}	TM_{11}	TE_{01}	TE_{11}
Field distributions in cross-sectional plane, at plane of maximum trans-verse fields			Distributions below along this plane		Distribution below alon this plane
Field distributions along guide					
Field components present	E_z, E_r, H_ϕ	E_z, E_r, H_ϕ	$E_z, E_r, E_\phi, H_r, H_\phi$	H_z, H_r, E_ϕ	$H_z, H_r, H_\phi, E_r, E_\phi$

Figure 2.8: Field patterns for several TE and TM modes in circular waveguide.

2.5.3 Eigenmodes in a pill–box cavity

From Eqs. 2.93 and 2.94, the expressions for the allowed resonant frequencies of the TE_{mnp} and TM_{mnp} modes in a cavity of radius R and length L are:

$$\omega_{mnp}^{TE} = c\sqrt{\left(\frac{\lambda'_{mn}}{R}\right)^2 + \left(\frac{p\pi}{L}\right)^2} \tag{2.95}$$

and

$$\omega_{mnp}^{TM} = c\sqrt{\left(\frac{\lambda_{mn}}{R}\right)^2 + \left(\frac{p\pi}{L}\right)^2} \,. \tag{2.96}$$

Thus, for a pill–box cavity, the solutions of the wave equations form two sets of modes, denoted transverse magnetic (TM) modes and transverse electric (TE) modes. TM modes have a longitudinal component of the electric field with respect to the cavity axis (z axis), whereas the magnetic field is transverse everywhere.

In contrast to this, TE modes have a longitudinal component of the magnetic field and the electric field is transverse everywhere. We saw above that the pill–box TM modes are classified by three integer indices m, n, p.The corresponding electric field in z direction is

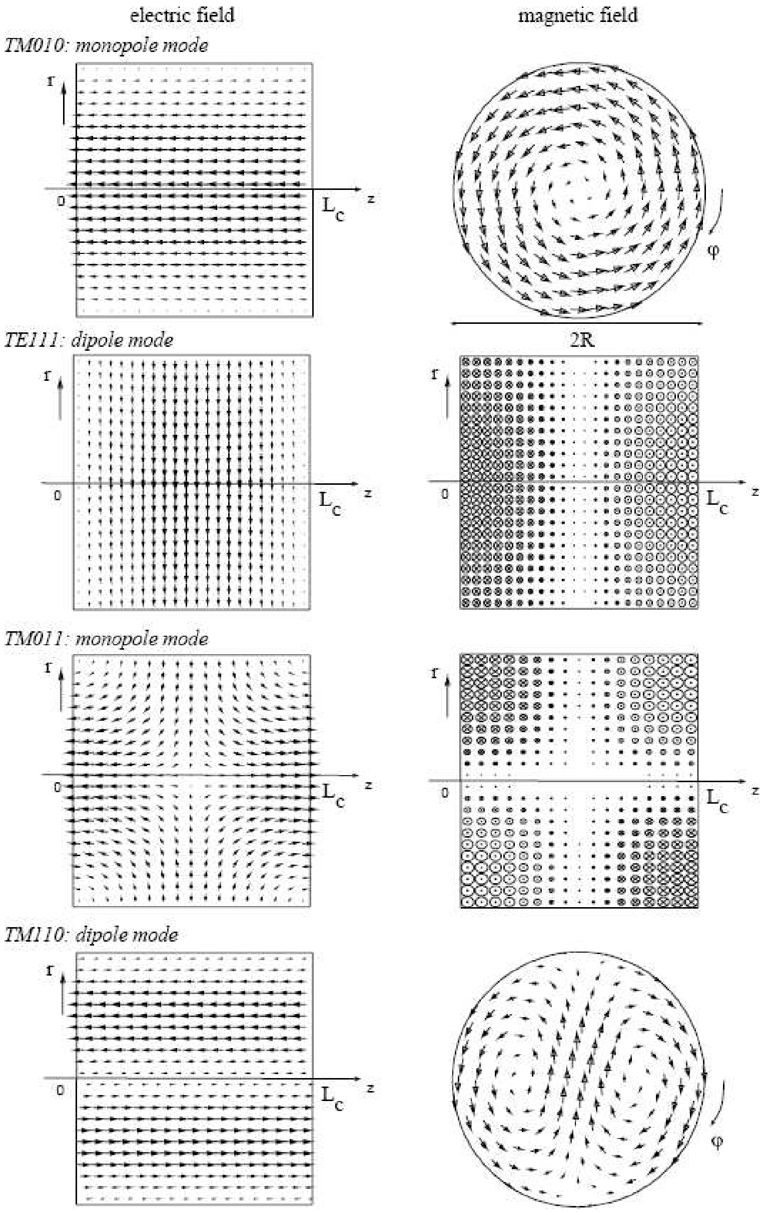

Figure 2.9: Vector plot for selected eigenmode fields in a cylindrical pill–box cavity. The size of the arrows indicates the relative amplitude of the electric field (left column) and the magnetic field (right column) within the cavity. By courtesy of Matthias Liepe.

$$E_z = \sum_{mnp} a_{mnp} \, \cos\left(\omega_{mnp} t + m\vartheta\right) \, \cos\left(\frac{p\pi z}{L}\right) J_m\left(\frac{\lambda_{mn}}{R} r\right) \; . \tag{2.97}$$

The meaning of this indices is as follows (for the TE–modes is similar):

- Modes with $m = 0$ are rotationally symmetric with respect to the cavity axis z. These so–called monopole modes have a non vanishing longitudinal component of the electric field at the beam axis, since $J_0(0) = 1$. Note that for all other Bessel function $J_m(0) = 0$, $m \neq 0$. Therefore only modes of the type TM_{0np} are useful for beam acceleration. Modes with $m = 1$ are called dipole modes because of their field distribution, see Fig. 2.9. These modes have a net deflection field on the beam axis and are therefore not suitable in accelerating cavities, but may be used to deflect a beam, as we shall see later. Further modes with $m = 2$ are called quadrupole modes, and so on.

- According to equation 2.97, the electric field vanishes at the cylinder wall of the pill–box ($r = R$) on account of the n^{th} root of J_m. Thus n gives the number of sign changes E_z, undergoes in radial direction.

- Finally the index p measures the number of sign changes E_z undergoes along the cavity axis (z direction).

TE modes are classified in a similar manner. In an ideal pill–box cavity the TE modes have no longitudinal electric field and thus cannot accelerate the beam nor can an on–axis beam excite them.

When many pill boxes are coupled together, each mode degenerate into as many coupled modes as the number of cells. The field lines are distorted, the modes are no longer purely TE or TM. Nevertheless one keeps the classification of *TM–like* and *TE–like* modes.

2.6 Shunt impendance and R/Q

In order to maintain an accelerating field in the cavity, it is necessary to store electromagnetic energy in the cavity. Since that energy ultimately comes from the electrical grid and has to be paid for, a useful quantity to calculate is the net acceleration achieved for a given quantity energy of dissipated power

$$R = \frac{|V|^2}{P_\lambda} \tag{2.98}$$

where P_λ is the power dissipated in the walls.

We will show that quality and loss factors, introduced previously in section 2.4.2, are related to the impedance R. The coupling between the wave and the charged beam is controlled by the loss factor, k_λ, which is characteristic for each mode λ. The quality factor Q_λ, describes the energy loss of mode λ which occurs primarily in the cavity walls. These parameters are defined analytically in the following way:

$$k_\lambda = \frac{|V_\lambda|^2}{4U_\lambda} \ , \qquad Q_\lambda = \frac{\omega_\lambda U_\lambda}{P_\lambda} \ ,$$

where V_λ is the voltage corresponding to mode λ along a path parallel to z, U_λ is the energy stored in the electromagnetic field of the mode and, as introduced in Eq. 2.98, P_λ is the power dissipated in the walls. Low losses imply a high Q_λ. These losses may be reduced by choosing a material with high conductivity, like a superconducting one, as in the case of the TESLA cavities. The parameter R/Q is often used, which is related to the loss factor through the equation:

$$\left(\frac{R}{Q}\right)_\lambda = \frac{4k_\lambda}{\omega_\lambda} = \frac{|V_\lambda|^2}{\omega_\lambda U_\lambda} \ , \tag{2.99}$$

where R is called the shunt impedance.

The energy density ε is given by ([Jac75], [Rei93]):

$$\varepsilon = \frac{1}{2}\left(\mathbf{E}\cdot\mathbf{D}^* + \mathbf{B}\cdot\mathbf{H}^*\right) \ , \tag{2.100}$$

or in another form (see also 2.37):

$$\varepsilon = \frac{1}{2}\left(\epsilon\mathbf{E}^2 + \frac{1}{\mu}\mathbf{B}^2\right) \ . \tag{2.101}$$

which becomes, using the electromagnetic components, and the indices seen previously:

$$\begin{aligned}\varepsilon_{mnp} = \frac{1}{2}\int_0^R\int_0^L\int_0^{2\pi}&\left[\epsilon\left(E^2_{r_{mnp}} + E^2_{\vartheta_{mnp}} + E^2_{z_{mnp}}\right) + \right.\\ &\left.+\frac{1}{\mu}\left(B^2_{r_{mnp}} + B^2_{\vartheta_{mnp}} + B^2_{z_{mnp}}\right)\right] \ \mathrm{d}\vartheta\cdot r \ .\end{aligned} \tag{2.102}$$

2.6.1 Energy gain

Let us now consider the energy gain through a cavity and once again the electric field. We can express the electric field on the axis as simply:

$$E_{z,mnp}(z,t) = \xi_{mnp}\cdot\exp[i(\omega t - kz)] \ , \tag{2.103}$$

where $\xi_{mnp} = \mathfrak{f}(r,\vartheta)$, from 2.97. The energy gain is given by:

$$e \ \mathrm{d}V_{mnp} = e\int_0^L \mathbf{E}\cdot \ \mathrm{d}\mathbf{l} \ . \tag{2.104}$$

If the beam is moving at the speed of light, in the longitudinal direction z, and parallel to the axis (Fig: 2.10), then we can write:

$$t = t_0 + z/c \ , \tag{2.105}$$

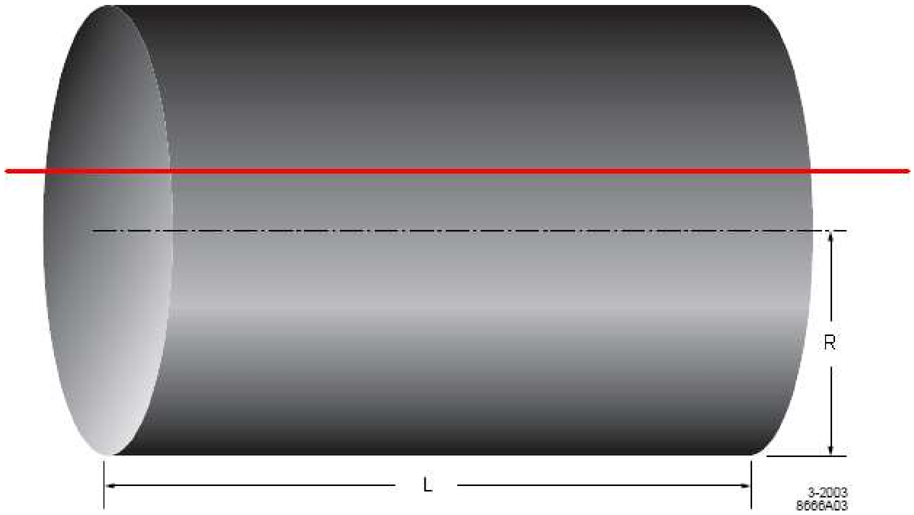

Figure 2.10: Parallel to the axis motion in a perfectly–conducting circular cylinder with radius R and length L

with t_0 the time at $z = 0$, and the energy gain, integrated over a distance dz, between $z = 0$ and $z = L$ as:

$$eV_{mnp} = e\int_0^L E_z\,\mathrm{d}z == e\xi_{mnp}\,\Re\Big\{exp\,(i\omega_{mnp}t_0)\int_0^L \mathrm{d}z\;exp\,[i\,(\omega_{mnp}/c - k_p)\,z]\Big\}\,, \tag{2.106}$$

where $k_p = \frac{p\pi}{L}$, L is the cavity length.
We define:

$$\psi_{mnp} = L\cdot\left(\frac{\omega_{mnp}}{c} - k_p\right)\ , \tag{2.107}$$

called *transit angles.* Recalling that TM_{mnp} and TE_{mnp} modes are standing waves and that such a mode is composed of a left–travellling wave and e right–travelling wave superimposed within the cavity, one can demonstrate the result [Ten03]:

$$\begin{cases} V_{mnp} = \frac{\xi_{mnp}L}{2}\left\{T_L cos\left(\omega_{mnp}t_0 + \frac{\psi_L}{2}\right) + T_R cos\left(\omega_{mnp}t_0 + \frac{\psi_R}{2}\right)\right\} \\ \\ \psi_{L,R}\ (Left\ and\ Right) = L\left(\frac{\omega_{mnp}}{c} \pm \frac{p\pi}{L}\right) \\ \\ T_{L,R}\ (Left\ and\ Right) \equiv \frac{sin\left(\psi_{L,R}/2\right)}{\psi_{L,R}/2}\ . \end{cases} \tag{2.108}$$

Let's now consider a particle moving along a straight trajectory which is not parallel to the z axis (2.11). In this case we express the electric field

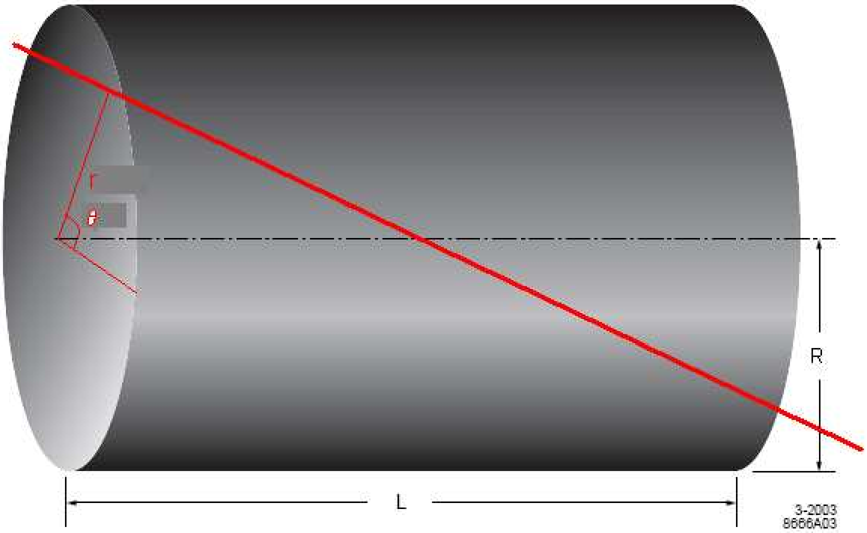

Figure 2.11: Motion in a perfectly–conducting pill–box with radius R and length L

as $\mathbf{E}(r(t), \vartheta(t), z, t = t_0 + \frac{s}{c})$, where s is the position along the particle path, then, the voltage becomes:

$$\begin{aligned} V_{mnp} = \int_{\sigma} \Big\{ & \xi_{r_{mnp}}\ exp\left[i\left(\frac{\omega_{mnp}s}{c}\right) - ikz\right] \quad \mathrm{d}\mathbf{s} + \\ & + \xi_{\vartheta_{mnp}}\ exp\left[i\left(\frac{\omega_{mnp}s}{c}\right) - ikz\right] \quad \mathrm{d}\mathbf{s} + \\ & + \xi_{z_{mnp}}\ exp\left[i\left(\frac{\omega_{mnp}s}{c}\right) - ikz\right] \quad \mathrm{d}\mathbf{s} \Big\} \ . \end{aligned} \tag{2.109}$$

Here σ is the particle trajectory, $\xi_{x_{mnp}} = \mathfrak{f}(r_\sigma, \vartheta_\sigma, z_\sigma)^4$, with $x = r, \vartheta, z$, and $\mathbf{s}\,(r_\sigma, \vartheta_\sigma, z_\sigma)$ is the unit vector along the particle path.
At this point it's enough to solve this line integral by using mathematical devices.

2.6.2 Matlab simulation

A Matlab program has been made to compute the Eq. 2.99 and find the value of R/Q characterizing each mode excited by the passage of a particle through a pill–box cavity, with any input angle and position by respect the cavity axis (Fig. 2.11). Solving Eq. 2.102 one can use the well known integrals, for $m, p \neq 0$:

$$\begin{cases} \int_0^{2\pi} \cos^2(m\vartheta) \quad \mathrm{d}\vartheta = \pi & \int_0^{2\pi} \sin^2(m\vartheta) \quad \mathrm{d}\vartheta = \pi \\ \int_0^{L} \cos^2\left(\frac{\pi p}{L} z\right) \quad \mathrm{d}z = \frac{L}{2} & \int_0^{L} \sin^2\left(\frac{\pi p}{L} z\right) \quad \mathrm{d}z = \frac{L}{2} \ , \end{cases}$$

---

[4] $(r_\sigma, \vartheta_\sigma, z_\sigma)$ are (r, ϑ, z) along the trajectory σ.

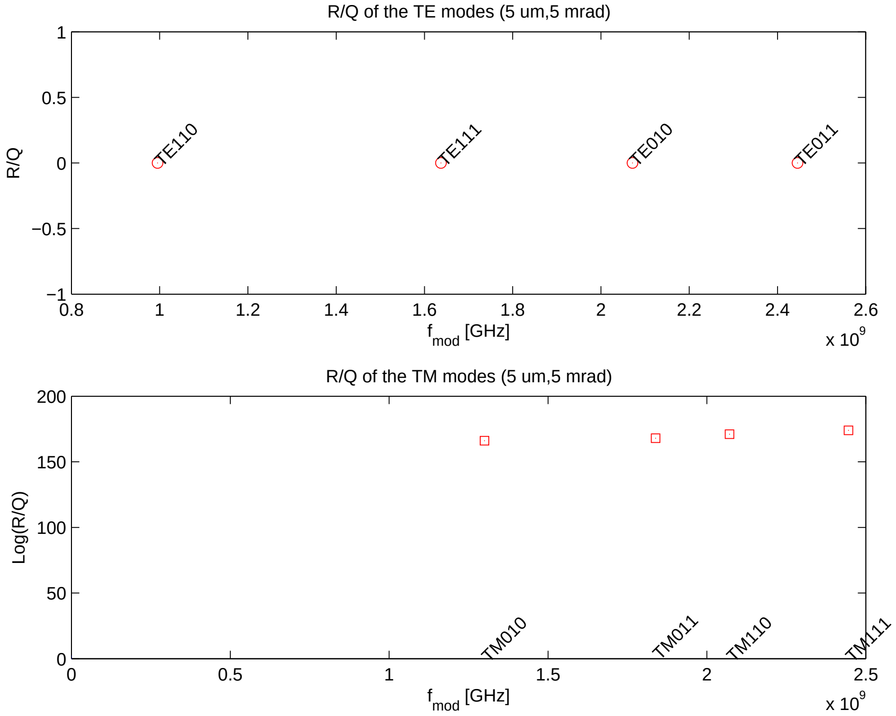

Figure 2.12: Parallel trajectory simulation. The particle enters with $\vartheta = 5\ mrad$ and $r = 5\ \mu m$ and moves parallel to the axis.

and the conservation of energy, to consider only time $t = 0$, and obtain two different expressions, for TE modes:

$$\begin{cases} \varepsilon^{TE}_{mnp} & = \frac{\epsilon\pi L}{4} b^2_{mnp} \frac{\omega^2_{mnp}}{\gamma^2_p} \int_0^R \mathrm{d}r \left[\frac{m^2}{r\gamma^2_p} J^2_m \left(\frac{\lambda'_{mn}}{R} r \right) + r J'^2_m \left(\frac{\lambda'_{mn}}{R} r \right) \right] \\ & + \frac{\pi L}{4\mu} b^2_{mnp} \left(\frac{\pi p}{L\gamma_p} \right)^2 \int_0^R \mathrm{d}r \left[J'^2_m \left(\frac{\lambda'_{mn}}{R} r \right) + \frac{m^2}{r\gamma^2_p} J^2_m \left(\frac{\lambda'_{mn}}{R} r \right) \right. \\ & \left. + \left(\frac{\gamma_p L}{\pi p} \right)^2 r J^2_m \left(\frac{\lambda'_{mn}}{R} r \right) \right] \\ \gamma_p = \frac{\lambda'_{mn}}{R} \ , & \end{cases} \tag{2.110}$$

or TM modes:

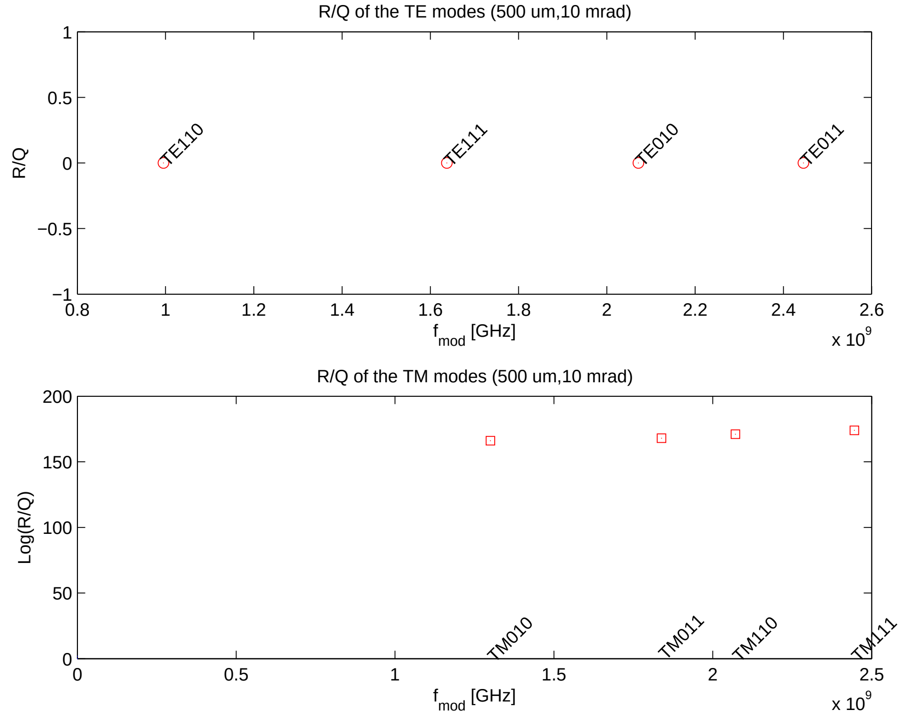

Figure 2.13: Parallel trajectory simulation. The particle enters with $\vartheta = 10\ mrad$ and $r = 500\ \mu m$ and moves parallel to the axis.

$$\begin{cases} \varepsilon^{TM}_{mnp} & = \frac{\epsilon\pi L}{4} a^2_{mnp}\left(\frac{p\pi}{L\gamma_p}\right)^2 \int_0^R r\ \mathrm{d}r \left[J'^2_m\left(\frac{\lambda'_{mn}}{R}r\right) + \frac{m^2}{r^2\gamma_p^2} J^2_m\left(\frac{\lambda_{mn}}{R}r\right) \right. \\ & \left. + \left(\frac{L\gamma_p}{p\pi}\right)^2 J^2_m\left(\frac{\lambda_{mn}}{R}r\right)\right] \\ & + \frac{\omega^2_{mnp} a^2_{mnp}\pi L}{4\gamma_p^2 c^4 \mu} \int_0^R r\ \mathrm{d}r \left[\frac{m^2}{\gamma_p^2 r^2} J^2_m\left(\frac{\lambda_{mn}}{R}r\right) + J'^2_m\left(\frac{\lambda_{mn}}{R}r\right)\right] \\ \gamma_p = \frac{\lambda_{mn}}{R}\ . & \end{cases} \tag{2.111}$$

The stored energy does not depend on the particle trajectory, while to calculate the voltage for a parallel trajectory we use Eq. 2.108, and for an angle trajectory we use Eq. 2.109 and solve the line integral along the trajectory. The results of this simulation are shown here. In an ideal pill–box cavity the TE modes have no longitudinal electric field and thus cannot accelerate the beam nor can the beam excite them for a parallel trajectory. Note that the R/Q values are in $[\Omega]$ for monopole modes and in $[\Omega/cm^2]$ for dipole modes.

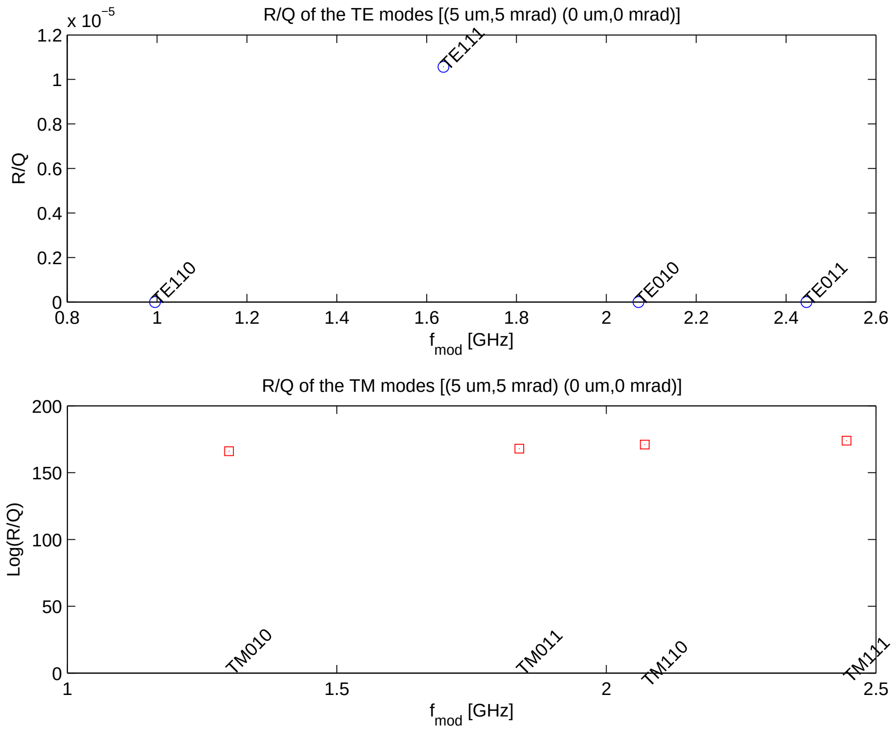

Figure 2.14: Not parallel trajectory simulation. The particle enters with offset of 5 μm and 5 mrad and goes out exactly in the geometrical cavity center.

The fundamental frequency is $f_{fund} = 1.3$ GHz, and the cavity length $L \approx 115.4$ mm is defined as half of the wave length corresponding to the fundamental mode and agrees with one cell length (see Fig. 1.7) in the TESLA cavities; the modes frequencies are calculated using Eqs. 2.95 and 2.96.

The requirement of a nonzero accelerating field on the axis of the cavity corresponds to a requirement that $m = 0$. Usually from the TM_{0n0} group of modes, the TM_{010} mode is chosen for beam acceleration because it has the lowest frequency and the simplest field pattern. For this reason here we take in account only $m, n, p = 0, 1$, since monopole modes are accelerating modes, while only dipole modes give radial fields on the z axis, and, as it will be shown, are useful in beam diagnostics because they are easily identifiable and their amplitude depends linearly on the beam offset from the cavity axis.

Modes with $m > 1$ generate fields only very close to the beam axis.

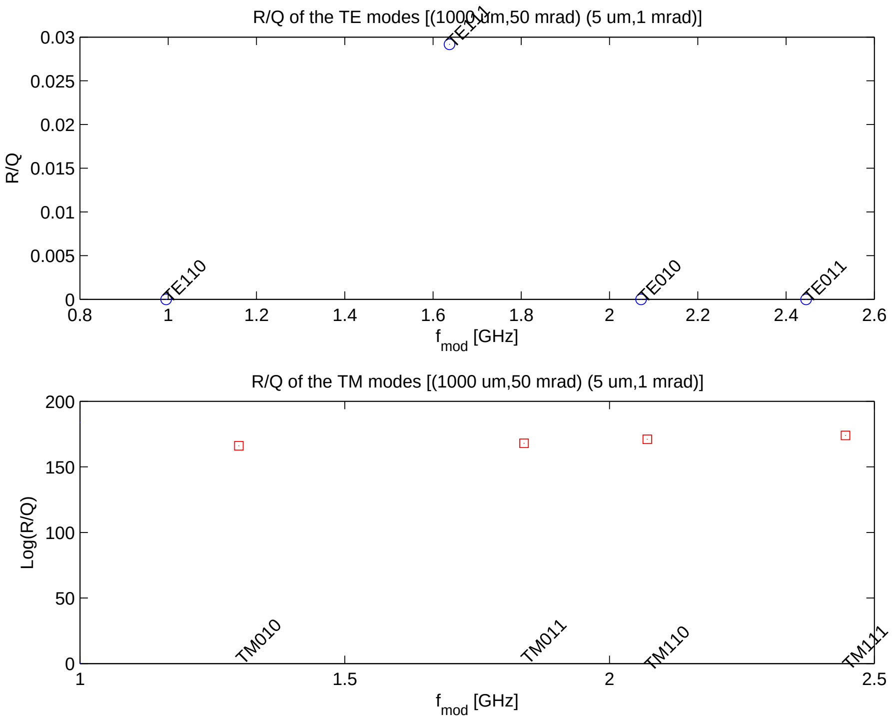

Figure 2.15: Not parallel trajectory simulation. The particle enters with offset of 1 mm and 50 mrad and goes out with offset of 5 μm and 1 mrad.

Figs 2.12 and2.13 show the results of simulating two parallel trajectories, with an offset of 5 μm, 5 mrad in the first figure, and of 500 μm, 10 mrad in the second one. In all the figures presented in this section the R/Q for the TM modes is expressed in logarithmic scale.

In Figs. 2.14 and 2.15 two not parallel trajectories are simulated. The first one shows a particle entering with an offset of 5 μm and 5 mrad, and going out exactly on the geometrical cavity center. In the second figure the particle enters with an offset of 1 mm and 50 mrad and the exit point has an offset of 5 μm and 1 mrad.

2.6.3 Wake fields in a pill–box cavity

The longitudinal and transverse wake potential produced by a charge passing on the axis of a cylindrically symmetric pill–box cavity can be computed in terms of the mode frequency ω_λ and loss parameter values k_λ, using the formalism shown in the previous sections. For longitudinal modes $(m = 0)$ the frequencies are obtained from:

$$\frac{\omega_{np}^2}{c^2} = \left(\frac{j_n^2}{R}\right)^2 + \left(\frac{\pi p}{g}\right)^2 \ . \tag{2.112}$$

Here R is the cavity radius, g is the cavity length, j_n is the n^{th} zero of $J_0(x)$ and the index p gives the longitudinal variation of the axial electric field,

$$(E_z)_{np} \sim J_0\left(j_n \ \frac{r}{R}\right) \ cos\left(\frac{\pi p z}{g}\right) \ exp\left(i\omega_{np}t\right) \ . \tag{2.113}$$

The delta–function wake potential is calculated (see for example [Wei81]) as

$$W_z(s) = \frac{4}{\pi\epsilon_p g}\sum_{n=1}^{\infty}\sum_{p=0}^{\infty}\epsilon_0 \ \frac{1-(-1)^p \ cos\left(\omega_{np}g/c\right)}{j_n^2 \ J_1^2(j_n)} \ cos\left(\omega_{np}\frac{s}{c}\right) \ , \tag{2.114}$$

where $\epsilon_0 = 1/2$, $\epsilon_p = 1$ for $p \neq 0$. If s is set to zero in the preceding relation, the sum diverges with increasing mode number, although only logarithmically. Thus a point charge passing through a completely closed pill–box suffers an infinite energy loss. For a Gaussian charge distribution this is no longer the case. The potential at position z for a bunch centered at $z = 0$ is given by ([Wei81]):

$$V(z) = \frac{2Q}{\pi\epsilon_0 g} \ e^{-z/2\sigma^2}\sum_{n=1}^{\infty}\sum_{p=0}^{\infty}\epsilon_0 \ \frac{1-(-1)^p \ cos\left(\omega_{np}g/c\right)}{j_n^2 \ J_1^2(j_n)} \ \Re\left\{\varpi\left(\frac{\omega_{np}\sigma}{c\sqrt{2}} - \frac{\mathbf{i}z}{\sigma\sqrt{2}}\right)\right\} \tag{2.115}$$

where $\varpi(z)$ is the complex error function, σ the r.m.s of the Gaussian charge distribution, and $\Re$ stands for the real part. No closed expression is known for this sum, but it has been evaluated numerically for sample cases.

For $s < (4R^2+g^2)^{1/2}-g$, the sum in Eq. 2.114 for the delta–function wake can be evaluated analytically. For the above range of s, no wave created by leading charge can reach the outer cylindrical wall of the cavity, be reflected and arrive back at the test charge before it has left the cavity. The pill–box cavity wake therefore looks identical to the wake for two parallel plates over this range of s. Over this range it can be shown that ([Wei81],[Cha75]):

$$\begin{aligned} 2\pi\epsilon_0 W_z(s) = {} & 2\delta(s) ln\left(\frac{g}{s}\right) - 2\sum_{n=1}^{\infty}\delta\left(2ng-s\right)\ ln\left[\frac{s^2}{(s+g)(s-g)}\right] \\ & -\frac{1}{g}\left\{\frac{1}{\left[\frac{s}{2g}\right]_{IP}+\frac{s}{2g}} - \frac{1}{\left[\frac{s}{2g}\right]_{IP}+\frac{s}{2g}\ +1}\right\}, \end{aligned} \tag{2.116}$$

where the symbol IP means the integer part of the term in brackets. Note that the wake is accelerating for all $s > 0$, even in the delta–function discontinuities given by the second term in the above expression. The combination of a delta–function discontinuity times a logarithmic discontinuity given by

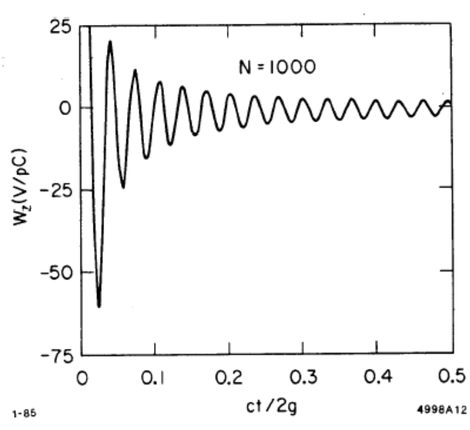

Figure 2.16: Longitudinal wake for a pill-box cavity ($g = 3$ cm, $R = 4$ cm) obtained by summing the first 1000 modes.

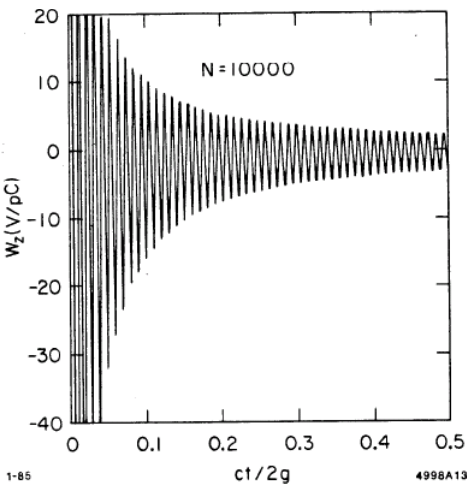

Figure 2.17: Longitudinal wake for a pill-box cavity (10000 modes).

the first term above is, however, retarding.

It is instructive to compare the results of the summation of modes up to mode N (Eq. 2.114) with the analytic result of Eq. 2.116. The summation is carried out for the case $s < 2g$ in Figs. 2.16 and 2.17. Note that as N increases, the resultant sum yields an oscillation of increasing frequency. In the limit $N \rightarrow \infty$, we would expect the delta–function wake constructed in this way to oscillate infinitely fast. The convolution of the wake function with a smooth bunch current distribution however, is well behaved. this illustrates an important property of a Green's function. The function itself need not be well behaved, only integrals over the function are.

Chapter 3

Preliminary study on HOM–based alignment

The aim of this chapter is to present a series of experiments made by using a spectrum analyzer to estimate the amplitude of higher order modes (HOM) excited by the beam. The interaction of the beam with the higher order modes in the TESLA cavities has been studied in the past at the TTF1 linac, in order to determine whether the modes with the highest loss factor are sufficiently damped. These experimental studies lead to the discovery of the effect of the 2.585 MHz of the 3^{rd} dipole passband. They also confirmed that the damping of the first two dipole passbands was adequate. We will review these results in the first part of this chapter.
The same modes can be used actively for beam alignment. At TTF2 a first study on the beam alignment based on the HOM signals has been made in the first cryo-module, containing 8 accelerating cavities. Four modes with highest R/Q in the first two cavities have been used and their excitations from a single bunch beam have been carefully measured.
The main result of these measurement has been:

1) the discovery of the 4 mm misalignment of the first TTF cryomodule with respect to the gun;

2) the demonstration that a 50 μm resolution could be achieved.

The cavity center could be found for each of the modes, and the results of this study are presented in the following chapter.

3.1 Up to 2003: HOM excitation with an Intensity Modulated Beam

In order to describe the experiments performed at the TESLA Test Facility during the period of this thesis, we want to introduce the starting point from where our program has been conceived and began in 2003.

A beam experiment was conducted in 1998 on the first accelerating module of the TTF linac, to investigate transverse higher order modes in the super-conducting cavities.

By injecting the beam with a transverse offset and by modulating the intensity of the 216 MHz bunch train with a tunable frequency in the 0–108 MHz range, transverse HOMs can be excited resonantly.

In fact, if the modulation frequency ω_{mod} is varied from 0 to $\omega_b/2$, with $\omega_b = 2\pi/t_b$ the bunch repetition angular frequency, all modes can be excited, when the following resonance relation is fulfilled:

$$\omega_{mod} = |\omega_l - m \cdot \omega_b| \ , \tag{3.1}$$

where ω_l is the angular frequency of the excited mode and m an integer.

Single modes have been excited by a charge modulation:

$$q_n = q_0(1 + \lambda \cdot \sin(n\omega_{mod}t_b + \phi)) \ , \tag{3.2}$$

where n is the bunch index, q_0 the average charge, t_b the bunch spacing,

ω_{mod} the angular frequency of the modulation signal. λ is the modulation amplitude and ϕ its initial phase [Bab01]. The transverse wake potential seen by the bunch with the index n in the train contains the contributions of the wakes excited by all previous bunches, being proportional to:

$$W_\perp(t) \propto \sum_{k=1}^{n-1} q_k W_\perp^\delta((n-k)ct_b) \ , \tag{3.3}$$

where $W_\perp^\delta$ is the delta–like transverse wake potential [Bab01] per accelerating structure. The bunches are considered to be point–like because $\sigma_z \ll \lambda_l = 2\pi c/\omega_n$, where σ_z is the beam size (r.m.s.) in the z direction and λ_l is the wavelength of the mode l.

If a mode is excited on resonance it results that the offset amplitude Δx, i.e. the difference between the extreme transverse position in the bunch, at a certain location after the cavity, is given by:

$$\begin{aligned} \Delta x = \delta x_{max} - \delta x_{min} &= R_{12} \propto (\delta x'_{max} - \delta x'_{min}) \\ &= c\ \delta x_0 \lambda \left(q_0 \frac{\omega_b}{2\pi}\right) \frac{e}{E} \frac{1}{\omega_l} \left(\frac{R}{Q}\right)_l Q_l \ , \end{aligned} \tag{3.4}$$

where δx_0 is the constant initial offset of the bunches with respect to the cavity axis, λ is the modulation amplitude, e is the electron charge, and E is the energy of the bunches in the middle of the cavity [Bab01].

In 1998 a HOM experiment with modulated beam intensity has then been carried out with an older setup of TTF, when injector 1 was used to generate electron bunches. The experimental set–up is shown in Fig. 3.1.

The experiment consisted in sending off–axis long bunch train with intensity modulation through an acceleration cavity [Far99]. By slowly varying of the modulation frequency ω_{mod} the resonance condition given by Eq. 3.1 was met for each mode. The transverse positions of the bunches, after the excited cavity, are monitored with a BPM.

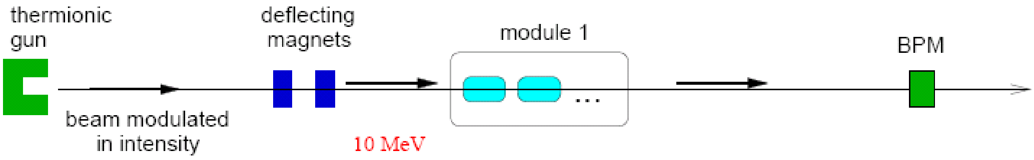

Figure 3.1: Experimental set–up used in 1998. The intensity modulated beam generated by the thermionic gun receives an offset with the help of a dogleg deflecting magnet pair. When a mode is excited in one cavity of module 1, its effect on the bunch offsets is measured at the BPM.

By doing this excitation, a beam instability was observed on the broadband BPM for $f_{mod} = 15.0022$ MHz with a short beam pulse of 35 μm and 5 mA current, and a large injection offset of about 20 mm. The beam pulse length could be increased to up to 500 μs while remaining on the HOM resonance. Fig. 3.2 shows the comparison of the BPM envelope signals with charge modulation off or on for a 400 μs long beam pulse.

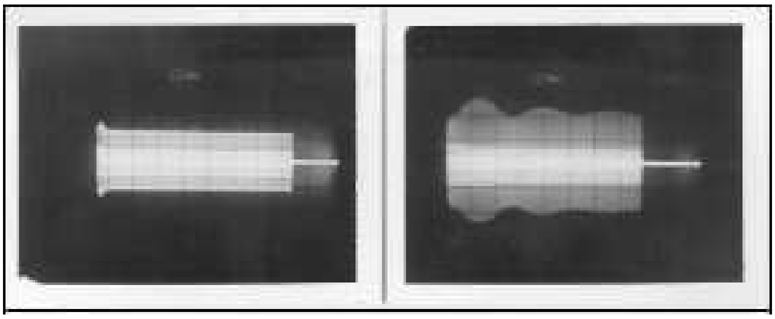

Figure 3.2: BPM difference signal showing evidence for a HOM resonance (right) in comparison to the signal for the unmodulated beam (left). The abscissa represents the time axis, while the ordinate is the BPM difference signal. The pulse length is 400 μs.

With modulation off, the broadband BPM integrates a high but constant

100 mV level of beam induced noise, although the beam is steered through its center. This is due to the rejection of the *sum* signal into the *difference* signal BPM antennas. While the modulation is on, the beam offset reaches a maximum of about 10 mm but, due to the excessive noise no quantitative measurement could be made. A damped oscillatory behavior of the envelope signal is visible in Fig. 3.2 with a period of about 125 μs, on top of the constant envelope of the beam oscillations reached at the steady state. This behavior was later explained, and reproduced by simulation [Bab01], by the fact that the modulation frequency was off HOM–resonance by about 8 kHz (1/125 μs). The resonant oscillations then reach a steady state after some damped overshooting. Simulations predict that for a perfectly on–resonance excitation, the oscillations reach the aperture limit within the 35 μs short pulse: this agrees with the observed veto from the beam loss protection system occurring at every attempt to fine tune the modulation frequency towards lower values of f_{mod}.

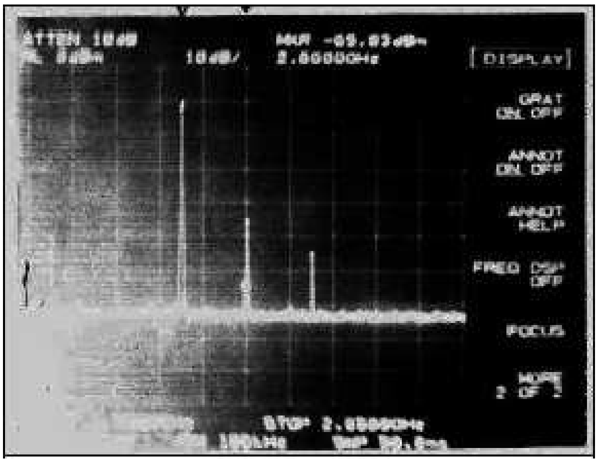

Figure 3.3: Sidebands around the 2.6 GHz beam harmonics.

The beam experiment revealed the existence of a HOM with a frequency $f_{HOM} = nf_b \pm$(15.022 MHz–8 kHz) in the accelerating module. While detuning cavities 1 and 2 had no effect on the beam instability, detuning cavity

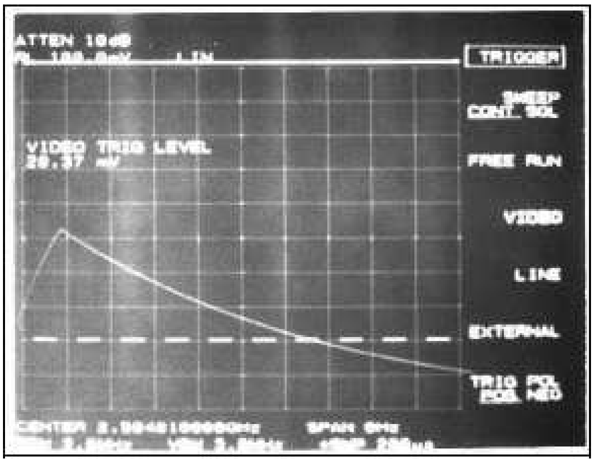

Figure 3.4: Time domain signal from HOM pickup on the 2585 MHz mode.

3 by about ±16 kHz in the fundamental mode did suppress the instability. It was then possible to measure and identify the mode at the HOM coupler outputs of cavity 3 with a spectrum analyzer. The frequency domain signal around the 2.6 GHz beam harmonics in Fig. 3.3 shows a beam modulation side–band peak enhanced by HOM resonance on the low side of this harmonics. The same signal, when analyzed in time domain in Fig. 3.4, shows the 35 μs beam–pulse cavity loading, followed by the relaxation of the field amplitude with a characteristic time $\tau = 110$ μs. The dipolar nature of the mode was demonstrated by checking the perfect linear dependance of the height of the amplitude maximum with the offset of the beam entering the module, over a range from 0 to 20 mm.
This method of identifying a dipole HOM frequency with a spectrum analyzer in the frequency domain, and then of doing a quantitative analysis from the time domain signal obtained by centering the spectrum analyzer on the HOM frequency with a finite bandwidth ($\Delta f \approx 300$ kHz), is the basis of all the investigations and results presented in this chapter.

The resonant modes of cavity 3 were studied over a wider range of frequencies with a network analyzer while the beam was turned off. As shown by Fig. 3.5, the measured HOM was the highest frequency mode of the 3^{rd} dipole pass-band. Its frequency was $f_{HOM} = 2584.986$ MHz ± 1 kHz. The damping factor was then given by [Far99]:

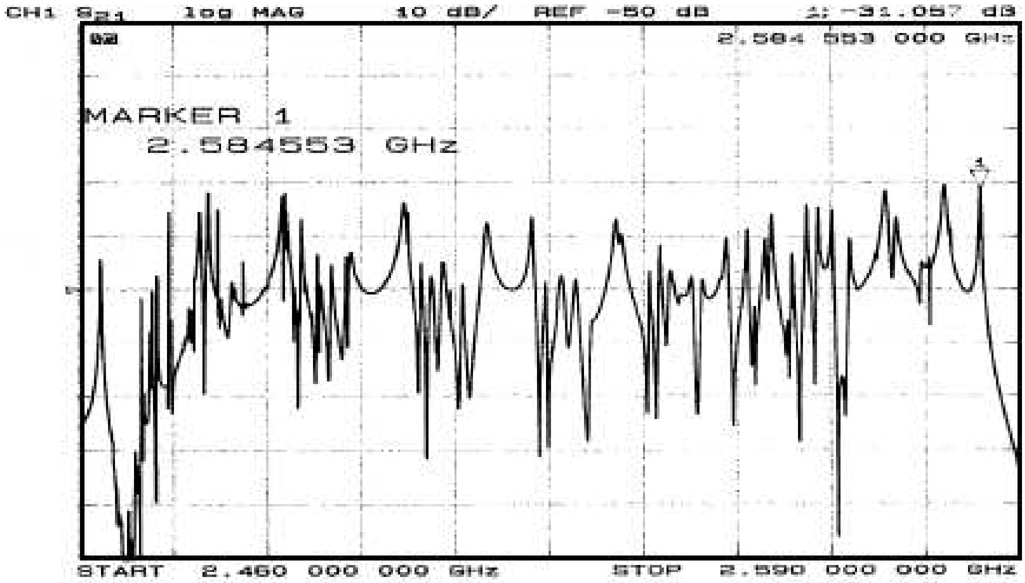

Figure 3.5: Third dipole pass-band of cavity 3. The vertical scale is in 10 dB per division.

$$Q = \frac{2\pi f_{HOM}\tau}{2} \approx 10^6 \ , \tag{3.5}$$

where τ is the decay constant.

The quite strong maximum kicks on the bunches, even for short pulses of 35 μs, indicates that the mode should have a high R/Q as well.
The time allocated for this experiment allowed the study of three more modes. None of them was as pronounced as the one described above. All modes are listed in table 3.1.

The spectrum of each cavity consists of resonant modes grouped in pass-bands (see Fig. 3.6) according to their TM or TE mode type. There are 9 modes in each passbands, and for the case of dipole modes there are 2

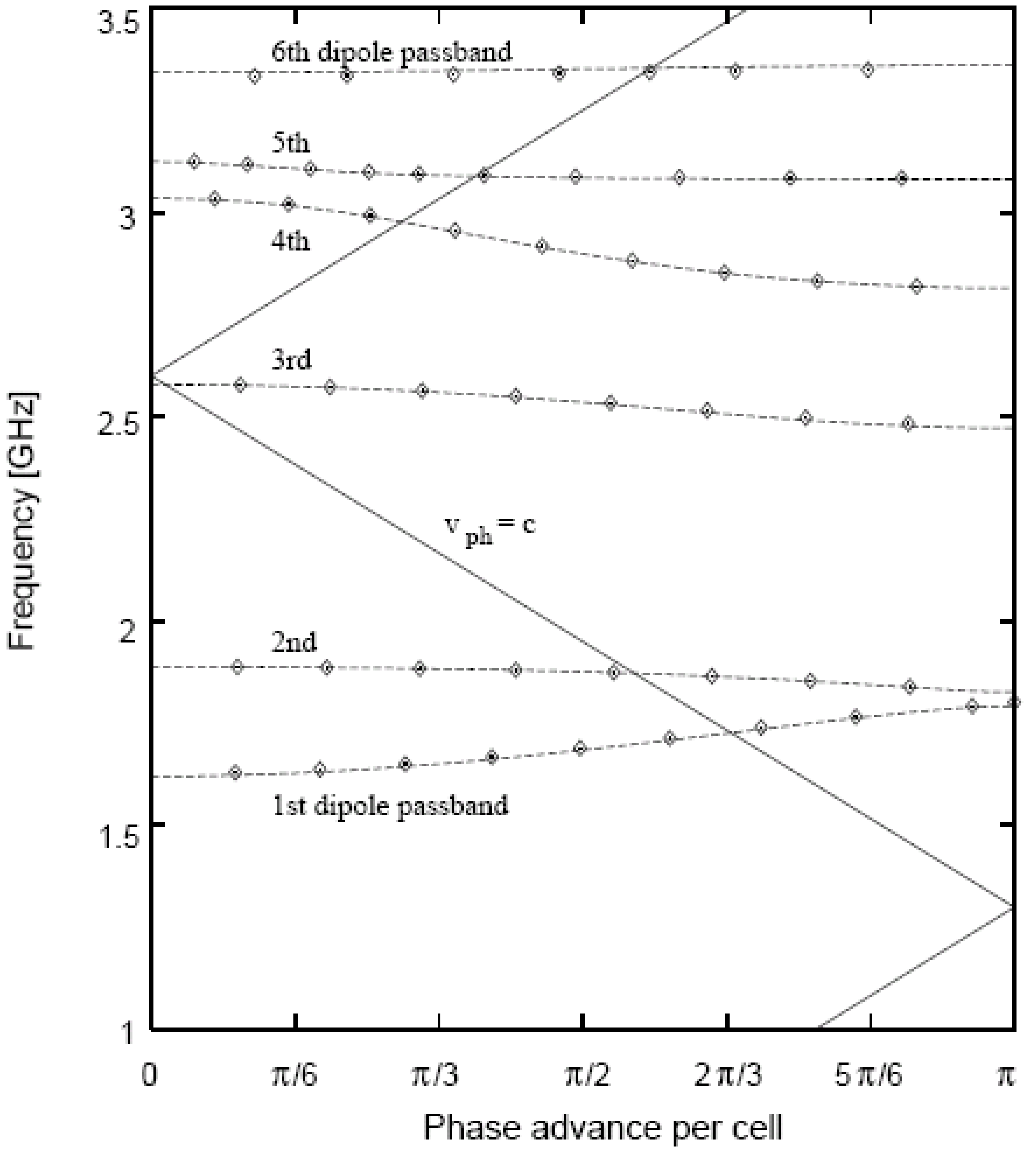

Figure 3.6: Dispersion diagram for the dipole modes of TESLA cavity. The diamond symbols represent individual modes. The velocity of the light line is shown as well. Its intersection with the passbands marks the modes with highest coupling to the beam

polarizations for each mode.

The 10 dipole modes listed bold type in table 3.1 were considered in this

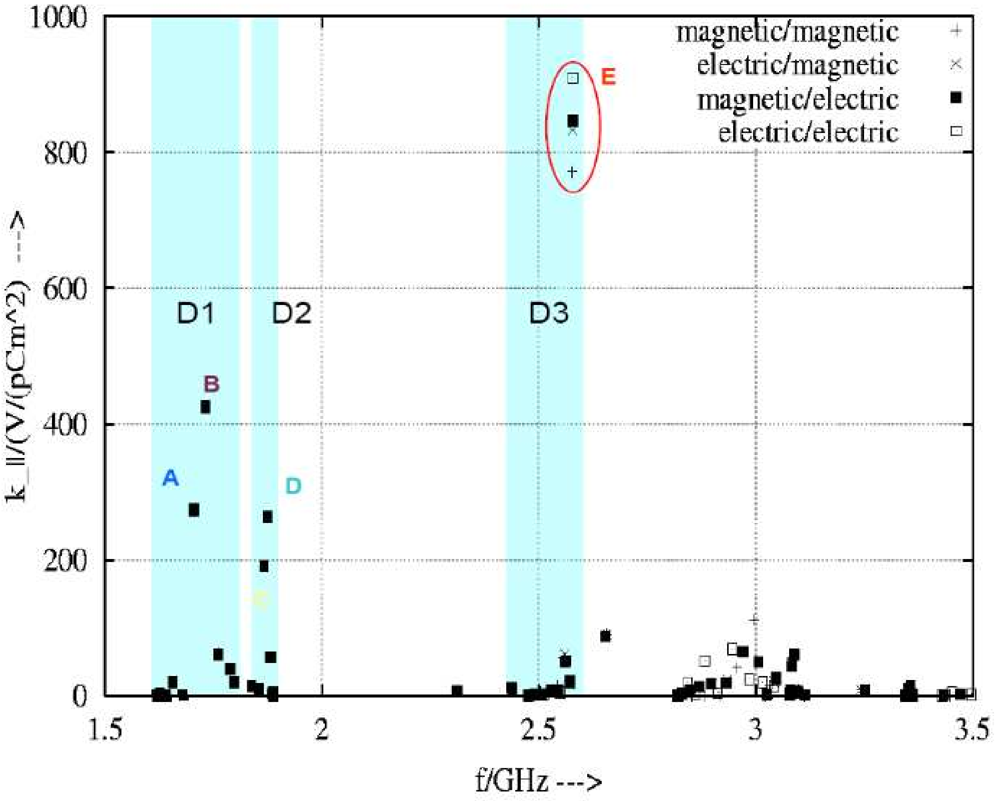

Figure 3.7: Loss factors for the 1st, the 2nd and the 3rd dipole passbands.

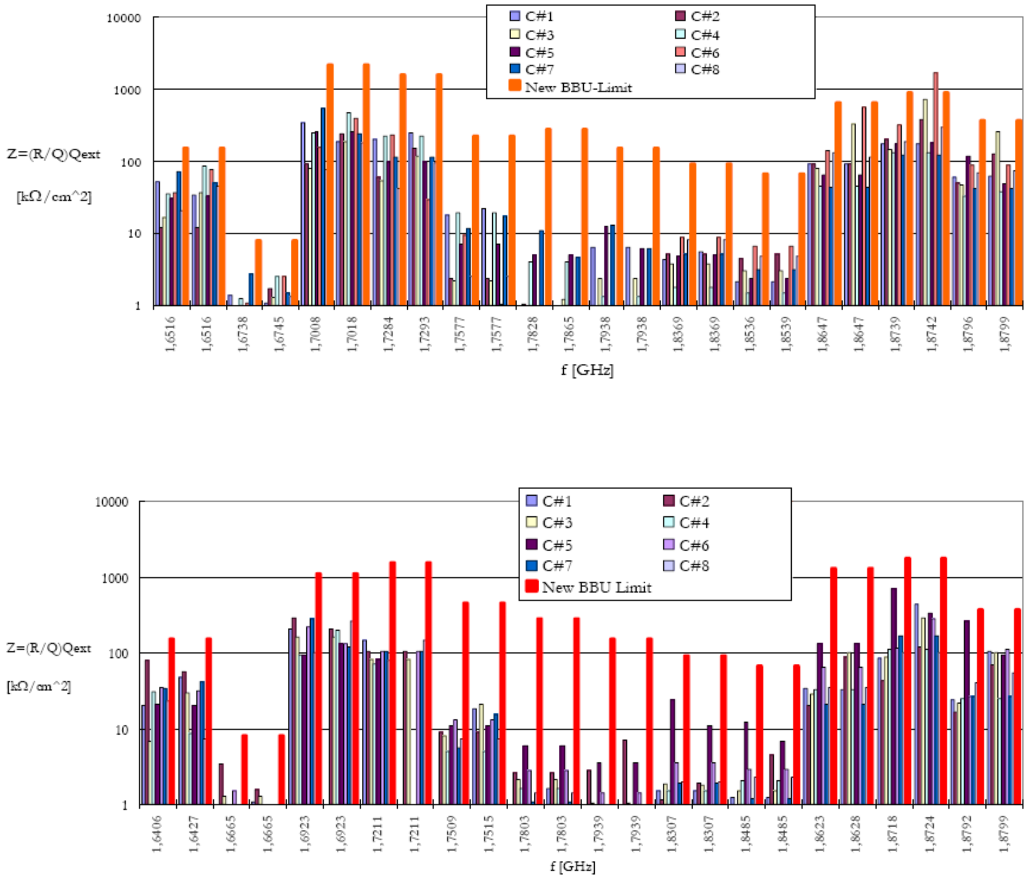

Figure 3.8: Damping of the first two transversal passbands, respectively for the cryomodules ♯1 and ♯2.

study (see also Fig. 3.9). Measurements with a beam modulated in intensity indicated modes with very high quality factors in several cavities, and their insufficient damping. Investigations in the RF laboratory showed that a reason for the poor damping were the boundary conditions imposed by the neighboring cavities. Depending on the frequency of these modes in different cavities which are connected by beam tubes, the electromagnetic field can have such a distribution that it couples badly to the HOM dampers. Nevertheless, the poor damping occurs only in few cavities, which indicates that

$\omega_{mod}/(2\pi)$ $[MHz]$	$\omega_l/(2\pi)$ $[GHz]$	$(R/Q)_l$ $[\Omega/\text{cm}^2]$	τ_l $[\mu\text{s}]$	Q_l	passband	cavity
15.022	2.585	15	110	$9 \cdot 10^5$	3^{rd} TE	3
14.04	2.586	15	8	$6.5 \cdot 10^4$	3^{rd} TE	6
22.475	2.5775	1	22	$1.8 \cdot 10^5$	3^{rd} TE	3
74.03	1.876	9	20	$1.2 \cdot 10^5$	2^{nd} TM	3

Table 3.1: HOMs excited by an intensity modulated beam generated by injector 1.

it can be avoided and anyway it is in agreement with the TESLA tolerances [Wan01].

For the first two dipole passbands D1 and D2 in Fig. 3.7, Fig. 3.8 shows that the damping is sufficient in such a way that the decay time $\tau = 2Q/W$ is a fraction of the beam pulse 1 ms duration.

Now we are going to use the modes in table 3.2 to measure the relative beam position, by respect to the mode axis. Notice that the effect of the beam angle with respect to the cavity axis was ignored in this experiment. It has been studied and our analysis refined later, when two additional steerers were installed in the TTF2 injector.

3.2 Polarizations, beam position resolution and HOM centers

The HOM signal can be used to monitor the offset of the beam with respect to the cavity axis, since their amplitude is proportional to it. Monitoring the beam offset relative to the individual cavity axis would be extremely helpful

Frequency $[GHz]$	Loss factor $[V/pC/m^2$ $/9-cells]$	R/Q $[\Omega/cm^2$ $/9-cells]$
$\mathbf{TE_{111}}$–like		
1.6291	0.1	0.0028
1.6369	3.3	0.1272
1.6497	0.1	0.0030
1.6671	19.7	0.7534
1.6885	3.6	0.1368
1.7129	**297.8**	**11.067**
1.7391	**425.4**	**15.5704**
1.7656	**58.2**	**2.0984**
1.7912	45.3	1.609
$\mathbf{TM_{110}}$–like		
1.8004	20.0	0.7084
1.8391	**14.1**	**1.4168**
1.8535	**7.7**	**2.8336**
1.8650	**186.5**	**6.365**
1.8736	**264.2**	**8.9774**
1.8795	**62.0**	**2.1002**
1.8834	**1.2**	**0.0420**
1.8858	4.8	0.1616
1.8871	**0.1**	**0.0030**

Table 3.2: R/Q for the two passbands TE_{111} and TM_{110}.

to check the alignment and eventually reduce the emittance growth in the TTF linac. In a linear collider it would, for instance, enable one to optimize the orbit bumps needed to reduce the transverse wake effect, to localize any badly misaligned module, or to control the beam position and alignment.
First studies on the possibility to align the beam in the cavities have been

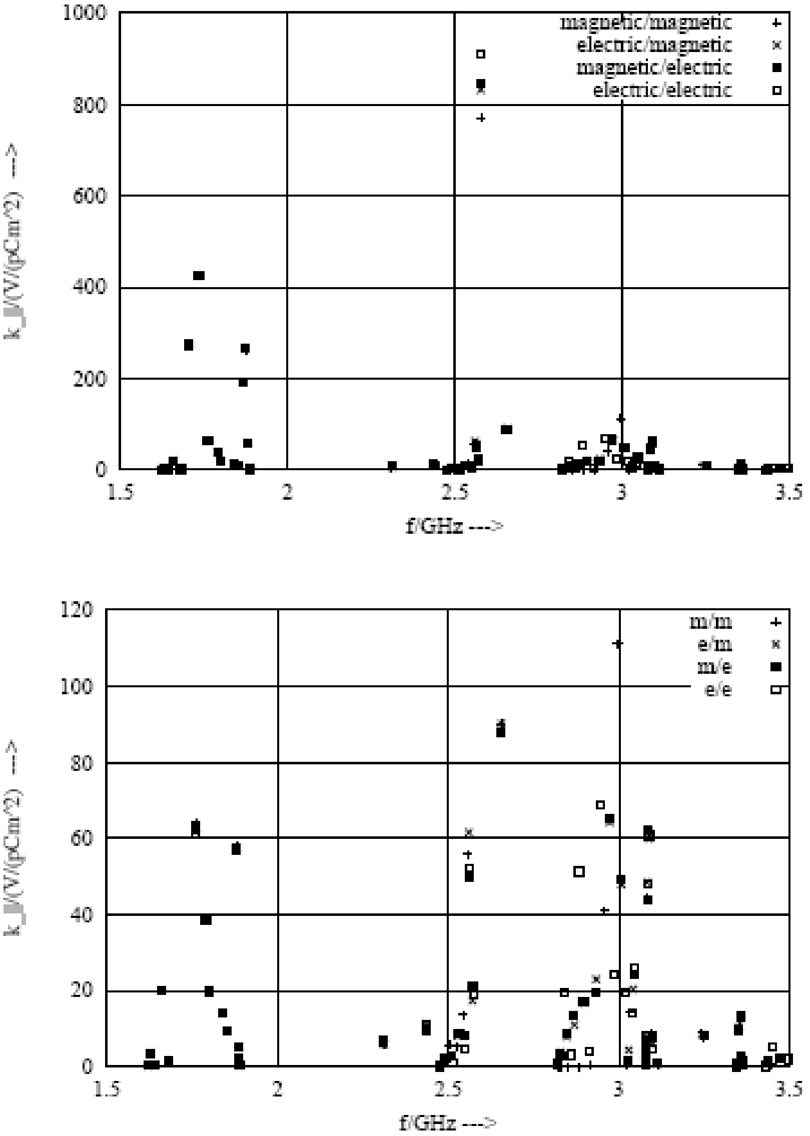

Figure 3.9: Dipole loss parameters for different boundary conditions (left beam pipe 84.15 mm, right beam pipe 86.51 mm). The upper diagram shows the full ordinate range while the ordinate scale in the lower diagram is expanded. By courtesy of Martin Dohlus.

made. The amplitude of the fields excited by the beam at several resonances in the first two cavities of the first TTF module has been measured as a function of the beam position.

Fig. 3.10 shows schematically the first part of the TTF–phase 2 (TTF2) [Faa02] injector. The RF gun accelerates the electrons emitted by a photo–cathode to 4.5 MeV. A horizontal and vertical steerer can deflect the beam, correcting for possible errors in the transverse and angular alignment of the gun. Eight cavities in module ACC1 accelerate the beam with a gradient of 12 MV/m.

The frequency spectrum of the wake fields excited by the beam is monitored with a spectrum analyzer.

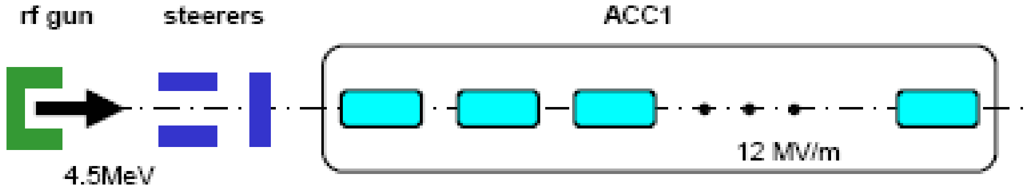

Figure 3.10: Schematic view of the alignment setup.

Four modes with highest R/Q have been used. Their frequencies and R/Q as predicted from simulations for an ideal TESLA cavity are shown in Table 3.2.Fig. 3.11 shows such a spectrum for the 6^{th}mode of the first dipole passband of the first cavity. The two polarizations can be distinguished and their quality factors Q, of about $9.3 \cdot 10^3$ and $2.4 \cdot 10^4$, have been measured a priori with a network analyzer.

3.2.1 The method

By the help of the horizontal and vertical steerers, the beam position in the cavity studied could be varied. The beam position with respect to the case of un–deflected beam (i.e. all steerers between the gun and the module are

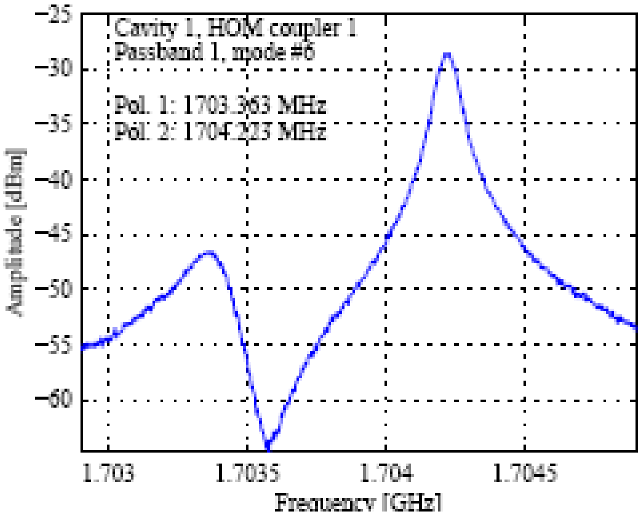

Figure 3.11: Mode ♯6 of the first dipole passband in cavity 1 of ACC1.

Dipole passband	Mode ♯	Frequency (simulation)	R/Q [MΩ/m^2]
1 (TE–like)	6	1713.7	11.21
	7	1738.3	15.51
2 (TM–like)	4	1864.7	6.54
	5	1872.7	8.69

Table 3.3: Dipole modes with highest R/Q used for monitoring, as predicted by simulations.

off) was calculated based on the steerer calibration and the transfer matrix [Bry92] from the steerer to the middle of the cavity.

Transmission of the position–velocity vector of a particle through a section of a transfer line, can be in fact simply represented by a 2 × 2 matrix (Fig. 3.12):

$$\begin{pmatrix} y_2 \\ y_2' \end{pmatrix} = \begin{pmatrix} C & S \\ C' & S' \end{pmatrix} \begin{pmatrix} y_1 \\ y_1' \end{pmatrix} = M_{1\to 2} \begin{pmatrix} y_1 \\ y_1' \end{pmatrix} . \tag{3.6}$$

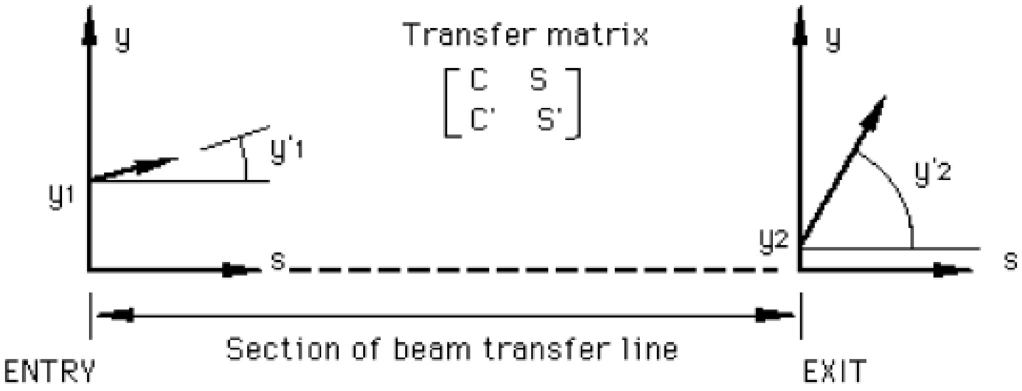

Figure 3.12: Transmission through a section of lattice (y represents either transverse coordinates).

The transfer matrix $M_{1\rightarrow 2}$ can be found by multiplying together the transfer matrices for the individual elements (magnets, drift spaces, cavities etc.) in the appropriate order. The individual of the quadrupoles matrices have the form:

$$M_y = \begin{pmatrix} \cos\,(or\cosh)\phi & \frac{L}{\phi}\sin\,(or\sinh)\phi \\ -\frac{\phi}{L}\sin\,(or-\sinh)\phi & \cos\,(or\cosh)\phi \end{pmatrix} \tag{3.7}$$

where

$$\phi = L\sqrt{|K|} \quad \text{and} \quad |K| = \left|\frac{1}{B\rho}\frac{\mathrm{d}B_y}{\mathrm{d}x}\right| \ ,$$

and L is the length of the element. The transfer matrix for the RF cavities is given by the so–called Chamber matrix [Chm65]:

$$\begin{pmatrix} \cos\alpha - \sqrt{2}\cos\left(\phi_{RF}\left(z\right)\right)\sin\alpha & \sqrt{8}\frac{\gamma_{in}(z)}{\overline{\gamma}'(z)}\cos\left(\phi_{RF}\left(z\right)\right)\sin\alpha \\ -\frac{\overline{\gamma}'(z)}{\gamma_{out}(z)}\left(\frac{\cos(\phi_{RF}(z))}{\sqrt{2}} + \frac{1}{\sqrt{8}\cos(\phi_{RF}(z))}\right) & \sin\alpha\ \frac{\gamma_{in}(z)}{\gamma_{out}(z)}\left(\cos\alpha\ + \sqrt{2}\cos\left(\phi_{RF}\left(z\right)\right)\sin\alpha\right) \end{pmatrix} \tag{3.8}$$

where the notations used are the following:

- s is the abscissa along the cavity axis;
- $\phi_{RF} \equiv \phi_{RF} - \omega_{RF} z/c$ is the RF phase seen by a particle which is at the relative position z within the bunch[1] and

  $$\overline{\gamma'}\,(z) \equiv q\; G_{RF} \cos\left(\phi_{RF}\,(z)\right) / \left(mc^2\right)$$

  represents the average of the function $\gamma'\,(s, z)$ over the cavity length;
- $\gamma_{in}\,(z)\, mc^2$ and $\gamma_{out}\,(z)\, mc^2 = \left(\gamma_{in} + \overline{\gamma'}\,(z)\, L\right) mc^2$ are the initial and final energy of the particle considered (L is the cavity length);
- $\alpha \equiv \frac{1}{\sqrt{8}\cos(\phi_{RF}(z))} \ln\left(\frac{\gamma_{out}(z)}{\gamma_{in}(z)}\right)$.

A simple method to find the axis of a mode in a cavity is to monitor the integral power of a mode as a function of the 2D position of the beam. The spectrum analyzer provides a convenient filter, with variable bandwidth, but especially with variable frequency. Since the spectra (see Fig. 3.11) take a long time to record, due to the low repetition frequency of the beam of 1 Hz, one can monitor the signal amplitude in time domain (see Fig. 3.15). A faster method is described below and has been adopted for our first measurements.

Recalling Eqs. 2.54 and 2.55 for the $m = 1$ case:

$$\begin{cases} W_z \propto r^2 \cos\vartheta \\ W_\perp \propto r \sin\vartheta\ . \end{cases}$$

In the plane $\vartheta = 0$

$$\begin{cases} W_z = \max\left(W_z\right) \\ W_\perp = 0\ , \end{cases}$$

while in the plane $\vartheta = \frac{\pi}{2}$

$$\begin{cases} W_z = 0 \\ W_\perp = \max\left(W_\perp\right)\ . \end{cases}$$

---

[1] ω_{RF} is the RF frequency.

To excite HOM power one needs to fix $\vartheta = 0$, while, to observe a HOM deflection one has to fix $\vartheta = \frac{\pi}{2}$. Each polarization of a dipole mode has then a transverse symmetry plane. When the beam is somewhere on this plane, that particular polarization is not excited. In this case the corresponding peak in Fig. 3.11 will disappear. In exchange, when moving the beam on the perpendicular direction, the amplitude of the HOM peak will change linearly with the beam offset with respect to the mode axis. In this way one can use one polarization to monitor motion in one direction and the other polarization for the orthogonal direction. Due to deformations in the cavity, the two polarizations have randomly oriented axes.

In reality the two polarizations have an arbitrary axis, randomly oriented with respect to the horizontal plane (see Fig. 3.14). This is due to the mechanical defect in the cavities and to the position of the HOM couplers. When steering the beam position in the horizontal and vertical planes we have chosen the polarizations responding best to changes in each plane (see Fig. 3.13). Then we have made one scan say in the horizontal plane with one polarization until we found a point on the symmetry plane of the mode, followed by another scan in the vertical plane monitoring the other polarization until finding the minimum. Then by iterating alternate scans one approaches the electrical center of the mode, as illustrated in Fig. 3.14.

3.2.2 Measurements and results

The time domain signal for one scan in the horizontal plane for the second polarization of mode ♯6 (second peak in Fig. 3.11) of the first passband of cavity 1 are shown in Fig. 3.15. A filter bandwidth of 300 kHz was used. The vertical position of the beam was 0.45 mm, with respect to the un–deflected position. One bunch per beam, of about 1 nC, was used.

The HOM signal builds up rapidly after the bunch passes the cavity, at

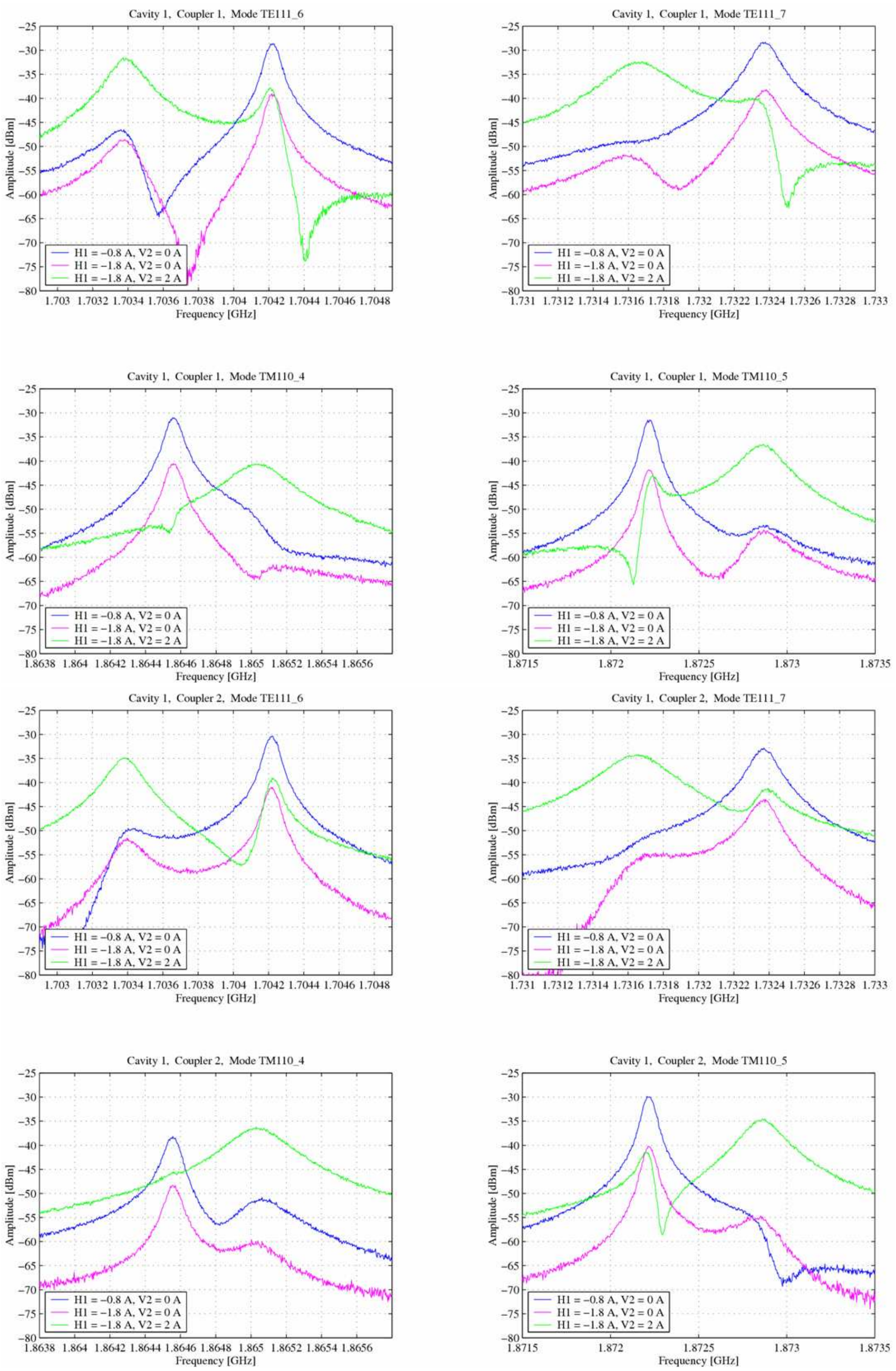

Figure 3.13: Changes of the HOM peaks during the scan, using respectively coupler 1 and coupler 2. We first steer horizontally, fixing the vertical steerer, and then we proceed in the opposite way; the modes better responding to the first or the second steering operation are respectively more horizontally or vertically polarized. They have not exactly horizontal or vertical polarization since are not exactly TE or TM modes, but only TE–like and TM–like modes.

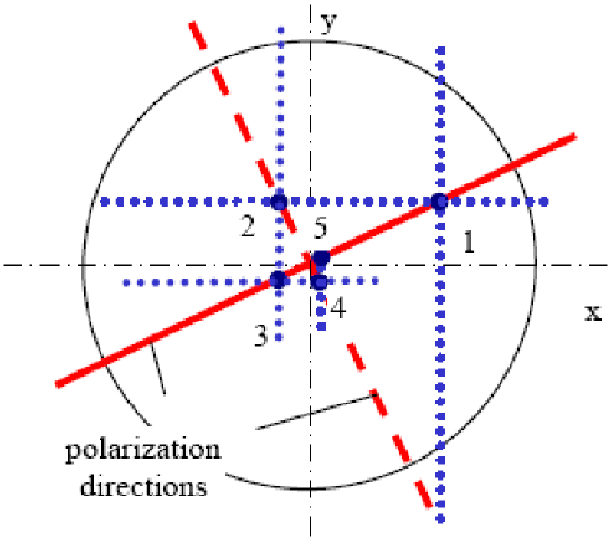

Figure 3.14: Alternate horizontal and vertical beam position scans for a mode with oblique polarization axes.

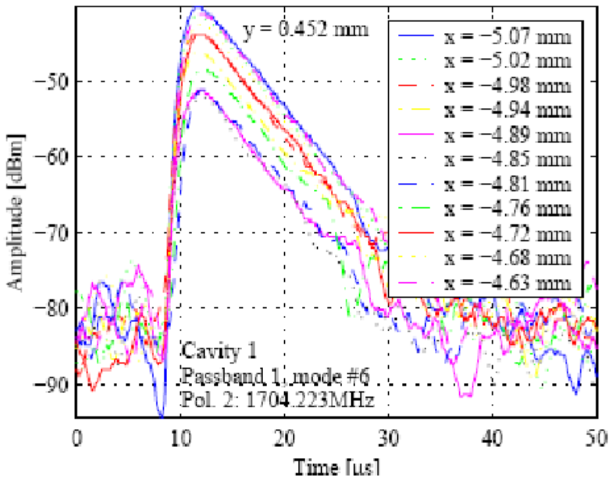

Figure 3.15: Time domain signals for the first polarization of the 6^{th} mode of the 1^{st} dipole band of the first cavity.

about t=10 μs in the plot. Then the amplitude of the signal decays with a rate given by the quality factor of the mode. The variation of the signal amplitude with the beam position can be observed. The signal is minimized when the beam is on the plane of the mode. The amplitude is not zero in this case, because of contributions from the other polarization and probably of an angle in the beam trajectory.

The amplitude of the signal in linear scale as a function of the beam position is presented in Fig. 3.17. Several scans have been made in the horizontal and vertical planes using alternatively the two polarizations. The beam position for minimum HOM amplitude is determined and its value is then used for the next scan. In the plots, the data is fitted by straight lines and the values inferred from the fits slightly deviate from the values determined during the measurements without using a fit. Note that for this mode four scans were sufficient to find the cavity axis. This was the case for all 4 modes measured in cavity 1, while for cavity 2 in general more scans were necessary.

This can be explained by the fact that, for the modes studied in cavity 1, the polarization axes are close to horizontal and vertical, in agreement with the observation that the two resonance peaks shown in Figs. 3.15 and 3.16 are well decoupled when large horizontal and vertical beam offsets are imposed. This is not the case for the modes of cavity 2, where the polarization axes are oblique and more scans are therefore needed to converge towards the mode center. We believe that this difference between the two cavities is due to mechanical defects in the cavity.

- **Cavity alignments**

It is remarkable that if the steerers between the gun and the module are switched off, the beam has a large horizontal offset of 4.85 mm in cavity 1. This seems to show that there is a large offset of this cavity with respect to the gun axis. After our study, the gun has been realigned.

- **Resolution of position measurements**

In the central regions of the scans, steps of about 50 μm in horizontal and vertical beam displacements have been used for both cavities and all modes. With a HOM amplitude signal resolution of 1 dBm in the spectrum analyzer, the effect of these steps could be clearly observed even at the minimum as illustrated in Figs. 3.15 and 3.16. Such a resolution on the beam position is also inferred from the fit accuracy and by comparing the center positions given by the minimum of the signal or by the fitting procedure.

- **Mode to mode axis difference**

However, the electric centers of the dipole modes do not coincide with such a fine resolution since they are essentially set by the relative cell to cell displacements and by their field distributions in the cavity. Fig. 3.18 compares the relative positions of the geometric centers of the 9 cell with the electric centers of the 4 dipole modes, by arbitrary superposing their two barycenters. The mode centers differ by 100 μm or less in both planes, while the cell centers vary over a 400 μm range.

3.2.3 Preliminary conclusions

Clearly more experimental data were needed at that moment.

The preliminary measurements presented in this section show that by monitoring the HOM signal amplitude for two polarizations of a dipole modes, one could measure the electrical center of the modes with a resolution of 50 μm.

Due to the cavity deformations, the main dipole modes have different electrical centers which differ by about 100 μm in most cases. This method provides a way to align the beam with respect to each accelerating cavity with a resolution much better than the 500 μm accuracy of the cavity mechanical alignment in the cryo–modules. In the case of a cryo–module, it has been possible to align the beam through the middle of the first and the last cavities, or define an axis of the module based on the information about the cavity alignment in the module, which has been obtained also from these measurements.

Summarizing our first results:

- $\Delta x_{ACC1} = 4.5$ mm,
- alignment resolution ≤ 50 μm,
- 1^{st} measurement of mode to mode axis differences.

After a shutdown, in August 2004, a new pair of steerers has been available in front of ACC1; with this new device we could scan beam offset and angle in order to minimize the HOM signal and find the axis of each cavity (which depends on the mode used).

In order to reduce the spent time, we proceeded first with parallel scans, i.e. keeping the beam angle constant in the middle of the studied cavity, and then with angular scans, keeping the beam position constant in the middle of the cavity Note in Fig. 3.19 the resolution of 50 μrad.

With such a parallel–angular scans method we found the injection conditions for which the beam travels on the axis of cavity 1 and respectively cavity 8, or alternatively, through the centers of the cavity 1 and 8.

The procedure described here, based on moving the beam, was lengthly, because only one cavity could be investigated at one time, and only for one mode at one time.

Moreover, only the amplitude of the mode was measured by the spectrum

analyzer and the phase information was missing, i.e. one could not distinguish between left and right, up and down, just from the HOM signal.
An alternative setup then has been made by the Stanford Linear Accelerator Center, and installed at TTF2.

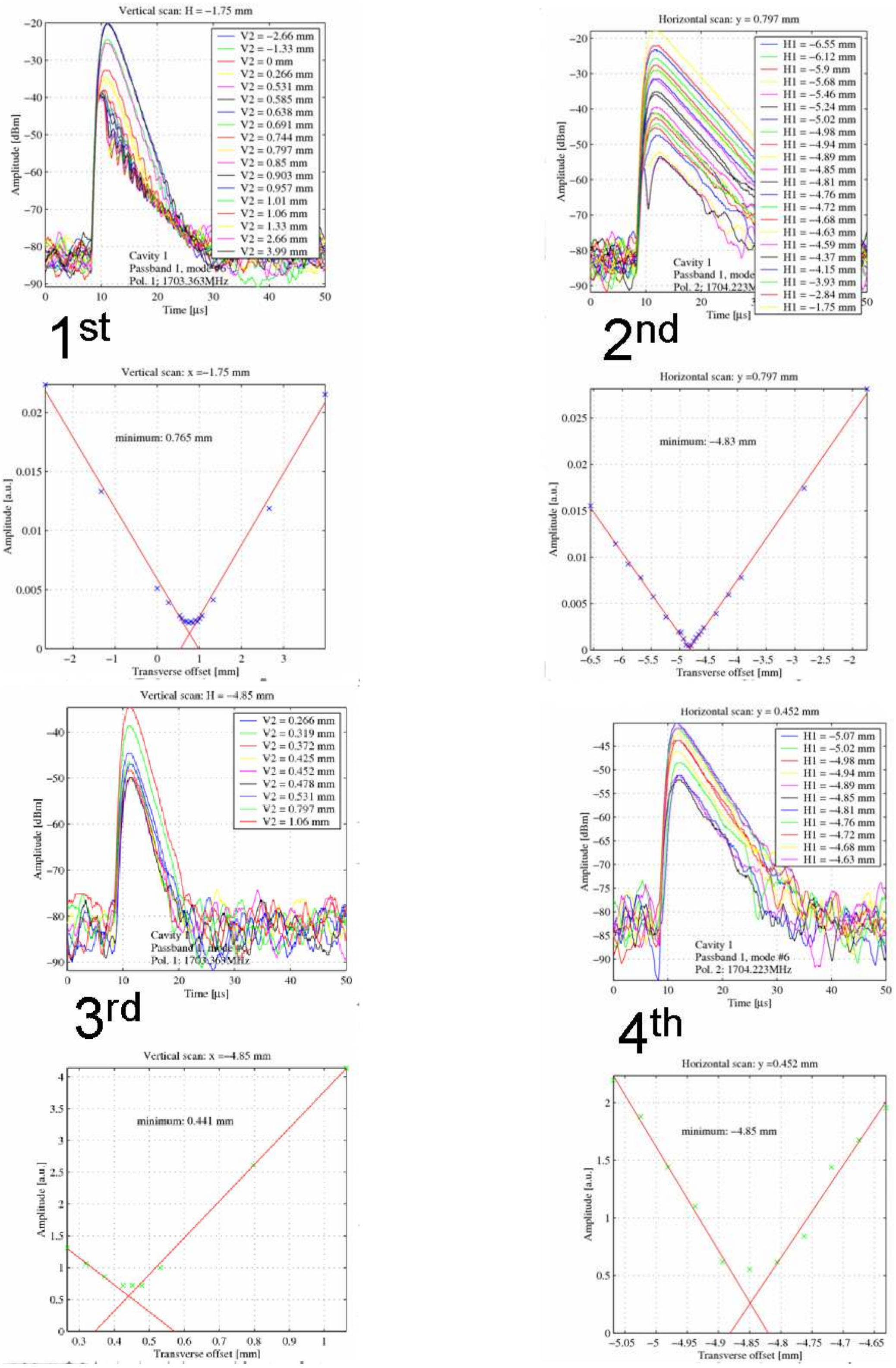

Figure 3.16: Time domain signals for cavity 1. The amplitude peaks are found steering the beam position in the horizontal and the vertical planes, and then picked and fitted to obtain the minimum HOM signal, corresponding to the electrical center of the mode.

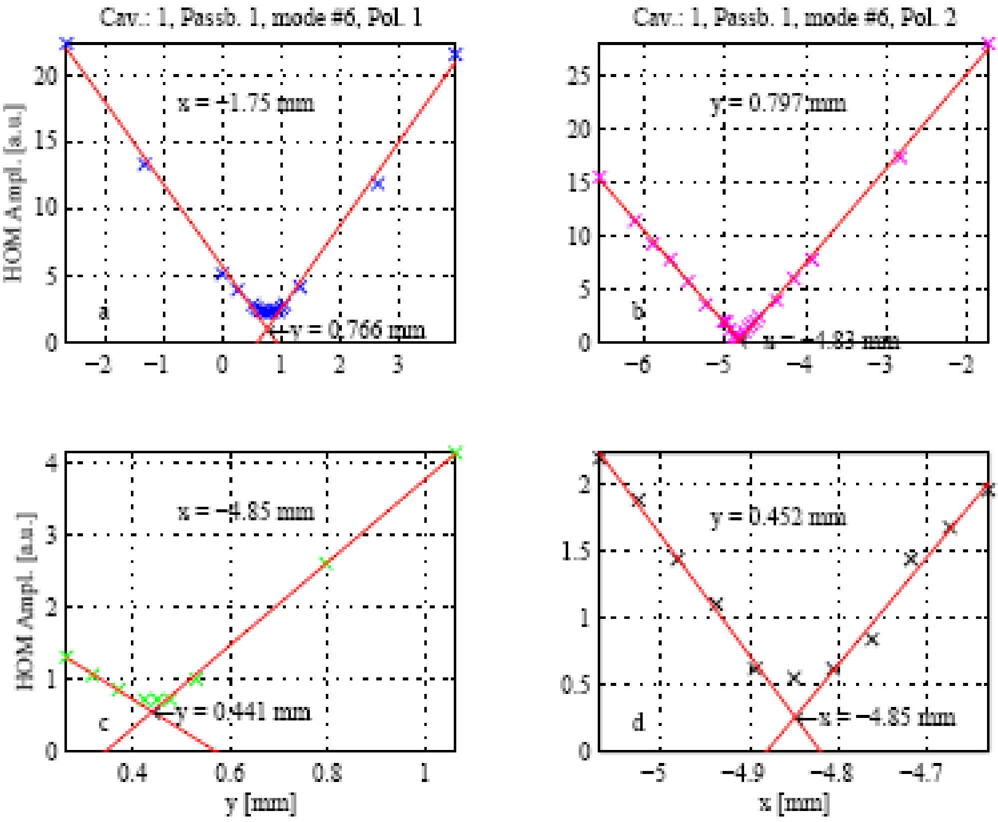

Figure 3.17: HOM signal amplitudes obtained with position scans, for each polarization of mode ♯6 of the first passband of cavity 1 as a function of the beam position.

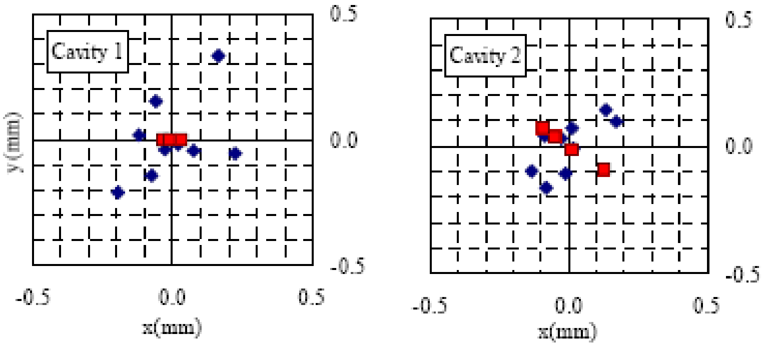

Figure 3.18: Relative positions of the 9 cell centers (blue diamonds) and of the 4 dipole mode centers (red squares).

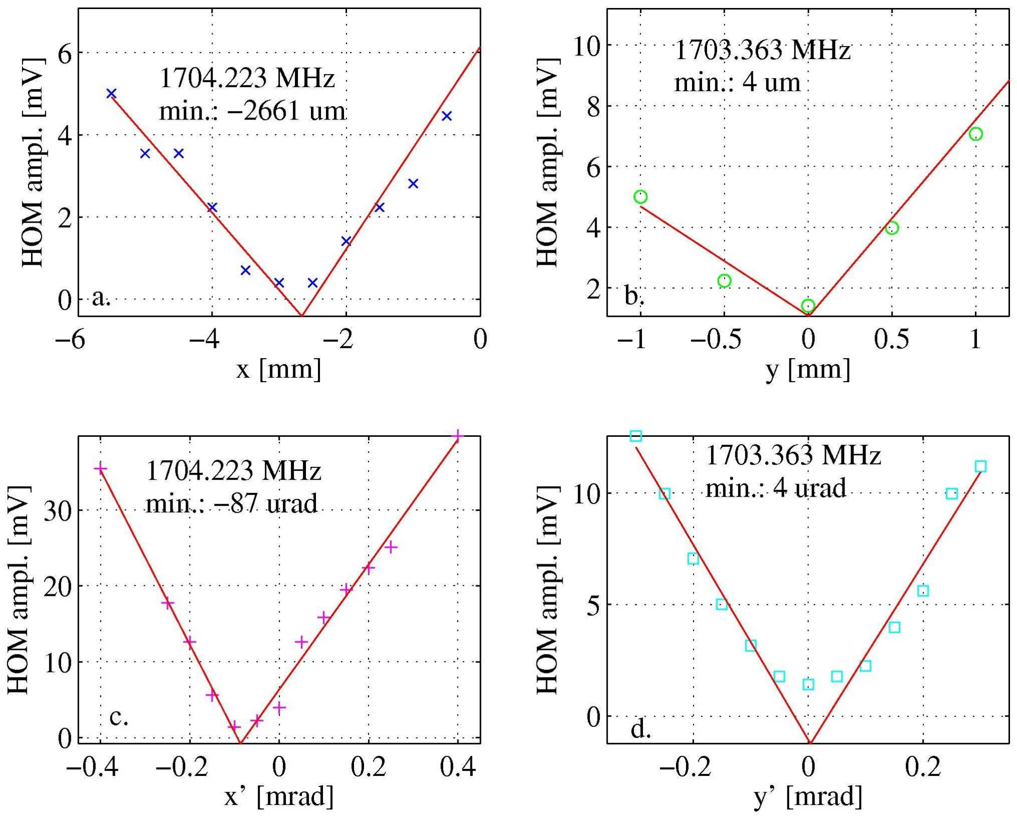

Figure 3.19: HOM signal amplitudes, obtained with angular and position scans, for each polarization of mode ♯6 of the first passband of cavity 1 as a function of the beam position.

Chapter 4

Advanced beam–based alignment studies using Higher Order Modes

In addition to the fundamental accelerating mode, superconducting cavities support a spectrum of higher frequency modes (See Chap. 2 [Wan01]). Of particular interest for use as beam diagnostics are the modes in the first two dipole bands (TE_{111} and TM_{110} respectively) and the first high order monopole passband. Previously, power measurements on these modes have been used for alignment, as shown in the previous chapter.

Here we describe the additional use of phase information to provide beam position and angle measurements. In addition, the monopole modes provide a convenient signal for charge normalization and beam phase reference. In this chapter we report the use of the amplitude and phase of the sixth and seventh TE_{111} modes. These modes couple strongly to the beam and are therefore ideal for position monitoring.

Dipole mode signals depend on beam transverse position (x, y), angle (x', y') and bunch tilt. The position signals are proportional to beam charge, position and offset. Angle signals are proportional to the product of beam charge, beam trajectory angle and the cavity length. Bunch tilt signals are proportional to the product of beam charge, bunch tilt angle and bunch length

[Ros03] (Fig. 4.1).

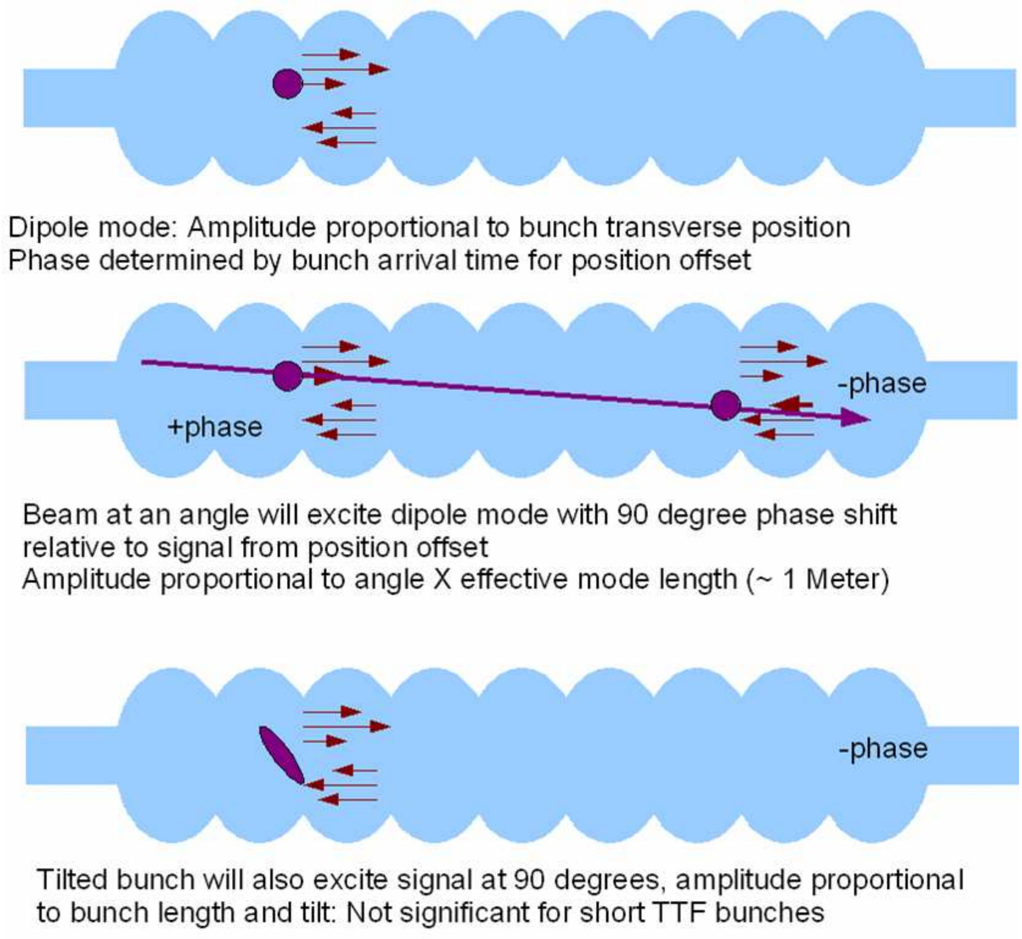

Figure 4.1: Schematic view of the RF cavity with an incoming ”tilted” beam.

4.1 Studies with broad band setup

4.1.1 Data Acquisition

While the frequency domain setup used for the above study, in Chapter 3, is easy and straightforward, it has the disadvantage of being slow and of not providing the phase information. Special electronics has meanwhile been built. A block diagram of the electronics is shown in Fig. 4.2. The signals from the HOM ports are: downmixed with the 1.3 GHz accelerator reference signal using a frequency mixer, a device performing frequency translation in such a manner that the output frequencies are lower in the spectrum than the input frequencies, $f_{out} = f_{in} - 1.3$ GHz. The range 1.3–2.8 GHz is translated to 0–1.5 GHz; subsequently the signals are digitized by a 5 Gs/s (real time)[1], 8 bit, oscilloscope, which records 50.000 points/channel. The digitizer is a system that converts an analog signal into a digital representation of the analog signal. Note: a digitizer usually samples the analog signal at a constant sampling rate and encodes each sample into a numeric representation of the amplitude value of the sample.

In order to improve the precision of the TTF2 triggers, the accelerator 9 MHz master source and the 1.3 GHz RF reference signals were added to the downmixed signal.

Four simultaneously sampled channels were measured by the scope, one for each of the 2 HOM couplers on 2 cavities. With one scope, four signals can be recorded in parallel, e.g. from the two couplers of two cavities. Two scopes have been used in some cases.

The signal from a coupler is filtered around 1736 MHz, i.e. near the frequency of the 7^{th} dipole mode in the first passband with $R/Q = 15.5\ \mathrm{M\Omega/cm^2}$(see table 3.1). A 9 MHz clock signal is used for time reference, for the synchronization of all the devices. This signal is used to select a cycle of 1.3 GHz

---

[1] Gs/s is a giga sample rate per second.

reference signal which is in turn used for phase reference.

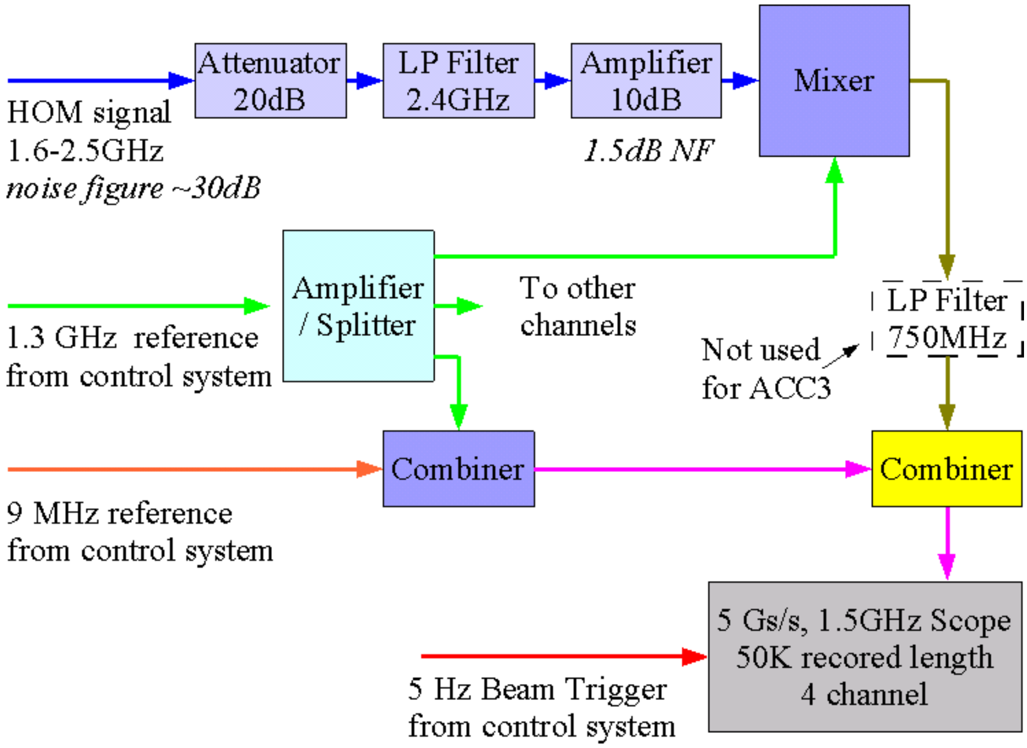

Figure 4.2: Block diagram of down mix electronics. Ten dB of cable attenuation is included in the noise figure estimate.)

The availability of the phase information gives the potential of measuring both beam offsets and angles with respect to each cavity HOM axis. Measurements have been made in the TTF2 modules with this setup. Single bunch beams have been used. The HOM signals have been measured for various offsets and angles of the beam. The beam was deflected with two pairs of magnetic correctors for each transverse plane. We will show in the next section that the resolution for beam position monitoring has been estimated to about 3 μm for a single cavity.

4.1.2 Raw signals and HOM data

The raw signal at one HOM channel, and the windowing function used for spectral analysis, are shown in Fig. 4.3. The initial saturated part of the signal is eliminated in the analysis by the windowing function.

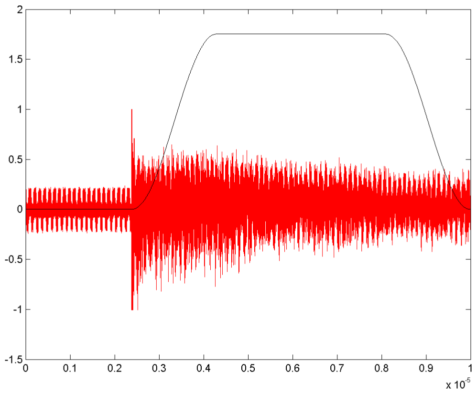

Figure 4.3: Raw signal at scope, from cavity 7, module 3, over 10 μs interval and windowing function used for the spectral analysis.)

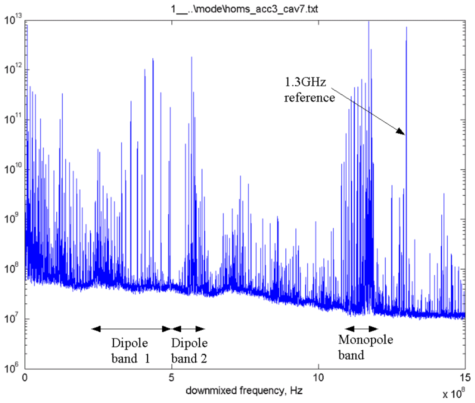

Figure 4.4: Averaged power spectrum for cavity 7, module 3, over both couplers and all data acquisition cycles. The horizontal scale of the figure is offset by LO (Local Oscillator) frequency, 1.3 GHz.

The spectrum (for cavity 7, ACC1, averaged over all data acquisitions), with the HOM bands indicated, is shown in Fig. 4.4. Dipole band 1 (TE_{111} 1.7 GHz) and dipole band 2 (TM_{110} 1.8 GHz) and the ~2.5 GHz monopole band are shown. There are a total of 18 modes in the 2 dipole bands. The first monopole higher order band can also be distinguished. Note that the mode frequencies are shifted down by 1.3 GHz as a result of the downmixing with the accelerator reference signal. The 1.3 GHz and 9 MHz are present in the spectrum, since they were mixed in the HOM signal.

In order to remove the effects of incoming beam motion, simultaneous

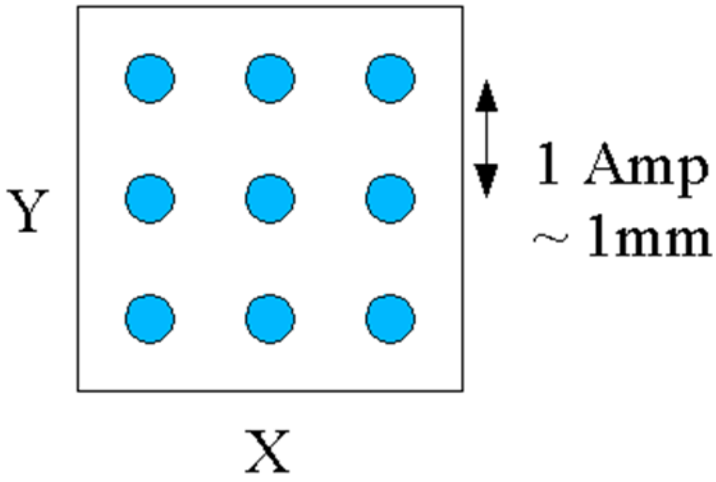

Figure 4.5: Steering X,Y correctors in (+1,0,-1) Amp box pattern.)

measurements from at least 3 cavities are required. The x and y correctors were steered over a range of +/- 1 mm (see Fig. 4.5) in all cavities for the purpose of calibrating the HOM signals. At each of the 9 corrector settings, HOM signals from 10 beam pulses were recorded.

A software to find the best match to peaks, fitting multiplets together, has been realized. The dipole modes have two orthogonal polarizations (see Figs. 4.6 and 4.7), but some modes overlap because their separation is less than a single polarization width. In such cases, the modes must be distinguished by the relative signals at the 2 couplers, yielding the complex dipole mode amplitude not only for each data set, for each mode, for each polarization, but also for each coupler:
(2 couplers)× (2 polarizations) = **4** complex signals $\mathbf{Z}_i (i = 1 : 4)$, or **8** real numbers, per mode.

The mode signal $\mathbf{Z}_i$ can be written as:

$$\mathbf{Z}_i = A\ e^{i\Phi} = I + iQ\ , \tag{4.1}$$

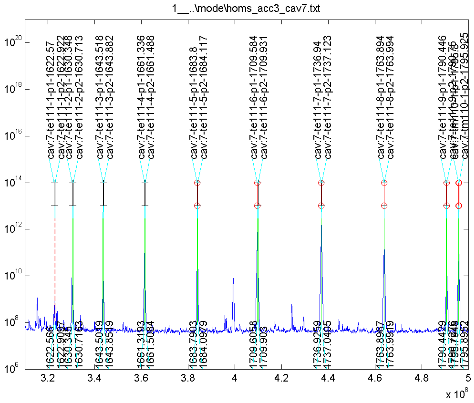

Figure 4.6: Total spectrum given by the electronics device. The green lines correspond to the frequency values previously measured with a spectrum analyzer. The new technology permits to monitor at the same time all the mode and polarization peaks with a 1.5 GHz band.

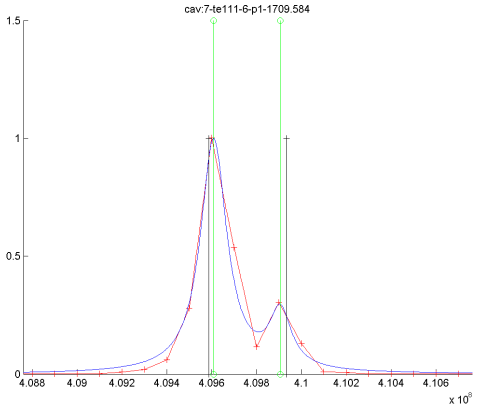

Figure 4.7: Zoom on one peak of the spectrum for the $TE_{111} - 6$ mode at 1.710 GHz.

where A is the signal amplitude and Φ the phase of the signal.

4.1.3 Data analysis

Linear regression

The calculations needed for the linear regression analysis are shown in every statistics book, and are entirely standard (see also Appendix A). We shortly summarize here:

- Given a set of measurements for a set of observables, linear regression allows to predict the measurements for one observable based on the others.
- The prediction is a linear combination of the other observables for that

measurement.

- The linear combination is chosen to minimize the error of the prediction of the observable over all measurements, in the least square sense.
- Linear regression needs more measurements than observables.

In our analysis, one can use regression to predict components of one mode from measurements of another mode. One can also use the linear regression to predict the beam position reading from the BPMs, using the mode components. In general, each dipole HOM delivers power to both couplers in each of the 2 polarization states. A calibration process (mentioned above) is required since neither the response amplitude nor the orientation of the mode polarization is known. Let $\mathbf{M}_N$ be the (109×9) real matrix of I and Q for the 109 beam pulses, as in our calibration sequence, for the 2 couplers and 2 polarizations, for a given cavity N with $1 < N < 8$. There is a $(9 \times C)$ conversion matrix $\mathbf{R}$, with C number of steerers, that we will determine through the calibration:

$$[\mathbf{M}_N \;\; \mathbf{1}] \cdot \mathbf{R} \equiv \begin{bmatrix} M_{1,1} & ... & M_{1,8} & 1 \\ M_{2,1} & ... & ... & 1 \\ ... & ... & ... & 1 \\ M_{109,1} & ... & M_{109,8} & 1 \end{bmatrix}_N \cdot \begin{bmatrix} R_1 \\ ... \\ R_9 \end{bmatrix} \sim= \mathbf{X} \; . \tag{4.2}$$

A column of 1 is necessary to take in account the offset. $\mathbf{X}$ is a $(109 \times C)$ matrix of corrector settings associated with the given pulses. The over–constrained matrix $\mathbf{R}$ is determined through least–squares linear regression[2]; in computing terms, using the transpose matrix:

$$\mathbf{R} = \left(\mathbf{M}^{\mathbf{T}}\mathbf{M}\right)^{-1} \mathbf{M}^{\mathbf{T}}\mathbf{X} \; .$$

Note that by using transport matrices one can convert each corrector settings into relative beam position (x, y) and angle (x', y') inside the considered

---

[2] see also Appendix A.

cavity N This calibration has been done for the matrix M_N associated with each cavity. Once $\mathbf{R}$ is found, we can estimate the corrector settings $\mathbf{X}_{est}$ corresponding to the HOM answer $\mathbf{M}$:

$$\begin{bmatrix} M_{1,1} & ... & M_{1,8} & 1 \\ M_{2,1} & ... & ... & 1 \\ ... & ... & ... & 1 \\ M_{109,1} & ... & M_{109,8} & 1 \end{bmatrix}_N \cdot \begin{bmatrix} R_1 \\ ... \\ R_9 \end{bmatrix} = \mathbf{X}_{est} \ . \tag{4.3}$$

At this point, we derive a second conversion matrix, $\mathbf{Q}$, (17×9) matrix, corresponding to both cavities at the end of the cryomodule. With the measured values we make a 109×17 matrix $\mathbf{E} = [\mathbf{M}_1 \ \ \mathbf{M}_8 \ \ \mathbf{1}]$, where $\mathbf{M}_1$ and $\mathbf{M}_8$ are the real matrices $\mathbf{M}$ of $\mathbf{Z}$ for the 109 beam pulses in the calibration sequence, for cavities 1 and 8, made using measured values:

$$\mathbf{E} \equiv \begin{bmatrix} M1_{1,1} & ... & M1_{1,8} & M8_{1,1} & ... & M8_{1,8} & 1 \\ M1_{2,1} & ... & M1_{2,8} & M8_{2,1} & ... & M8_{2,8} & 1 \\ ... & ... & ... & ... & ... & ... & 1 \\ M1_{109,1} & ... & M1_{109,8} & M8_{109,1} & ... & M8_{109,8} & 1 \end{bmatrix} , \tag{4.4}$$

and a 109×8 matrix $\mathbf{M}_N$, for an internal cavity (2 through 7); then we calculate $\mathbf{Q}$ from the equation

$$\mathbf{EQ} \sim= [\mathbf{M}_N \ \ \mathbf{1}] \ , \tag{4.5}$$

where $[\mathbf{M}_N \ \ \mathbf{1}]_N$ is the matrix seen in Eq. 4.2 for the same cavity N, and the symbol $\sim=$ indicates the ”equivalence” in linear regression sense. Subsequently we can use this matrix $\mathbf{Q}$ to predict the steerer settings for the given pulses but this time from the measurements of the HOM signals in the cavities at the end of the cryomodule, in order to compare the two predictions and estimate the measurement resolution; we call this new estimated matrix $\mathbf{X}_{est,1,8}$. The next step is to compare $\mathbf{X}_{est,1,8}$ as determined from the outer cavities with that determined from a given cavity in Eq. 4.3:

$$\mathbf{X}_{est,1,8} = \mathbf{EQR} \ ,$$

from Eqs. 4.2 and 4.5, and

$$\mathbf{X}_{est} = [\mathbf{M}_N \;\; \mathbf{1}]\, \mathbf{R} \ ,$$

for each machine pulse. The standard deviation of the pulse to pulse difference $\sigma = std\,(\mathbf{X}_{est,1,8} - \mathbf{X}_{est})$, by using optics matrices to translate steerer settings in beam position, gives an estimate of the position measurement resolution.

Results

The results described hereafter are based on the analysis of the TE_{111}–6 mode (∼1700 MHz). Fig. 4.8 illustrates the determination of one of the elements of $\mathbf{Q}$, which is the slope of the line formed by the strongly correlated signals $\mathbf{M}_2$[3] and $\mathbf{E}$. The estimated corrector settings can be transformed in beam position (x, y) by optics matrices. Fig. 4.9 shows the pulse to pulse difference, $\mathbf{X}_{est,1,8} - \mathbf{X}_{est}$, for this set of roughly 100 beam pulses. σ is approximately 6.4 μm for x and 4.5 μm for y. If we assume that this residual has equal contribution from both cavities, this results in an estimate of single cavity measurement resolution of about 3 μm.

These measurements were performed with a system noise figure of approximately 10 dB. The theoretical measurement noise limit, considering the known dipole mode coupling[4] of approximately 10 Ω/cm^2, and assuming a 10 dB noise figure is approximately 60 nanometers. The factor of 50 between the theoretical and measured resolution in not yet understood.

---

[3] matrix made of I and Q for cavity 2, couplers 1 and 2, polarization 1 and 2.

[4] there is a factor corresponding to the coupling of the signal out through the HOM coupler. This is harder to calculate, but e.g. Jacek Sekutowicz has made estimations of it. (The R/Q describes only the coupling of the beam to the HOM, i.e. how much power is stored in the fields; but not all are extracted to the HOM electronics.)

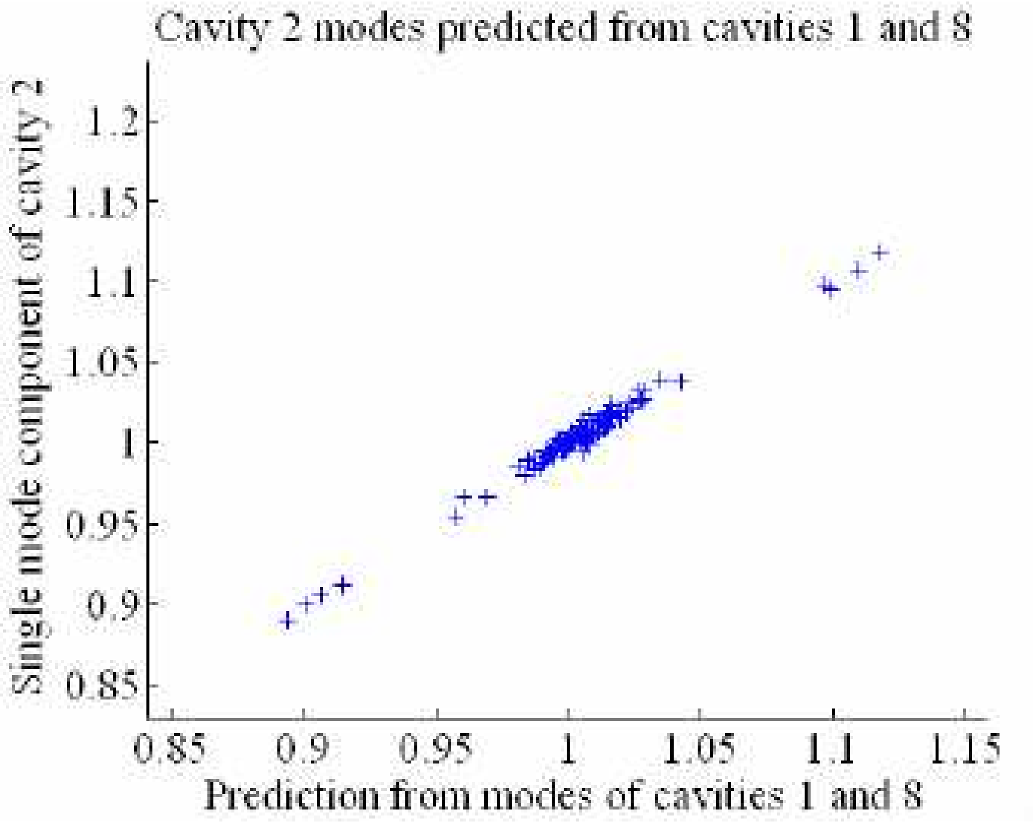

Figure 4.8: A component mode signal Z_i from cavity 2 vs those predicted through the regression fit $\mathbf{M} = \mathbf{EQ}$, from cavities 1 and 8. Both quantities are normalized by the average amplitude signals.

4.2 Studies with Narrow Band Multi–Channel Setup

Multi–Channel Acquisition System

A multi–channel system capable of simultaneously measuring all 40 of the TTF2 HOM signals has been built (Fig. 4.10).
Narrow band filters were be used to select one or two modes, around 1.7 GHz and the signals downmixed to an IF[5] of approximately 30 MHz. These signals are digitized by an array of 12 bit 100 Ms/s digitizers (much narrower

---

[5] "Intermediate Frequency" is an old term used to describe the operation of Radio Receivers, but is still used to describe Radio frequency electronics.

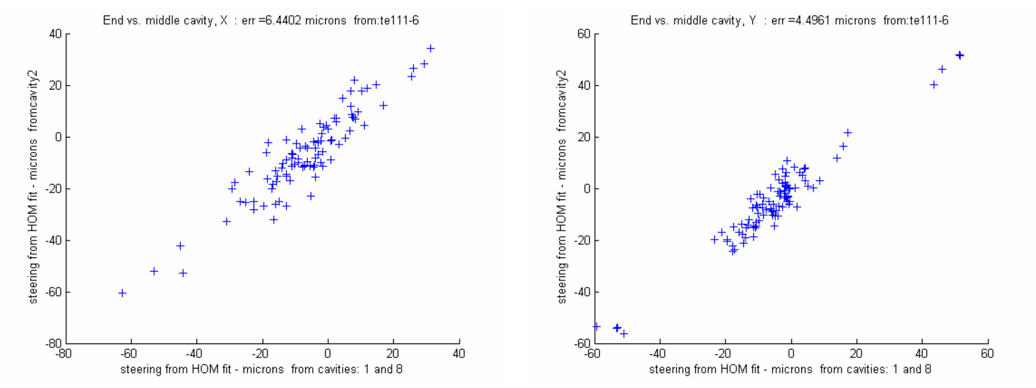

Figure 4.9: x (left) and y (right) predicted from the TE_{111}–6 mode signals of cavity 2 vs that predicted from cavities 1 and 8; $\sigma = \sim 6.4$ and $\sigma = \sim 4.5$ respectively.

bandwidth than the Gs/s digitizers used in the previous experiment), named **SIS** (**Struck Innovative Systems**).

Measurements

One such electronics channel has been built for each coupler of each of the 40 cavities at TTF2. Compared to the previous setup, one can monitor simultaneously one mode (in some cases two) from each coupler. In exchange it cannot measure the other frequencies. These signals are now part of the TTF control system.

This system has been used for beam alignment for the measurement of the position of the centers of the cavities in the cryo–module with respect to each other.

No phase or frequency information is required for the analysis described in this paragraph. For the measurements two pairs of steering correction magnets were used to generate orthogonal ”sine–like” or ”cosine–like” trajectories through cryomodules ACC2 and ACC3 (Fig. 4.11). In this way we aimed at covering a good range of the transverse space (x, x') and (y, y'). We denote the horizontal correctors with $H1$ and $H2$ and the vertical ones with $V1$ and $V2$. Fig 4.12 shows a typical signal from one of the HOM channels, from one coupler of one cavity. One can see here the beating of two frequencies close

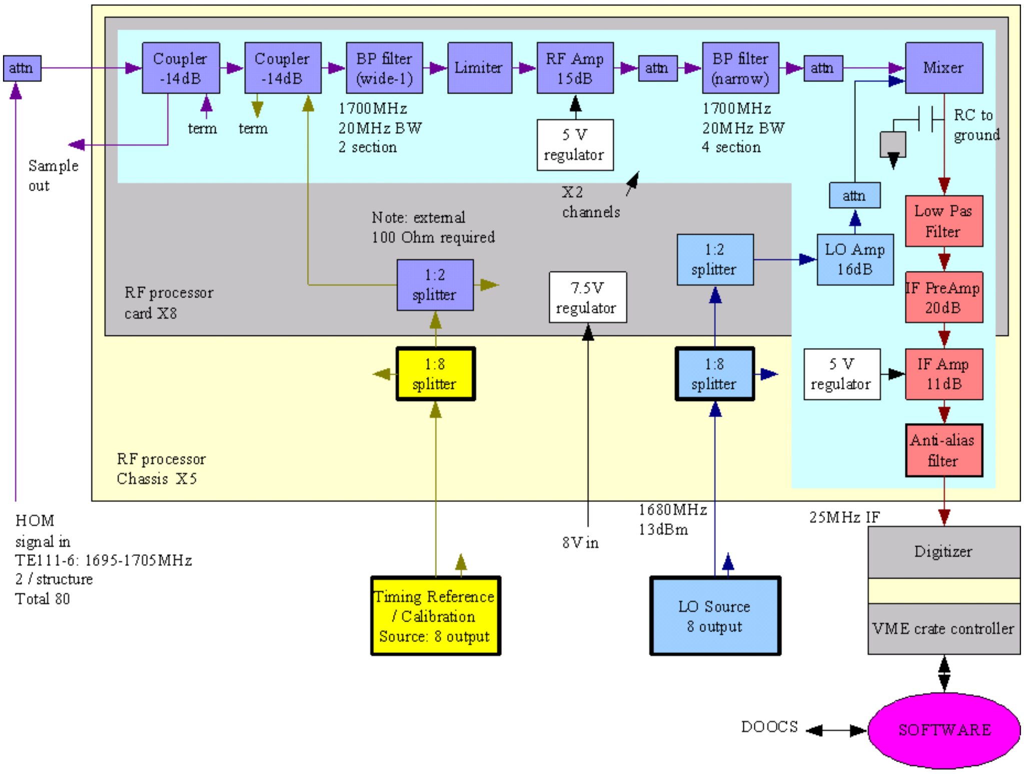

Figure 4.10: Electronics set–up of the multi–channel system measuring simultaneously all 40 of the TTF HOM signals.

to each other, decaying in time. These frequencies correspond most likely to the two polarizations of one mode. The sharp signal immediately after the arrival of the bunch is probably generated by the fundamental mode and higher frequency modes slipping through the filters. It has been removed from all the data analysis with a windowing function like in Fig. 4.3.

Fig. 4.13 shows the raw signal power for each of the 16 ACC3 HOM couplers as a function of corrector current setting. The total number of scan steps is 100, 25 per each steerer:

- from 1 to 25 horizontal steerer H1;
- from 26 to 50 vertical steerer V1;

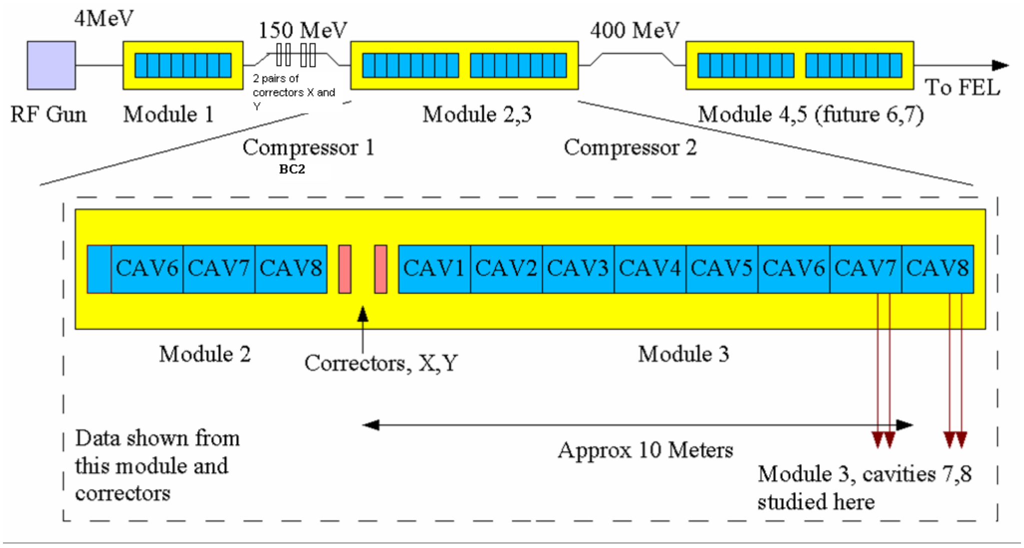

Figure 4.11: Sketch of TTF2.

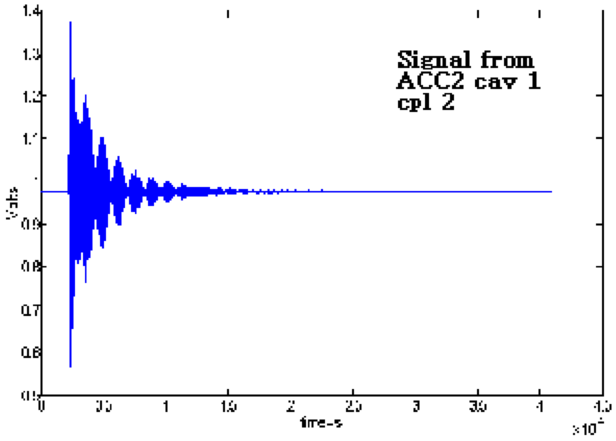

Figure 4.12: Single HOM signal.

- from 51 to 75 horizontal steerer H2;
- from 76 to 100 vertical steerer V2.

In each individual scan parabolas can be recognized, characteristic to dipole modes. For each scan most of the signals show a minimum, showing that the scans have been made around a well centered beam.

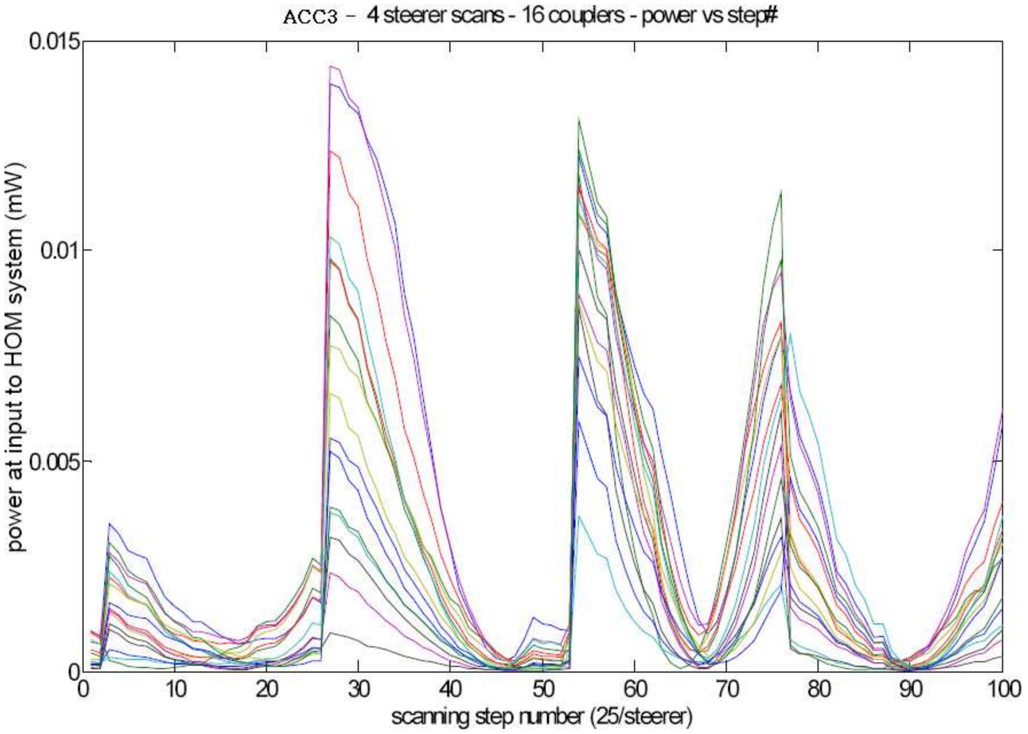

Figure 4.13: Showing the raw data from the corrector scans. The data are in the sequence H1 (steps 1–25), V1 (steps 26–50), H2 (steps 51–75), V2 (steps 76–100).

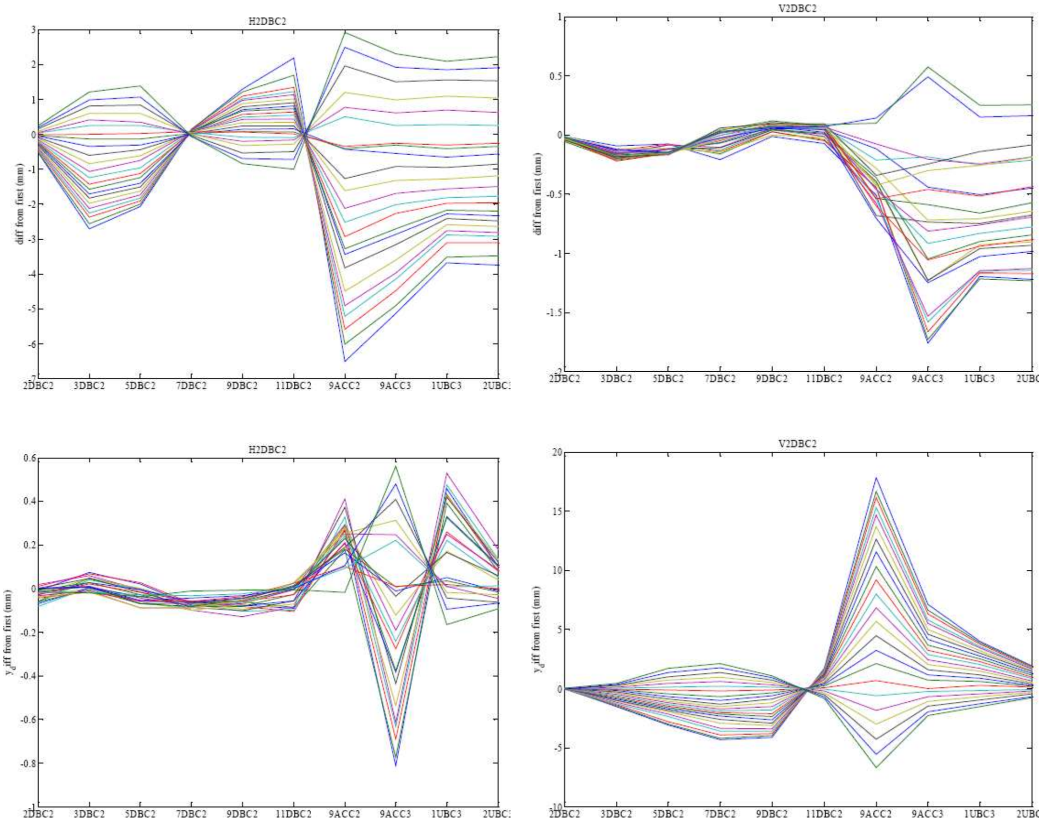

Figure 4.14: x (top) and y (bottom) difference trajectories for first and second corrector sweep.

Since the TTF correctors, at low energy ($\sim$ 100 MeV), have hysteresis the surrounding BPM's have been used to define the trajectory. There is a "cavity BPM" at the end of each cryomodule ACC2 and ACC3 and warm stripline BPM's before and after the accelerator section. Figs. 4.14 and 4.15 show the difference trajectories for each of the 4 corrector current settings as a function of BPM number. The figures have 8 parts, two for each of the correctors sweeps. It is important to note that there appears to be a lot of out–of–plane motion. Only one of the BPM's (9ACC3) is known to be rotated.

Since there were difficulties with the optics model of the facility, the attempts to "fit" the trajectories and use linear regression were unsuccessful. Therefore we used another technique, model independent analysis, which is independent of the knowledge of optics. This method can be applied to BPM's readings, or HOM signals, or corrector settings, in order to correlate these quantities with the beam motion by a Singular Value Decomposition. In the next section we will show how model independent analysis is used in diagnostics with BPM's, and then our application of the same method to HOM signals will be presented. In this way we are going to demonstrate how higher order modes can be used as beam position monitors to estimate the beam trajectory inside the cryomodules.

4.2.1 Model Independent Analysis

The idea of Model Independent Analysis (MIA) is to analyze large statistical samples without the need for a model of the accelerator.

In our case a large set M of BPM data vectors $\widehat{\mathbf{b}}_p$ for each measured pulse p is needed. The average orbit is subtracted and the individual vectors are normalized by the square root of $M \cdot P$, where M is the total number of BPM's and P the total number of pulses [Irw99]:

$$\mathbf{b}_p = \left(\widehat{\mathbf{b}}_p - < \widehat{\mathbf{b}} > \right) / \sqrt{PM} \; . \tag{4.6}$$

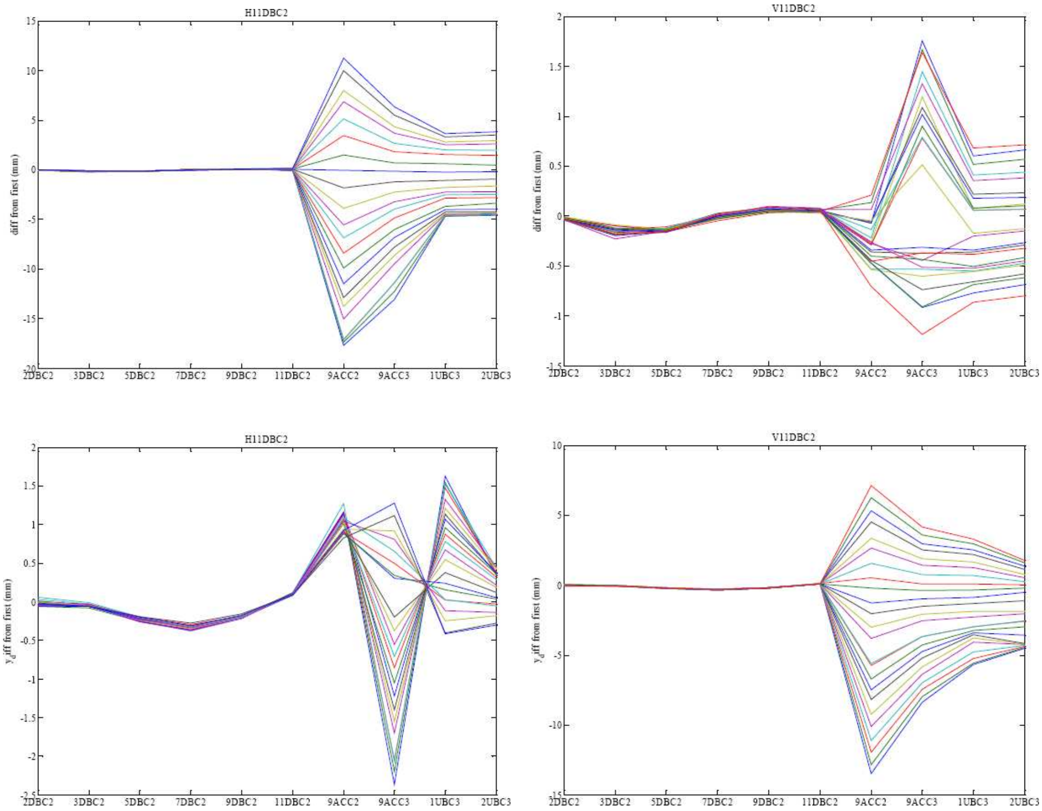

Figure 4.15: x (top) and y (bottom) difference trajectories for third and fourth corrector sweep.

These BPM normalized difference vectors are arranged row-wise in an orbit matrix **B** that contains P rows, and M columns. Typically the number of pulses is much larger than the number of BPM's.
Next the matrix **B** is decomposed into a product of the three matrices, **U**, Λ and **V**, using singular value decomposition (SVD) (Appendix B).

$$\mathbf{B} = \mathbf{U} \cdot \mathbf{\Lambda} \cdot \mathbf{V}^T \text{ with : } \begin{array}{rcl} \mathbf{U}^T\mathbf{U} & = & \mathbf{1} \\ \mathbf{V}^T\mathbf{V} & = & \mathbf{1} \end{array} \tag{4.7}$$

The left and right matrices U and V are orthogonal, whereas Λ is a P–by–M matrix containing the singular values on the diagonal and zeros off the diagonal. It turns out that the column vectors of the matrix **V** point into the direction of linear independent modes of orbit jitter. They are called spatial vectors and are orthogonal to each other. Their length is normalized to 1. Typical patterns are betatron oscillations or patterns proportional to the dispersion function, caused by energy jitter.
The column vectors of **U** describe the time development of the corresponding orbit patterns in **V** and are called temporal vectors. The singular values in $\mathbf{\Lambda}$ are given by the r.m.s. jitter amplitude averaged over space (BPM's) and time (pulses) for individual jitter modes. The vectors with the largest corresponding singular values contain the prominent jitter modes.
The SVD of a BPM matrix is shown schematically in Fig. 4.16. In the next section we will show that the model independent analysis can be easily applied also to the HOM signals to obtain an estimation of the beam trajectory inside the cryomodules, with a resolution of a few μm.

4.2.2 Data analysis

We applied MIA to the BPM readings in individual scans. We use the Matlab SVD function which separates the SVD eigenvalues and normalizes the basis vector to one. The four most significant eigenvalues are shown in the figure. It is expected that the most significant eigenvalue should be more

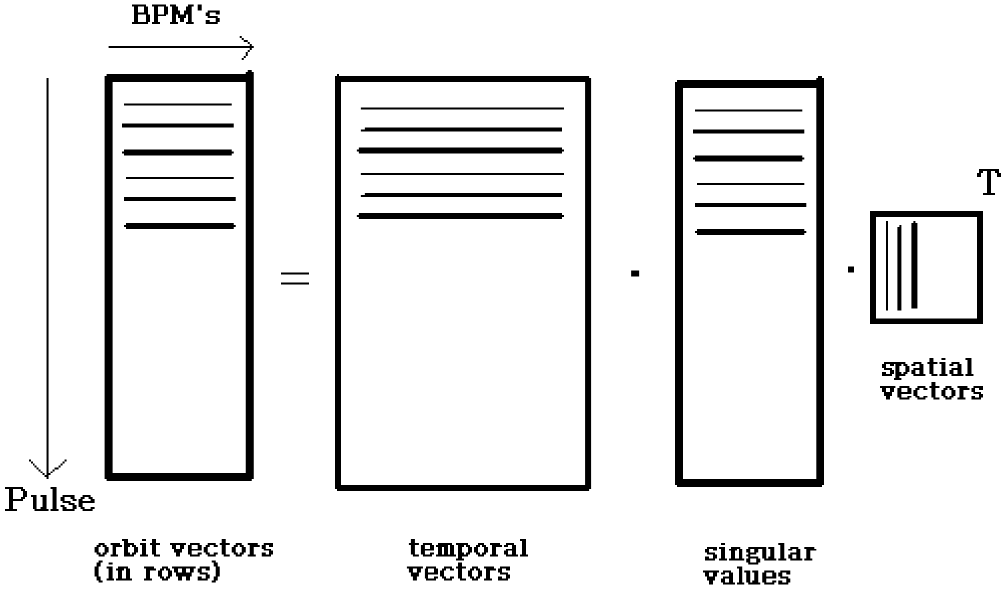

Figure 4.16: Schematic singular value decomposition of BPM matrix.

than 10 times stronger than the next one. This is not so for most of the corrector sweeps, probably because of signal saturation areas and not exactly orthogonal corrector sweeps. In order to determine the movement associated with a change in corrector strength at a given location, we multiply the basis vector amplitude at the location of the cavity by the eigenvalue and the step delta from the corrector sweep. We will use this scale for the power response analysis. The absolute position of each cryo–cavity is not of interest, only differences between them are needed to determine their locations with respect to best fit line.

Fig. 4.17 shows the first SVD spatial vector (picked from V) corresponding to the most significant mode for the first and the second corrector sweeps. The two graphics in the left side show the spatial vector due to horizontal scan versus the BPM number in the top and versus the 'time' or step number

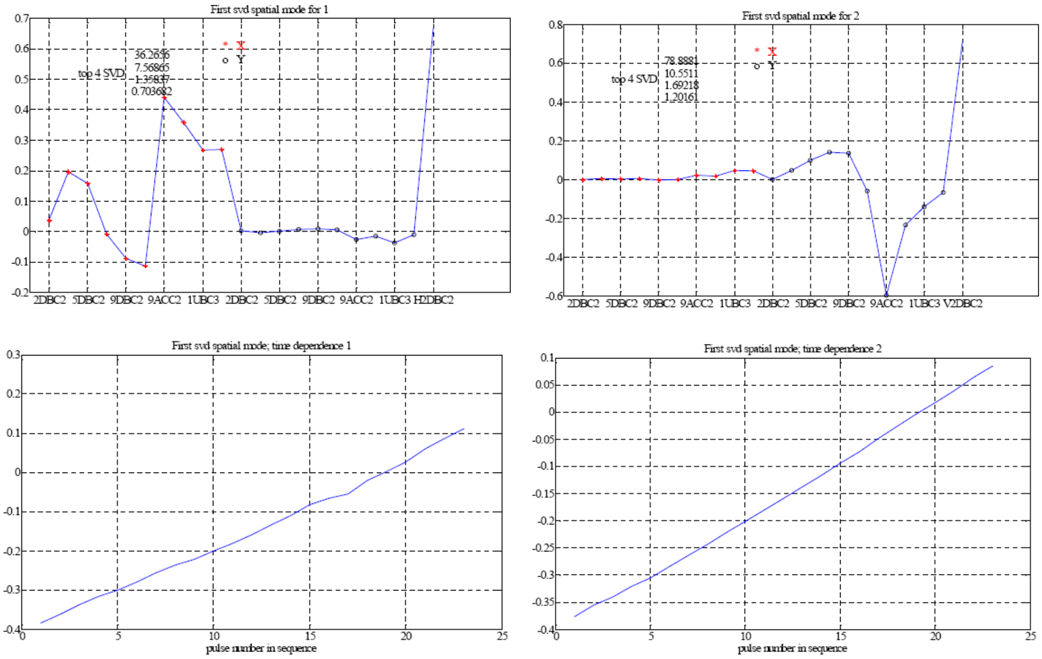

Figure 4.17: First SVD spatial vector (from V) corresponding to the most significant mode for the first and the second corrector sweeps (x left, y right);top vs BPM number (x, y followed by the corrector current); bottom: versus time (step number).

dependence of that mode in the bottom. The two graphics in the right side of the figure correspond to vertical scans.

Fig. 4.18 shows a typical sequence of HOM waveforms during the first (x) corrector sweep. Using the conversion to volts (the digitizer scale is 0.125 millivolts per east significant bit), the estimated losses in the cable and the receiver circuit gain, we are able to estimate the total energy emitted. Several of the waveforms show a sharp transient at the beginning. This transient is believed to be due to higher frequency HOM's and is not included in the data analysis. The HOM power should have a parabolic response to the corrector sweep. Fig. 4.19 shows the curve that results depicted in Fig. 4.18. Each point in Fig. 4.19 represents a single waveform, i.e. there is no pulse–to–pulse averaging. The horizontal axis is given by the SVD mode strength. For this coupler, for this sweep, the location of the minimum is at -1.2 mm and the

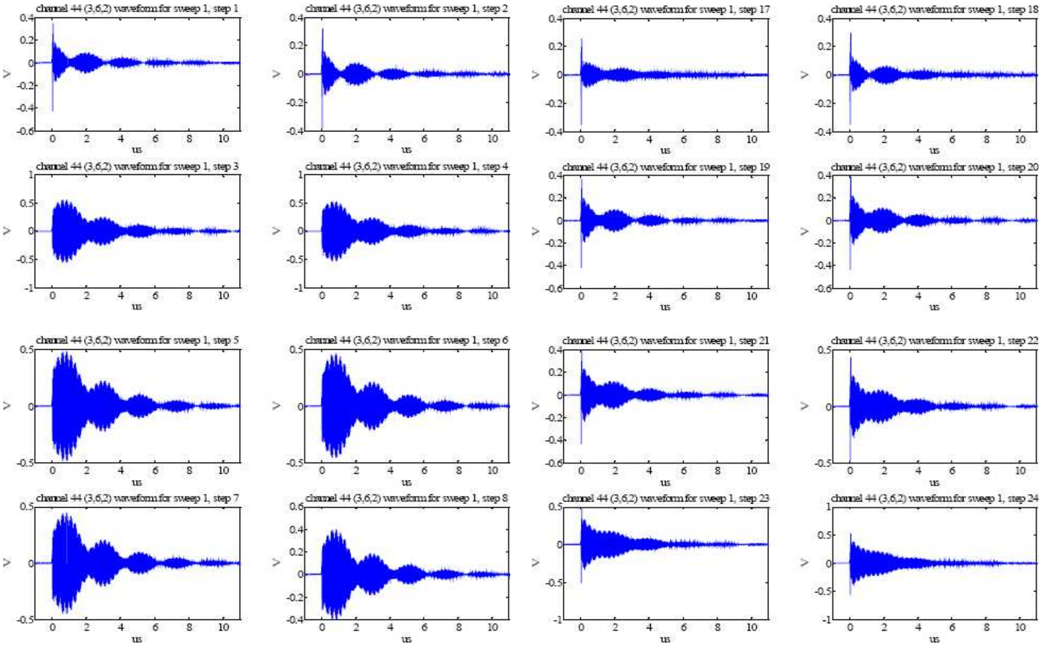

Figure 4.18: Single pulse, single bunch waveforms for the first and the second 8 steps in the x corrector sweep.

estimated power level (averaged over one decay time) is 35 μW. On either side of the minimum, the character of the mode interface changes, indicating the phase shift of one mode with respect to the other.

Fig. 4.20 shows the minimum value for each of the parabolas. Many are quite close to zero, the waveforms in these cases must be quite small. The next 4 fits, Figs. 4.21, 4.22, 4.23, 4.24, show the center locations from the fits for angle and position, for both the SVD based and the nearest neighbor. There appears to be a scale difference, and possibly a sign error for the SVD position estimation. The nearest neighbor position (4.22) shows remarkably similar answers for x, x' and y, y'. Close look at the SVD for y and y' shows that these trajectories are remarkably similar, and not orthogonal as intended. To correct this results, due to not exactly orthogonal corrector scans, source of coupling, new measurements are needed and already planned.

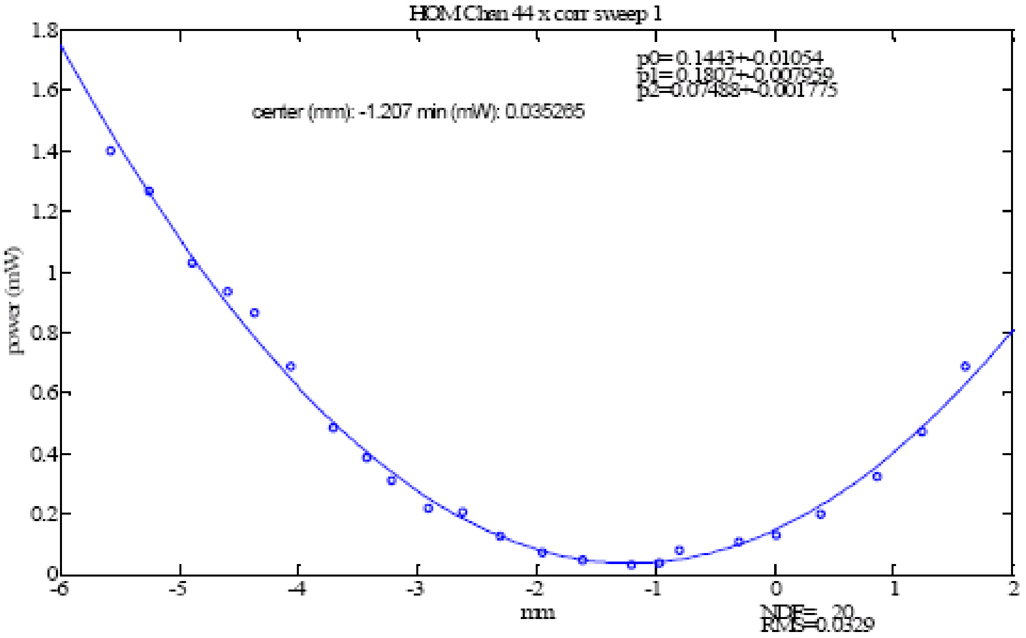

Figure 4.19: Sample (ACC3, cavity 6, coupler 2) power response from corrector sweep 1.

4.3 Analysis of a single HOM signal

In this section, we describe the detailed investigation of the HOM signal from one channel, i.e. one cavity and one coupler. The purpose is to understand the signals and develop the method to convert the HOM signals into beam position signals (HOM–BPM). The method is also applied to the determination of the transverse position of the accelerating cavities in the cryomodules. For this we use the MIA technique described in section 4.2.1.

We chose channel 26, i.e. the second coupler of the fifth cavity of the second module (ACC2), because we observed only one distinguishable frequency, making it simpler to understand and explain the signals and the procedure.

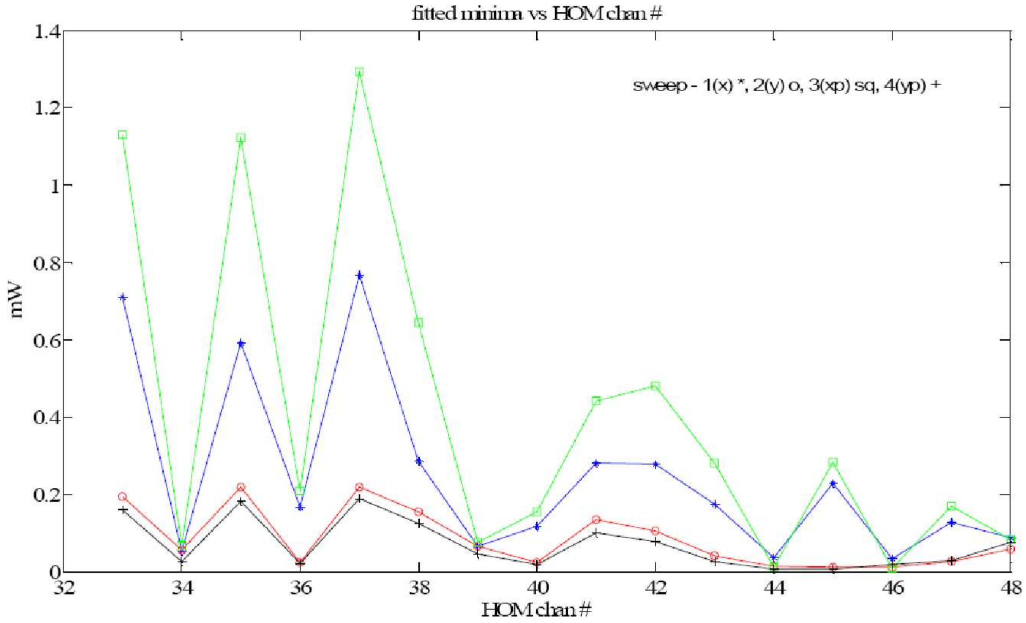

Figure 4.20: HOM dipole power minimum vs channel number (from one cavity and coupler) for the 4 corrector sweeps.

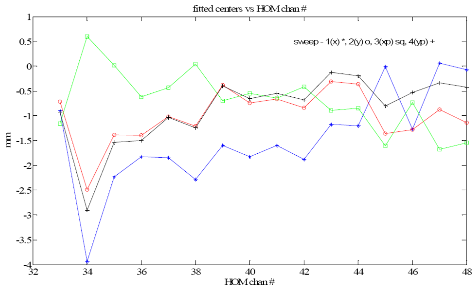

Figure 4.21: Fit minima location (mm) vs HOM channel number. The centroid and scale are derived from the SVD mode separation.

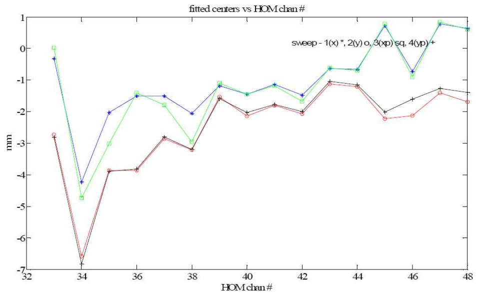

Figure 4.22: Fitted position minima from interpolations of nearest 2 BPM's.

4.3.1 Waveform processing

In order to derive beam position from the raw HOM signals, precise determinations of the amplitudes and phases of the digitized waveforms is needed. The first step in this analysis is to find the time reference; it is useful, for

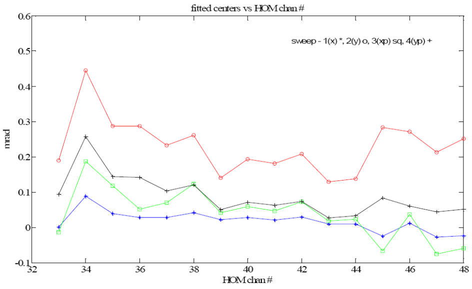

Figure 4.23: Fitted angle minimum–from nearest 2 BPMs.

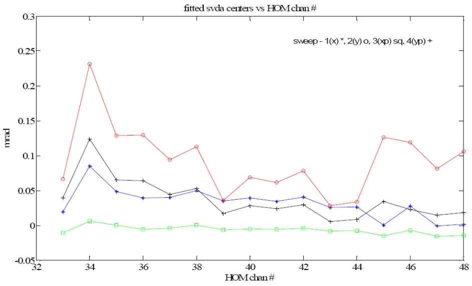

Figure 4.24: Fitted centers vs trajectory angle as determined from SVD lowest order mode.

a more precise analysis, to take the time reference exactly where the HOM waveform starts, Fig. 4.25, and then take only the most significant data for the analysis. The value for t_0 is determined by fitting the rise of the signal from the HOM and defining t_0 to be at the interception with the x axis of the the straight line fitting the two points where the rms of the rise itself is bigger than five times the standard deviation of the signal itself.

Once we determined the time reference, we can proceed with the identification of the HOM frequency ω for this channel, from a Fourier transform

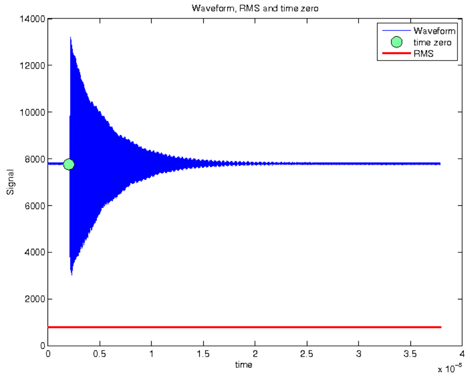

Figure 4.25: Time reference starting when the waveform starts. In this picture the time axis is in SIS (**Struck Innovative Systems** SIS3300, VME 8ch, 100Ms/s 12 bit digitizers) units.

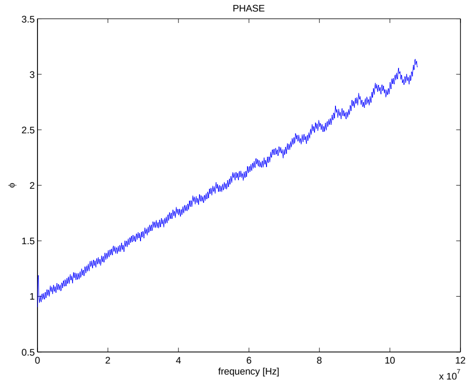

Figure 4.26: Phase before frequency correction.

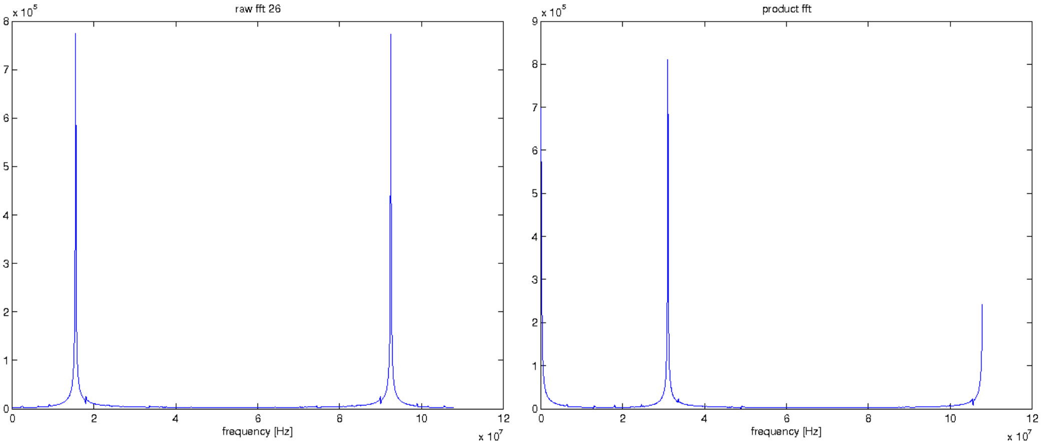

Figure 4.27: Raw Fast Fourier Transform (fft) of the original signal and of the product waveform.

(Fig. 4.27, left plot).

By multiplying the waveform with the function $\exp\left(i\omega(t-t_0)\right)$ we can distinguish a sine–like and a cosine–like component of the HOM signal. The frequency ω is determined from a fit of the amplitude spectrum, and is not very precise one. The result depends on the precision of the fit. Fig. 4.27 shows the Fast Fourier Transform of the original signal (left) and the product waveform (right).

For this reason we filtered the new waveform, with the Matlab tools, to clean the signal, and after an attentive observation of the polynomial fit of the filtered waveform and of its phase slope (4.26), we could find the exact frequency. We now then go back and multiply the original waveform with $\exp\left(i\Omega\left(t-t_0\right)\right)$, where the frequency has been corrected by a $\mathrm{d}\omega$: $\Omega = \omega + \mathrm{d}\omega$ (Figs. 4.29 and 4.28).

From the polynomial fit of the data one could also calculate the amplitude and the phase of the signal, and secondarily the quantities I and Q (real and imaginary (cosine– and sine–like) parts of the signal) for 100 pulses (Figs. 4.29, 4.30 and 4.31).

Looking at the phase (Fig. 4.32, steerers 3 and 4) we note a drastic

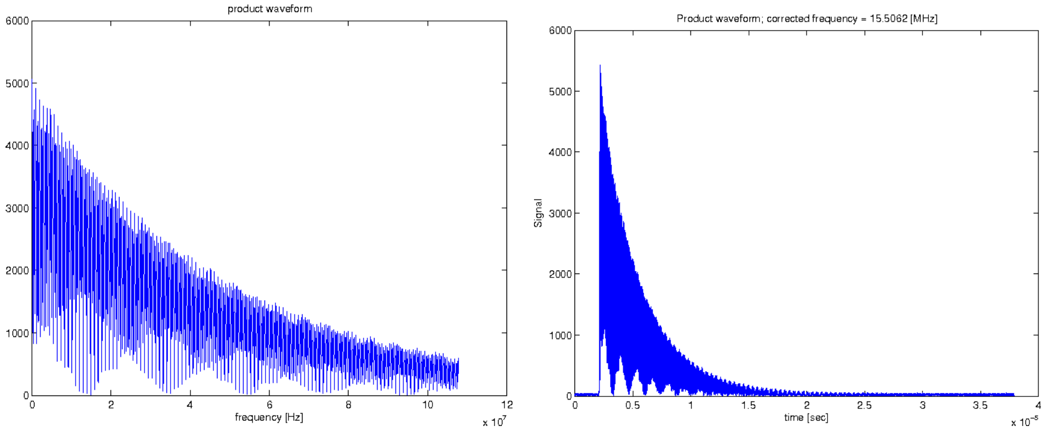

Figure 4.28: Product waveform with uncorrected and corrected frequency.

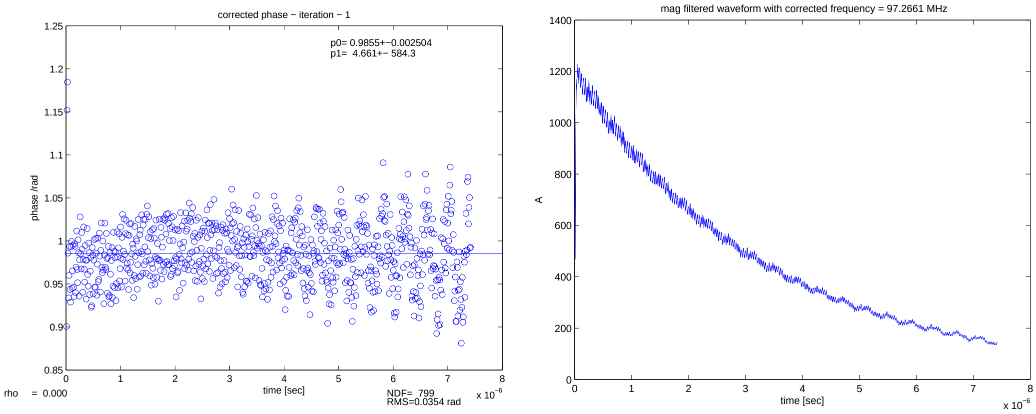

Figure 4.29: Phase at one of the 100 pulses and amplitude from the filtered product signal, with corrected frequency. The flat phase (note vertical scale) indicates that the frequency is correct.

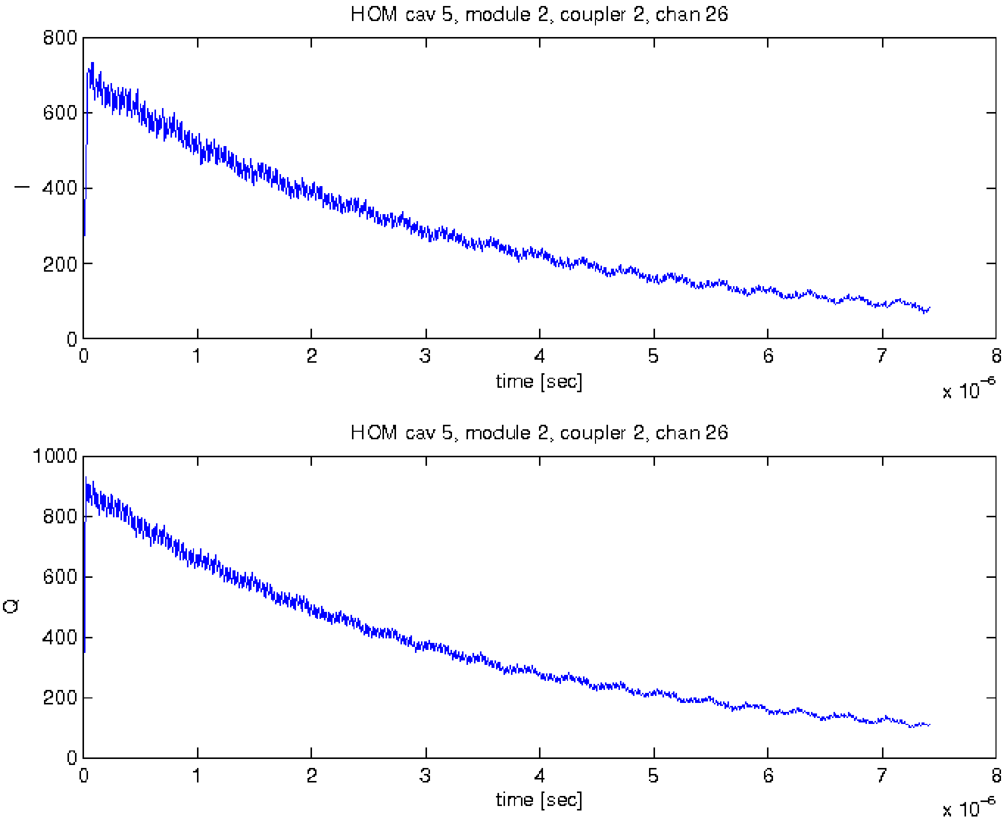

Figure 4.30: I and Q of the filtered product signal, with corrected frequency.

change in phase, and we tried to identify the corresponding BPM's readings (Fig. 4.33). One could trace a straight line between the two groups of red point, and divide the beam pipe in two area with a phase shift of $\sim \pi$.

4.3.2 BPM eigenmode and eigenfunction analysis

The readings in any one BPM are related by a linear equation to the value in the other BPMs due to linear optics:

$$x_i = a_{ij}x_j + a_{ik}x_k + ... + b_{ij}y_j + b_{ik}y_k + ... + c_i \tag{4.8}$$

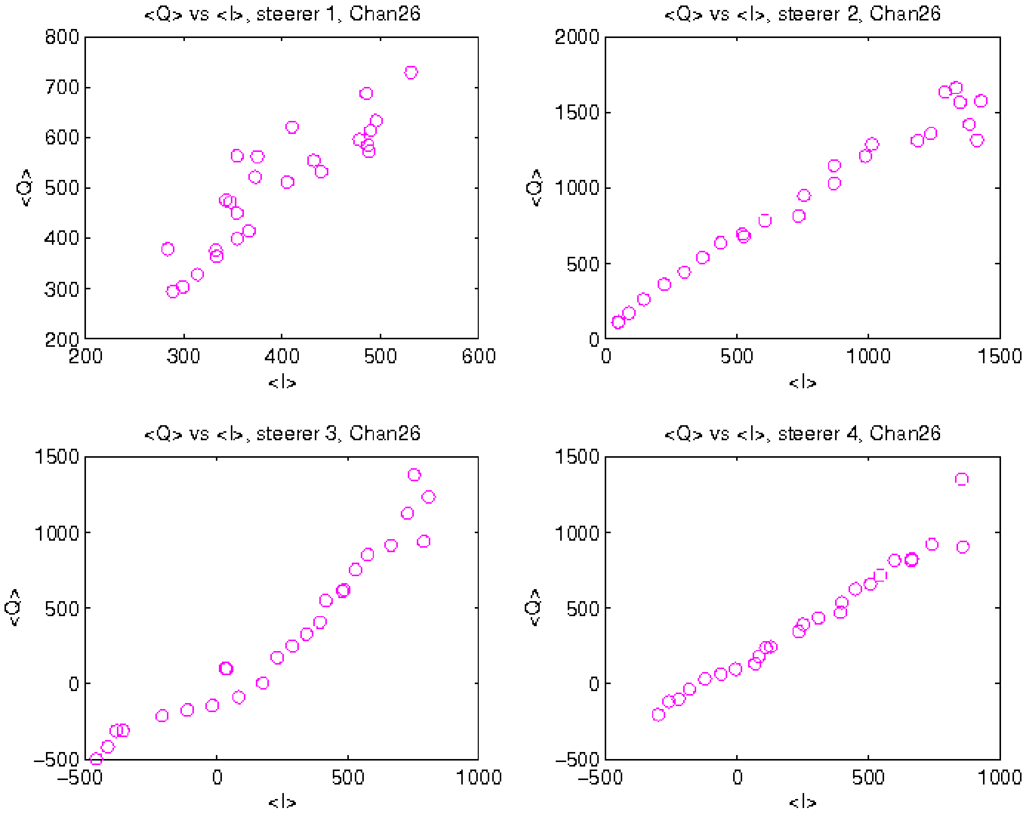

Figure 4.31: Mean Q, over all the pulses, plotted against mean I. The four pictures contain each 25 pulses corresponding to four different steerer scans. Saturation points are not removed here, giving the non–perfect linearity.

A similar equation can be written for y. The b coefficients allow for possible coupling between the two transverse planes.
We look for the values of the coefficients which would allows us to predict x and y in one BPM from the values of x and y in the other ones.
Repeated application of the above two equations yields a set of simultaneous equations which can be expressed in terms of a single matrix equation $\mathbf{X} = \mathbf{\Upsilon A}$, where $\mathbf{A}$ is a column vector made of the coefficients a, b c, $\mathbf{X}$ is a column vector of the measured values for either x or y from a given BPM, and $\mathbf{\Upsilon}$ is the matrix of x and y from the other BPMs.The matrix also contains a column of ones to allow for a constant term. Each row of $\mathbf{\Upsilon}$ and $\mathbf{X}$ corresponds to a pulse:

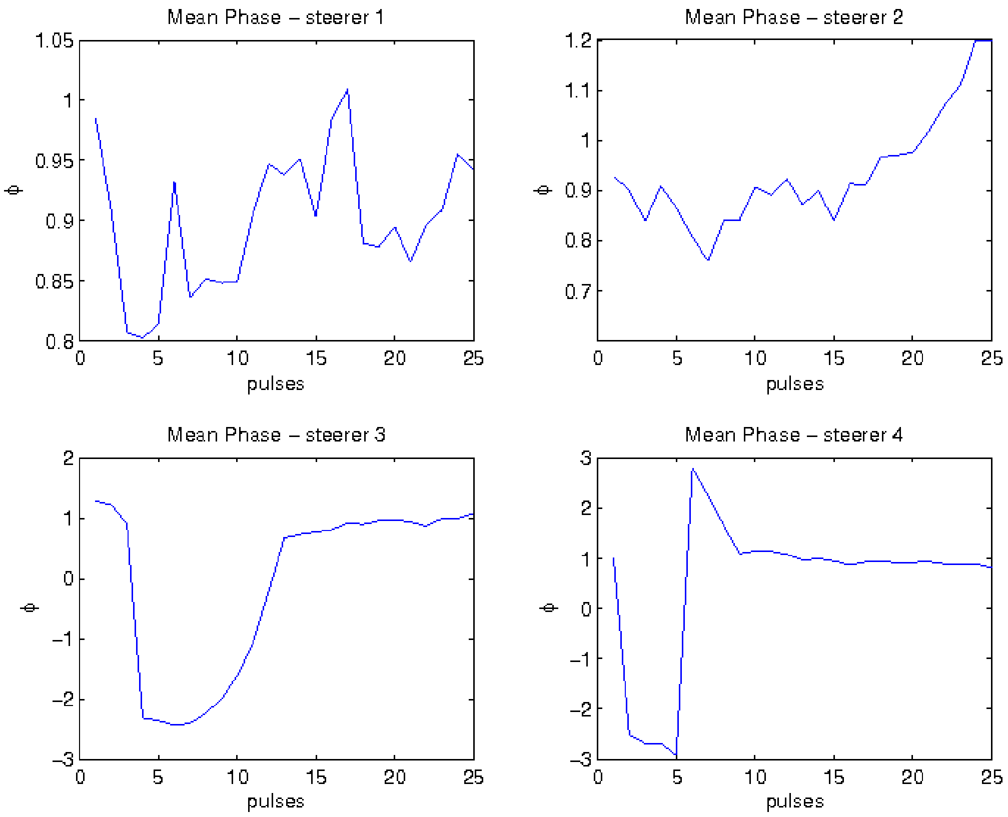

Figure 4.32: Mean phase per each corrector scan. One can clearly see a change in phase of about π in the y and y' corrector scans.

$$\begin{pmatrix} x_i \\ . \\ . \\ . \\ y_i \\ . \\ . \\ . \end{pmatrix} = \begin{pmatrix} x_j & x_k & \dots & y_j & y_k & \dots & 1 \\ . & . & \cdots & . & . & \cdots & . \\ . & . & \cdots & . & . & \cdots & . \\ . & . & \cdots & . & . & \cdots & . \\ . & . & \cdots & . & . & \cdots & . \\ . & . & \cdots & . & . & \cdots & . \\ . & . & \cdots & . & . & \cdots & . \\ . & . & \cdots & . & . & \cdots & . \end{pmatrix} \begin{pmatrix} a_{ij} \\ a_{ik} \\ . \\ b_{ij} \\ b_{ik} \\ . \\ c_i \end{pmatrix} , \qquad (4.9)$$

with $\boldsymbol{\Upsilon}$ and $\mathbf{A}$ known. In order to find matrix $\mathbf{A}$, we invert the non–square and possibly singular $m \times n$ matrix $\boldsymbol{\Upsilon}$ using singular value decomposition. We

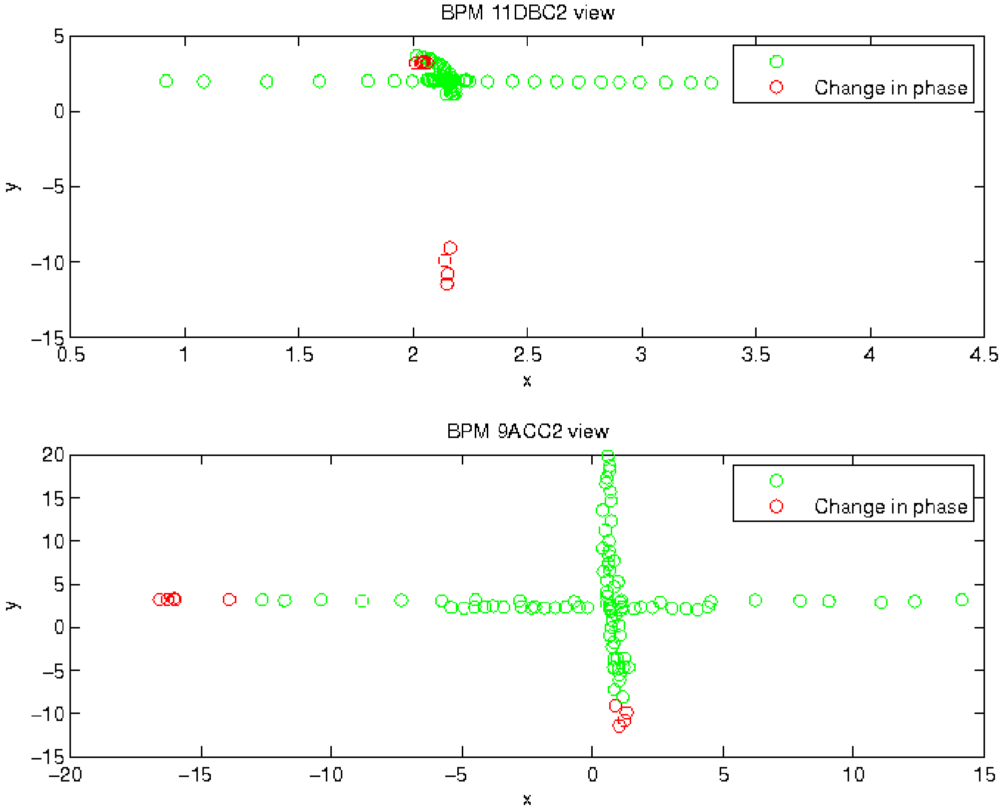

Figure 4.33: BPM readings during beam position scans. The red points correspond to the measurements with changed phase.

obtain this way the matrix $\mathbf{\Upsilon}^{+}$ such that the solution $\mathbf{A} = \mathbf{\Upsilon}^{+}\mathbf{X}$ minimizes the magnitude $|\mathbf{\Upsilon}\mathbf{A} - \mathbf{X}|$ [Jac02].

Once these coefficients are known, x and y in one BPM can be predicted from the values of x and y from the other BPMs for any pulse.

A similar analysis can be made in order to predict the BPM's readings at a certain pulse, from the readings of all the BPMs at the previous pulses. We will concentrate on this aspect of the analysis, since this will be the procedure, in the future, to predict the beam position from HOMs at a specific moment. We will use the procedure described hereafter in the analysis of the HOM signals.

Trajectory predictions

Four matrices, one for each corrector scan, have been made, with the positions read by 9 around the second accelerating module ACC2. The I and Q of the HOM signals from cavity 5, coupler 2, ACC2 (channel 26) during the scans, integrated over 4094 points of each HOM waveform and normalized to 10^5, are shown in Fig. 4.34. The normalization is needed for the SVD analysis. The number of measured pulses for each steerer is 25, but we eliminated the points where the HOM signals were saturated and where the I and Q did not show a linear behavior. The order of the scan in this figure is horizontal, vertical, horizontal, vertical.

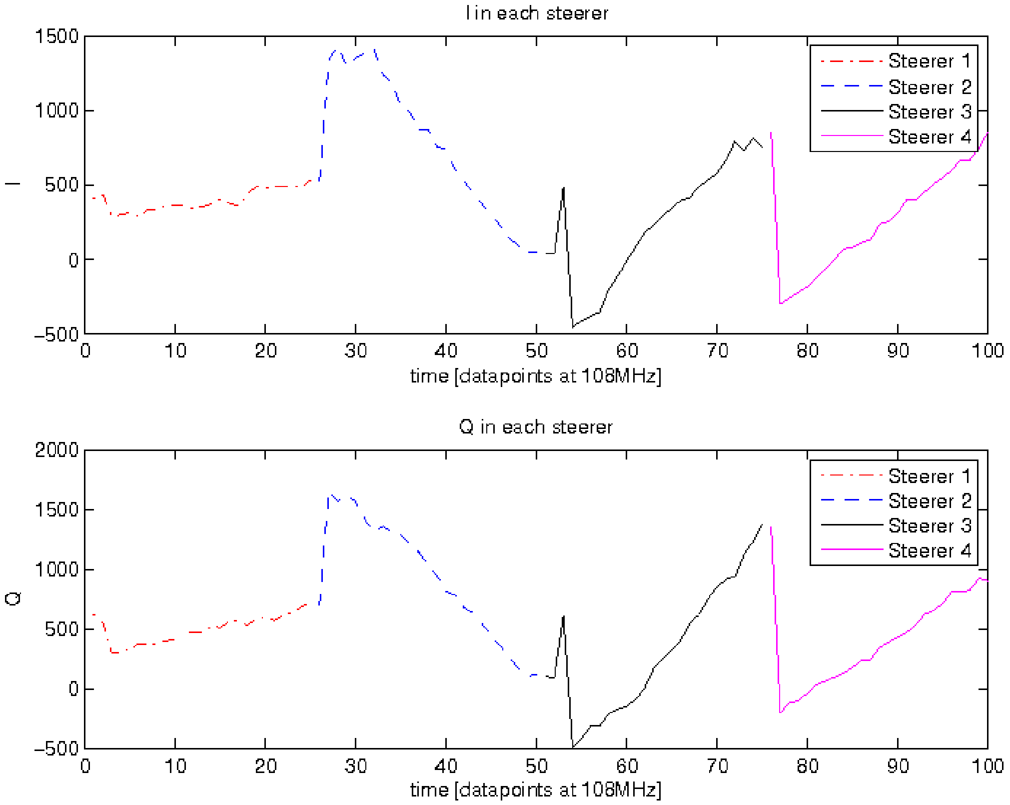

Figure 4.34: I and Q plotted against the pulse number. Steerers 1 and 3 are horizontal, while 2 and 4 are vertical.

The SVD of these four BPM matrices gives back four sets of new matrices, $[\mathbf{U_n}, \mathbf{S}_n, \mathbf{V}_n]$, with $n = 1, 4$.
As explained above, both $\mathbf{U}$ and $\mathbf{V}$ are unitary matrices representing orthogonal temporal patterns and spatial patterns respectively, while $\mathbf{S}$ is a diagonal matrix containing the corresponding eigenvalues. The number of eigenvalues above the noise floor determines the number of significant physical variables that are changing and affecting the beam centroid motion. In Fig. 4.35 the plots of each of the $\mathbf{U}$ and $\mathbf{V}$ matrices, for the highest eigenvalue, for each corrector scan, are shown. The abscissa for $\mathbf{V}$ contains 9 x readings from the BPM's followed by the y readings. Like in the previous figure, the four correctors are used, respectively, for horizontal, vertical position steering and horizontal, vertical angular steering. One can note in Fig. 4.35[6] that when we steer horizontally, in position or angle, the answer is in the first set of nine points of the abscissa, corresponding to the x positions read from the nine BPMs considered, while, if a vertical steering is applied, the answer is in the second set of nine points of the abscissa, corresponding to the y readings.

In order to check the accuracy of the method we use linear regression. We calculated the four vectors $\mathbf{a}_{1,2,3,4}$, one for each steerer, which validate the condition:

$$\mathbf{\Xi}\cdot\mathbf{a}_n = \begin{pmatrix} I_{25} & Q_{25} & I_{26} & Q_{26} \\ . & . & . & . \\ . & . & . & . \\ . & . & . & . \end{pmatrix}_n \cdot \begin{pmatrix} a(1) \\ a(2) \\ a(3) \\ a(4) \end{pmatrix}_n = \begin{pmatrix} u(1) \\ . \\ . \\ u(m) \end{pmatrix}_n = \mathbf{u}_n \ , \quad (4.10)$$

with n= steerer 1,4; the matrix to the right hand, Ξ_n, is a $m \times 4$ matrix of I and Q for the fifth cavity of the second module, coupler 1 (channel 25) and 2 (channel 26), at all the m pulses of non–saturation for the steerer "n" and $\mathbf{u}_n$ is the first column of the matrix $\mathbf{U}$ calculated with SVD for the steerer "n". Then the four vectors $\mathbf{a}_{1,2,3,4}$ are calculated by linear regression, using

---

[6] in this figure the scan order is: horizontal, horizontal, vertical, vertical.

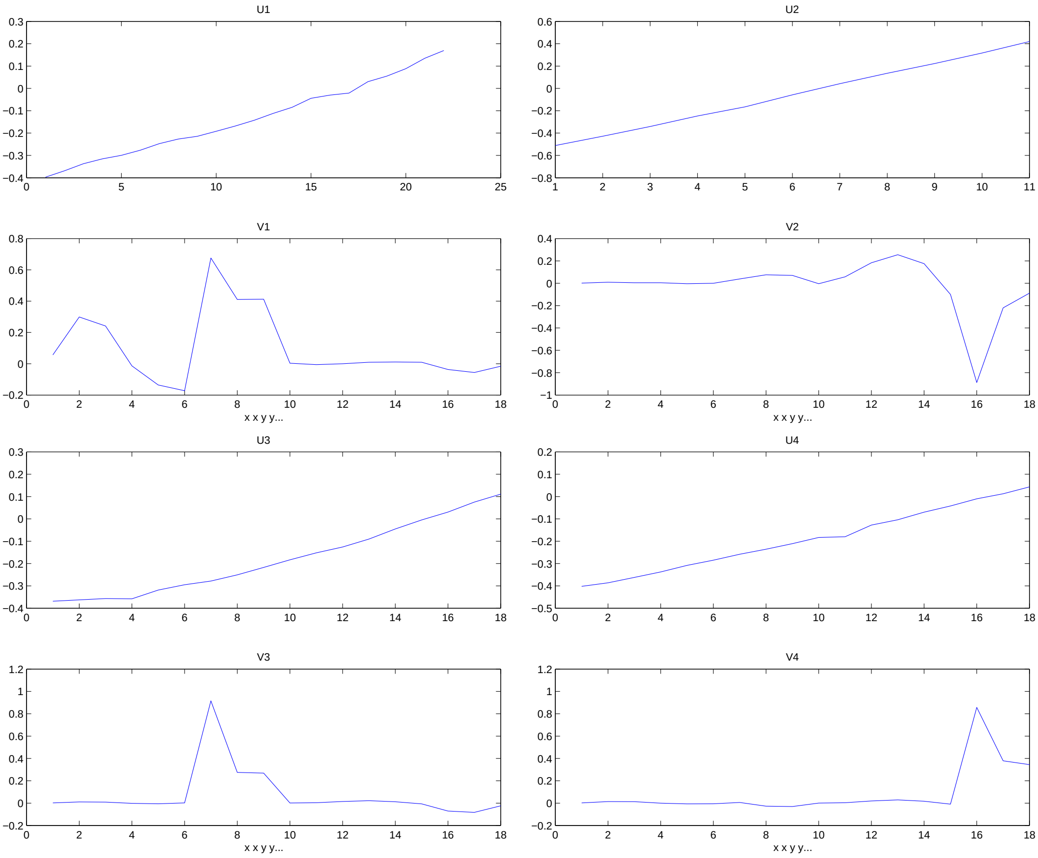

Figure 4.35: Temporal and spatial eigenvectors, for the highest eigenvalue, from BPM's readings. Points 1:9 corresponding to steerer sweeps 1 and 3 (horizontal), while points 10:18 to steerer sweeps 2 and 4 (vertical).

Matlab tools: $\mathbf{a}_n = \Xi^T \cdot \mathbf{u_n} = \Xi \setminus \mathbf{u_n}$, where the symbol $\setminus$ means linear regression, in Matlab language.
Now we multiply this calculated vectors **a** by the same matrices Ξ, to have back four "predicted" temporal eigenvectors to compare with the original ones, obtained previously from the SVD analysis.
The accuracy of the SVD is in this case revealed by the residual between the temporal eigenvectors **U** obtained from SVD and the ones predicted with linear regression with the HOM signals, by using the same set of measurements (i.g. same matrix Ξ).
We choose for this test only the first column of each matrix $\mathbf{U}^7$, corresponding to the highest eigenvalue, the only one above the noise floor (order of at least 10 times bigger then the other eigenvalues). Fig. 4.36 shows in comparison the two sets of **U** (calculated with SVD and predicted with linear regression) for each steerer scan, corresponding to the highest eigenvalue, the only above the noise floor. By "known **U**" we mean in this figure **U** from the direct SVD of the BPM readings, while "predicted **U**" is the same temporal eigenvector matrix, estimated by using linear regression. The SVD analysis results are confirmed by the linear regression against the HOM readings. We also calculated the corresponding predicted trajectories from both the sets of vectors **u**, multiplying them by the corresponding eigenvalues (Figs. 4.37 and 4.38):

$$\mathbf{x}_{n,traj} = \mathbf{u}_n \cdot s_n \cdot \mathbf{v}_n \ , \tag{4.11}$$

where $\mathbf{u}_n$ and $\mathbf{v}_n$ are the temporal and spatial eigenfunctions corresponding to the highest eigenvalue s_n, and $n = 1, 4$ the corrector sweep number. Note the different scales in the plots.

The vectors **a** have been used in a second time, as columns for a 4×4 matrix, **A**, to calculate a predicted set of temporal eigenvectors corresponding to a new measurement of I and Q values for channels 25 and 26, for each corrector (109 new pulses):

---

[7] calculated from SVD.

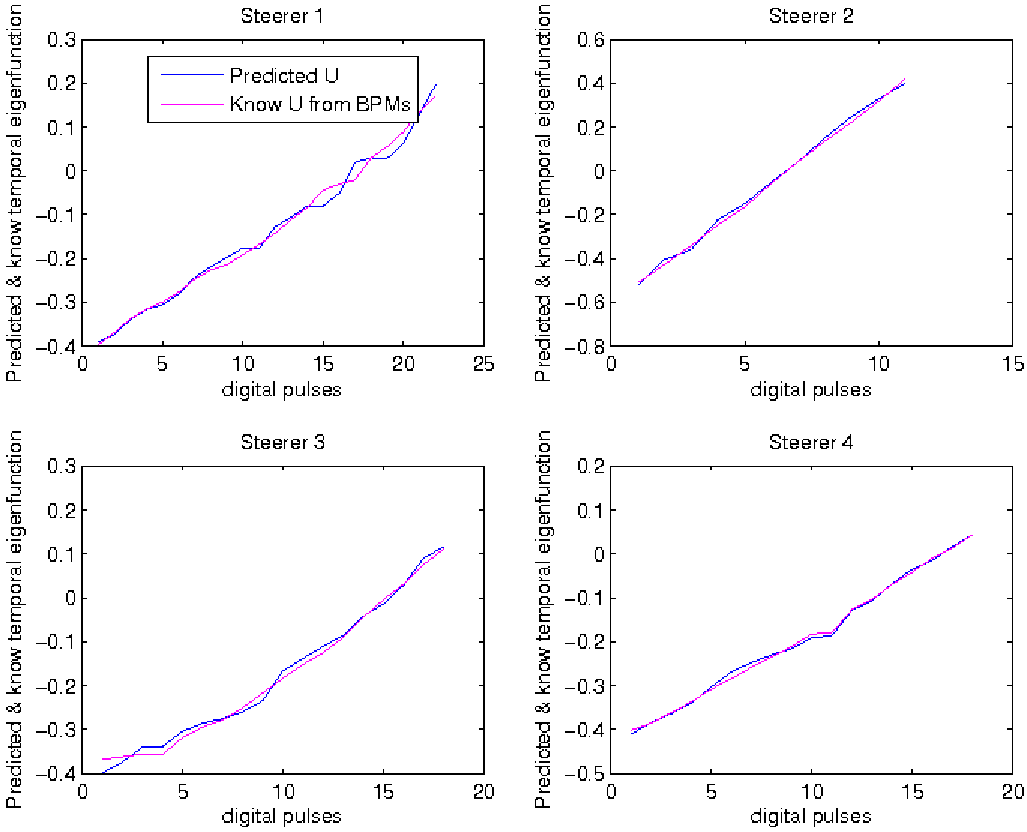

Figure 4.36: Comparison between the predicted temporal eigenvectors and the vectors obtained by SVD analysis. By "known **U**" we mean **U** from the direct SVD of the BPM's readings, while the "predicted **U**"traces are estimated by using linear regression.

$$\begin{pmatrix} I_{chan25} & Q_{chan25} & I_{chan26} & Q_{chan26} \\ . & . & . & . \\ . & . & . & . \\ . & . & . & . \end{pmatrix}_n \cdot \mathbf{A} = \begin{pmatrix} u(1) \\ . \\ . \\ u(m) \end{pmatrix}_{n,pred} = \mathbf{U}_{n,pred} \cdot \qquad (4.12)$$

One could now introduce these four vectors as columns of a matrix $\mathbf{U}_{pred}$, in order to predict the beam positions and trajectories corresponding to a known set of I and Q values, e.g., as seen before:

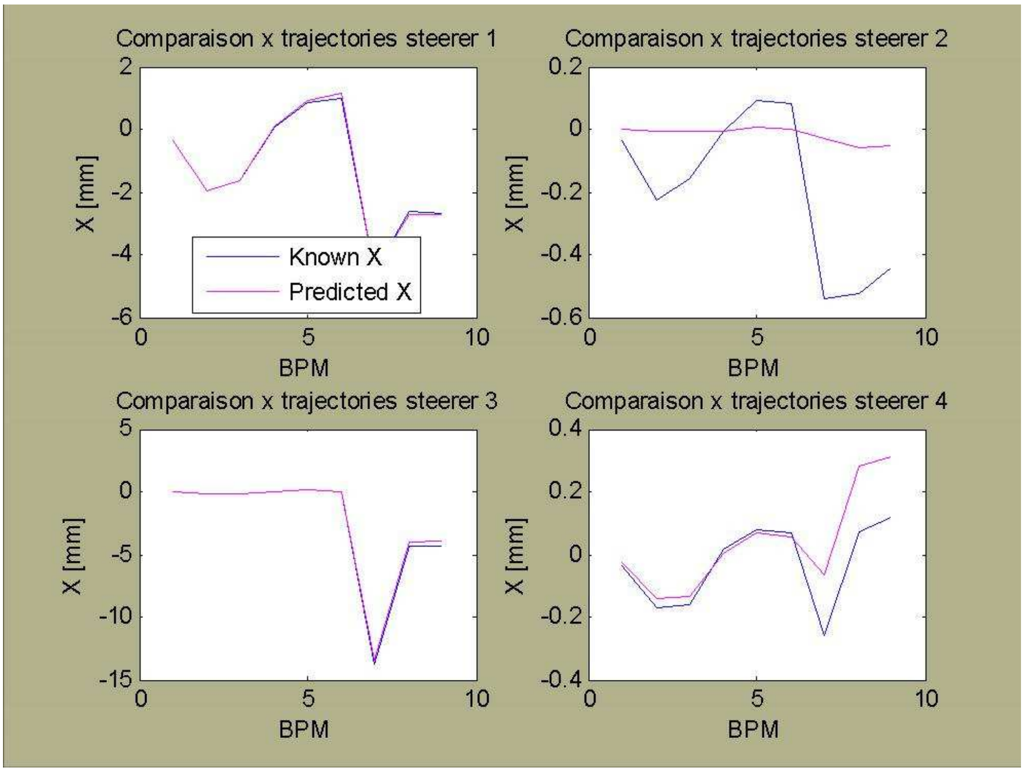

Figure 4.37: Comparison between the horizontal trajectories from the predicted temporal eigenvectors and the vectors obtained by SVD analysis. Same notation for "known" and "predicted" than in Fig. 4.36. Note the different scales in the plots.

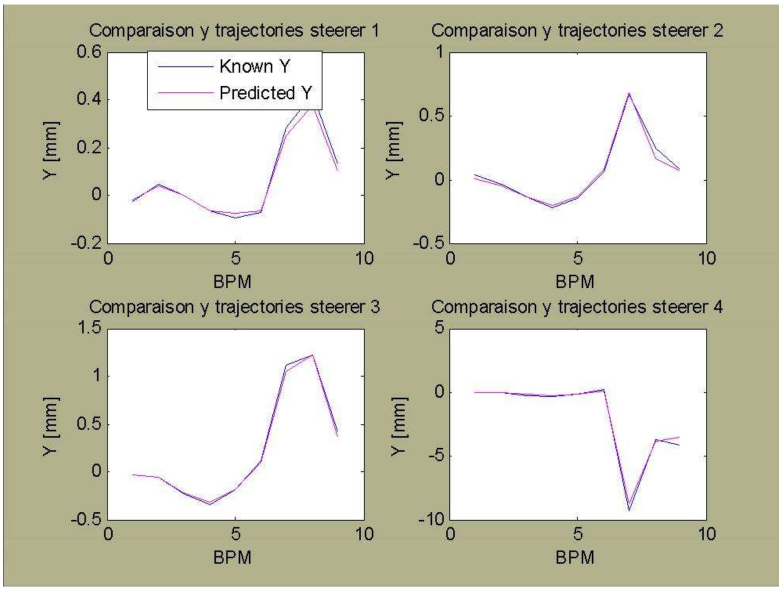

Figure 4.38: Comparison between the vertical trajectories calculated from the predicted temporal eigenvectors and the vectors obtained by SVD analysis. Note again the different scales in the plots.

$$\mathbf{X}_{n,pred} = \mathbf{U}_{n,pred} \cdot \mathbf{S}_n \cdot \mathbf{V}_n \ . \tag{4.13}$$

We choose in this case as well, for our plots, only the value of each vector $\mathbf{U}_{n,pred}$ corresponding to the highest eigenvalue, and the corresponding eigenvector inside the matrix $\mathbf{V}_n$. In Fig. 4.39 the results of this prediction are shown. The term ”Known” indicates here the trajectories obtained by direct SVD of the BPM readings, while the term ”Predicted” refers to the trajectories obtained by using $\mathbf{U}_{n,pred}$, i.g. the matrix estimated from a new set of data multiplied by the coefficient matrix[8]. Note the different scales in the plots. It is clear that more measurements and studies are needed to minimize the residual, for a better resolution, and to achieve such a target we need to have better orthogonality of the beam trajectory. It is important to stress the fact that this measurements had the limit due to a too large

---

[8] from Eqs. 4.12 and 4.13.

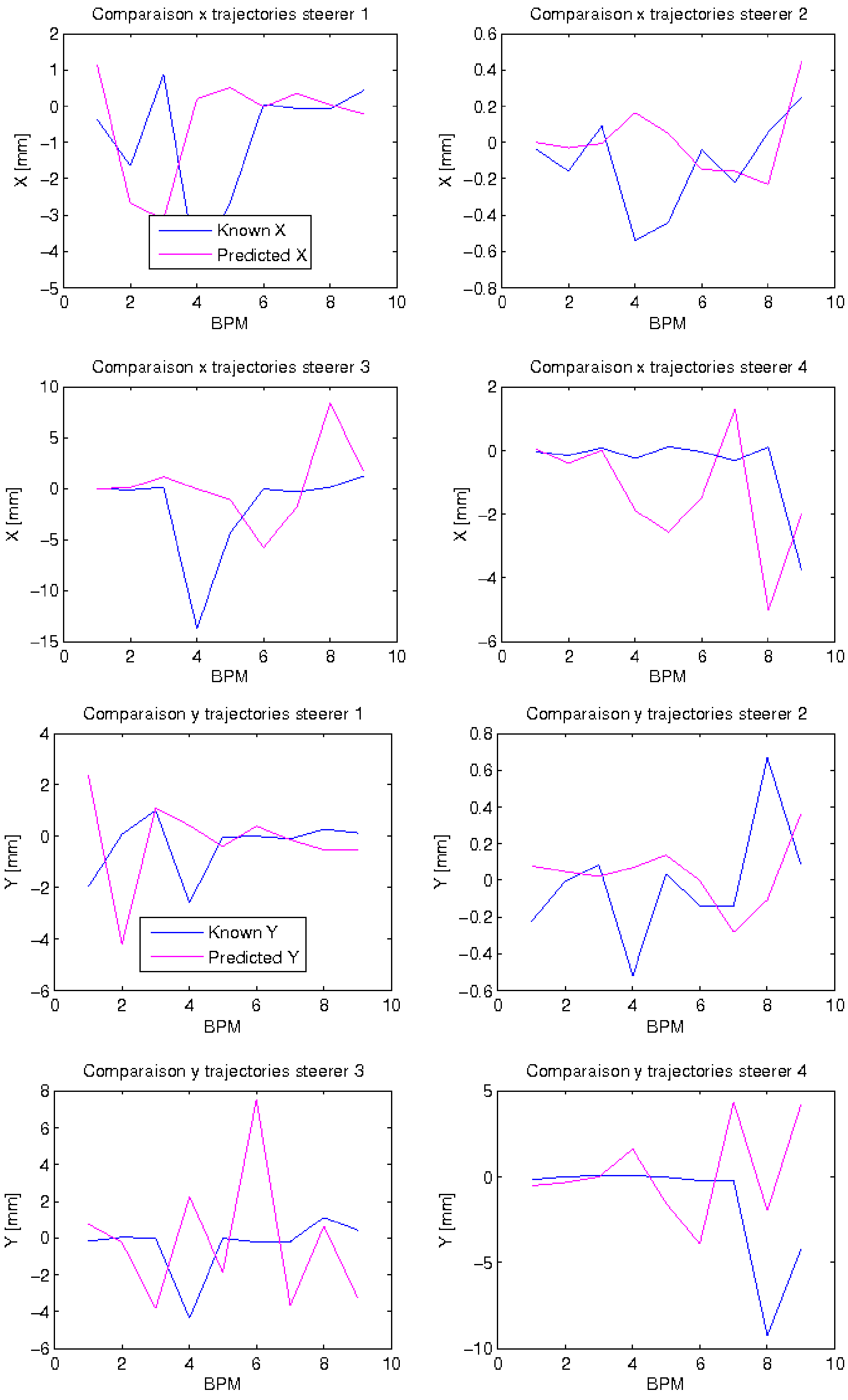

Figure 4.39: Predicted trajectories from a new set of measurements.

corrector resolution, with respect to the size of the scan steps, needed for a more precise analysis; moreover a lot of data points have been dropped from the analyzed data, because of saturated signals. Figs. 4.37 and 4.38 already show a good agreement, giving encouraging results for the application of this procedure.
The corrector power have been recently changed and more measurements, shown in the next section, have given better results, by using the same method of analysis.

Results of latest measurements

New measurements have been made successively and the same procedure has been applied but with finer steerer scans, covering better the (x, x') and (y, y') space., due to a smaller corrector resolution.
The beam was steered in the fourth and fifth modules (ACC4 and ACC5). Approximately 20 runs, of $\sim$ 100 points each were used. In Figs. 4.40 and 4.41 the alignments are plotted with the slope and offset removed to show the relative alignment of the cavities within the module. Different lines correspond to different data set used for the analysis. In ACC4, the rms alignment in x and y was 105 and 215 μm[9], with a measurement reproducibility in x and y of 37 and 24 μm.
In ACC5 the alignment was 241 and 203 μm respectively, with a measurement reproducibility of 9 and 5 μm. Note that the tolerance for cavity alignment is 500 μm rms. The results of this last measurements has been presented to EPAC 2006 and still are developping.

The procedure described in this chapter is the HOM BPM calibration procedure; by knowing the I and Q of the HOMs signal, it is possible to predict the beam position in each cavity. The HOM based cavity alignment measures the relative positions of the axes of the $TE_{111}-6$ dipole modes in

---

[9] Standard Deviation.

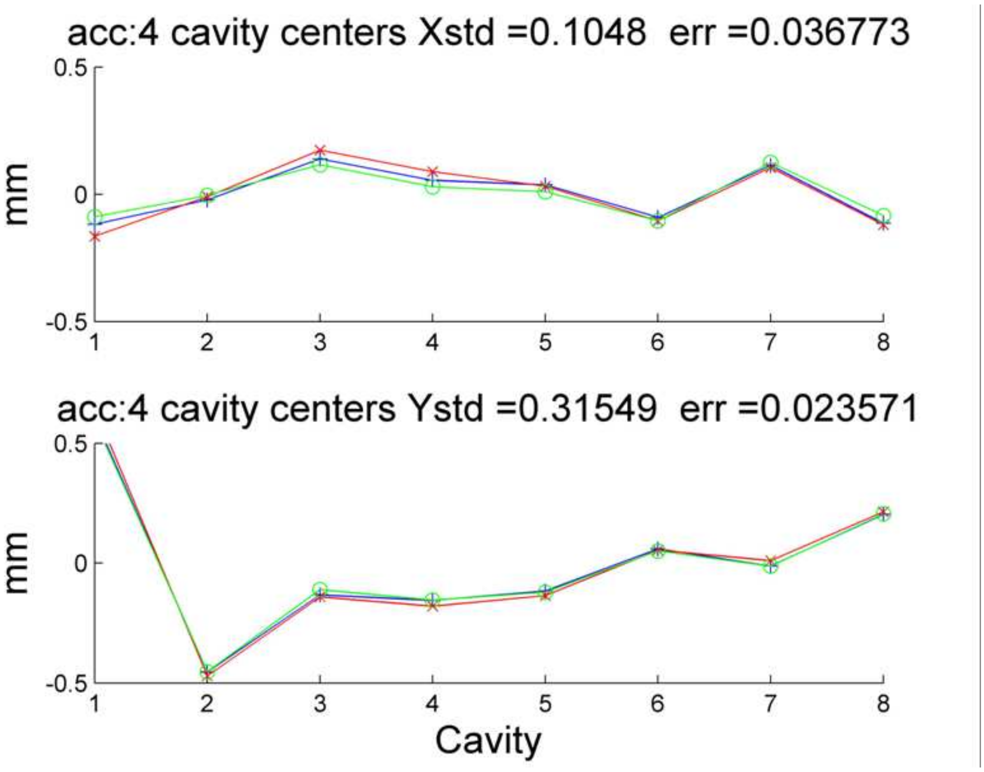

Figure 4.40: Alignment of $TE_{111} - 6$ cavity mode centers in module 4.

the cavities in a module. The dipole mode axes may not be aligned to the mechanical centers of the cavities due to perturbations from couplers, and manufacturing imperfections.

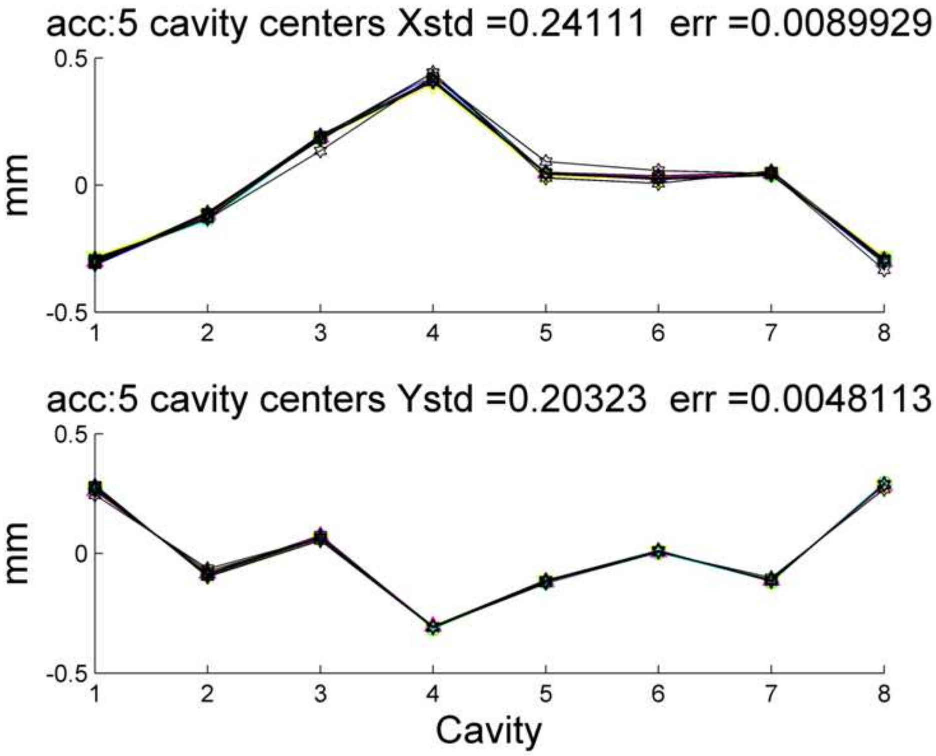

Figure 4.41: Alignment of $TE_{111} - 6$ cavity mode centers in module 5.

Chapter 5

Summary and conclusions

The passage of an electron bunch through a superconducting cavity in addition to coupling to the accelerating mode, excites a spectrum of higher order modes. An analytical study about the electromagnetic fields and the wake fields expansion, in general and in a pill-box cavity in particular, has been carried out; throughout these notes the application of basic physical principles such as energy conservation, superposition and causality have been emphasized, both to provide insight and to simplify certain derivations. An alternative and original method of resolution of the Maxwell's equations have been shown and the results of a Matlab computation of the R/Q characteristic of each mode have been presented.

An experimental program at Tesla Test Facility 2 at DESY has been also described in this thesis. The dipole mode amplitudes contain information on the beam position relative to the cavity, while the monopole modes provide information on the arrival time of the beam. A fully relativistic beam will most strongly excite the cavity modes with near speed of light phase velocities, and we only consider such modes. Dipole modes are also excited by a bunch which traverses the cavity at an angle with amplitude where is the beam angle relative to the mode axis, with a phase 90 degrees from that produced by a position offset. A tilted bunch also excites dipole modes. For the TTF2, the bunch length is sufficiently short that the "tilt" signal is insignificant. The signals from the higher order mode ports on superconducting cavities have been used to do survey structure alignment and to find the cavity eccentricities and misalignment.

A HOM–based diagnostic system has been successively installed to instrument both couplers on each of the 40 superconducting cavities in the DESY TTF2 Linac. The electronics uses a single stage down conversion from the 1.7 GHz HOM spectral line to a 20 MHz IF (intermediate frequency signal) which has been digitized. The electronics was based on low cost surface mount components suitable for large scale production. The response of the HOM modes was calibrated using steerers. The two dipole modes with the strongest coupling to the beam were the TE_{111}–6 and TE_{111}–7. For the HOM dipole experiments the TE_{111}–6, with a frequency of approximately 1.7 GHz was used. The dipole modes including the TE_{111}–6 are doublets, with a frequency splitting caused by the asymmetry in the cavity shape, and by the cavity power coupler. Several TM_{011} monopole lines were used for the HOM monopole experiment. The data described here is from a series of experiments until March 2006. The beam was steered by a large amount ($\sim$1 cm) relative to its nominal orbit, in order to be sure to pass through the centers of the cavities.

For the analysis of monopole and dipole signals first a linear regression analysis has been introduced, giving already a resolution of about 3 μm. Secondly, the Model Independent Analysis (MIA), based on singular value decomposition, has been used. SVD and linear regression were performed using the Matlab function, and the accuracy of the SVD analysis has been revealed by the residual with the linear regression.
Then we have been able to find, by SVD, a set of eigenvalues and eigenfunctions generating orthonormal basis, and effectively average the BPM's with

best correlated appropriate weighting as given by the basis set. Successively, with the correlation coefficients, we have obtained a prediction on the position of the beam. The procedure of using HOMs as BPMs has been then explained and then dipole high order modes have been shown to be usable as beam position monitors with less than 5 μm resolution, expected to improve to less than 1.5 μm and 5 μrad with the removal of input attenuators. The dipole modes also define a cavity "center".

Studies to correlate this center position with externally measured alignments are underway. The HOM experiments on TTF2 have used single bunch beam. For bunch rates not much faster than the HOM mode decay times, bunch by bunch position and phase measurements should be possible in the future. Moreover, the existing broad band HOM diagnostic system can measure the response of all the HOM modes below 2.5 GHz to beam position and angle, and this will allow detailed comparison of cavity simulations.

Appendix A

Introduction to linear regression

Linear regression analyzes the relationship between two variables, X and Y. For each data taking, you know both X and Y and you want to find the best straight line through the data. In some situations, the slope and/or intercept have a scientific meaning. In other cases, you use the linear lines as a standard curve to find new values of X from Y, or Y from X.

The term ”regression”, like many statistical terms, is used in statistics quite differently than it is used in other contexts. The method was first used to examine the relationship between the heights of fathers and sons. The two were related, of course, but the slope is less than 1.0. A tall father tended to have sons shorter than himself; a short father tended to have sons taller than himself. The height of sons regressed to the mean. The term ”regression” is now used for many sorts of curve fitting.

Matlab determines and graphs the best–fit linear regression line, optionally including a 95% confidence interval or 95% prediction interval bands. You may also force the line through a particular point (usually the origin), calculate residuals, calculate a runs test, or compare the slopes and intercepts of two or more regression lines.

In general, the goal of linear regression is to find the line that best predicts Y from X. Linear regression does this by finding the line that minimizes the sum of the squares of the vertical distances of the points from the line.

Note that linear regression does not test whether your data are linear. It assumes that your data are linear, and finds the slope and intercept that make a straight line best fit your data.

A.1 How linear regression works

A.1.1 Minimizing sum–of–squares

The goal of linear regression is to adjust the values of slope and intercept to find the line that best predicts Y from X. More precisely, the goal of regression is to minimize the sum of the squares of the vertical distances of the points from the line. Why minimize the sum of the squares of the distances? Why not simply minimize the sum of the actual distances?

If the random scatter follows a Gaussian distribution, it is far more likely to have two medium size deviations (say 5 units each) than to have one small deviation (1 unit) and one large (9 units). A procedure that minimizes the sum of the absolute value of the distances would have no preference over a line that was 5 units away from two points and one that was 1 unit away from one point and 9 units from another. The sum of the distances (more precisely, the sum of the absolute value of the distances) is 10 units in each case. A procedure that minimizes the sum of the squares of the distances prefers to be 5 units away from two points (sum–of–squares $= 50$) rather than 1 unit away from one point and 9 units away from another (sum–of–squares $= 82$). If the scatter is Gaussian (or nearly so), the line determined by minimizing the sum–of–squares is most likely to be correct.

Sum of squares than is more properly ”the sum of the squared deviations”. Mathematically, it is an unscaled, or unadjusted measure of dispersion.

The distance from any point in a collection of data, to the mean of the data, is the deviation. This can be written as $x(i)- < X >$, where $x(i)$ is the i^{th} data point, and $< X >$ is the estimate of the mean. If all such deviations are squared, then summed, we have the ”sum of squares” for the data.

When more data are added to the collection, the sum of squares will increase, except in unlikely cases such as the new data being equal to the mean. So usually, the sum of squares will grow with the size of the data collection. That is a manifestation of the fact that it is unscaled.
In many cases the degrees of freedom for the statistical analysis of a data collection is the number of data minus one. We write this as $n - 1$, where n is the number of data.
Scaling (also know as normalizing) means adjusting the sum of squares so that it does not grow as the size of the data collection grows. This is important when we want to compare samples of different sizes, such as a sample of 100 values compares to a sample of 20 values. If the sum of squares was not normalized, its value would always be larger for the sample of 100 values than for the sample of 20 values. To scale the sum of squares, we divide it by the degrees of freedom, i.e., calculate the sun of squares per degree of freedom, or variance. Standard deviation is the square root of the variance.
Sum of squares is often abbreviated with the letters SS and his computation involves just inverting a matrix, in fact, in mathematical terms, this method is an optimization techinque to find an approximate solution for a system of linear equations that has no exact solution, and this happens because the number of equations (m) is bigger that the number of variables (n).
We want to find a solution for the ”equation”:

$$A\mathbf{x} \approx \mathbf{b}\ , \tag{A.1}$$

where A is an $m - by - n$ matrix (with $m > n$) and $\mathbf{x}$ and $\mathbf{b}$ are respectively $n-$ and $m-$dimensional column vectors. We want to minimize the *Euclidean norm* squared of the *residual* $A\mathbf{x} - \mathbf{b}$. Therefore the minimizing vector $\mathbf{x}$ is a solution of the **normal equation**:

$$A^T A\mathbf{x} = A^T\mathbf{b}\ , \tag{A.2}$$

and the solution is unique and given by:

$$\mathbf{x} = \left(A^T A\right)^{-1} A^T\mathbf{b}\ . \tag{A.3}$$

The matrix $\left(A^T A\right)^{-1} A^T$ is called *pseudo inverse* of A. We cannot use the true *matrix inverse* of A (that is A^{-1}), because it does not exist as A is not a *square matrix* ($m \neq n$).

A.1.2 Slope and intercept

Matlab reports the best–fit values of the slope and intercept, along with their standard errors and confidence intervals[1].

The slope quantifies the steepness of the line. It equals the change in Y for each unit change in X. It is expressed in the units of the Y–axis divided by the units of the X–axis. If the slope is positive, Y increases as X increases. If the slope is negative, Y decreases as X increases.

The Y intercept is the Y value of the line when X equals zero. It defines the elevation of the line (Fig. A.1).

The standard error values of the slope and intercept can be hard to interpret,

---

[1] i.g. an interval between two numbers, where there is a certain specified level of confidence that a population parameter lies

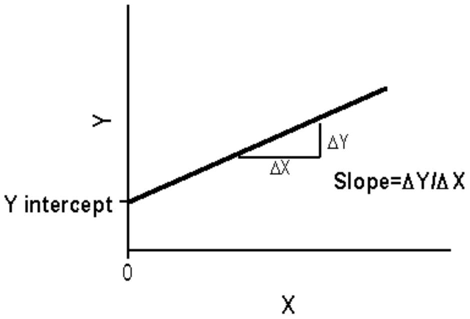

Figure A.1: Linear regression sketch. The slope quantifies the steepness of the line.

but their main purpose is to compute the 95% confidence intervals. If you accept the assumptions of linear regression, there is a 95% chance that the true value of the slope lies within the 95% confidence interval of the slope. Similarly, there is a 95% chance that the true value of the intercept lies within the 95% confidence interval of the intercept.

A.1.3 Goodness-of–fit of linear regression

The value r^2 quantifies goodness of fit; it is a fraction between 0.0 and 1.0, and has no units. An r^2 value of 0.0 means that knowing X does not help you predict Y. There is no linear relationship between X and Y, and the best–fit line is a horizontal line going through the mean of all Y values. When r^2 equals 1.0, all points lie exactly on a straight line with no scatter. Knowing X lets you predict Y perfectly.

r^2 is computed from the sum of the squares of the distances of the points from the best–fit curve determined by linear regression. This sum–of–squares value is called SS_{reg}, which is in the units of the Y–axis squared. To turn r^2 into a fraction, the results are normalized to the sum of the square of the distances of the points from a horizontal line through the mean of all Y values. This values is called SS_{tot}. If the curve fits the data well, SS_{reg} will be much smaller than SS_{tot}.

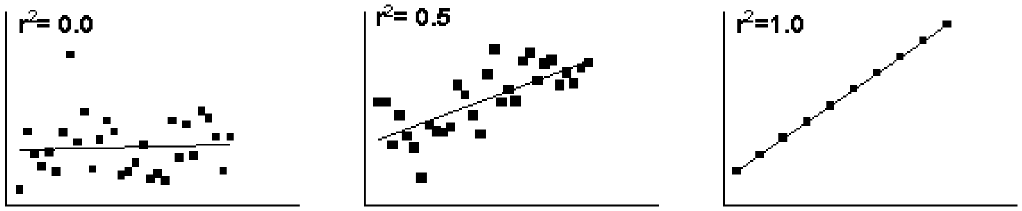

Figure A.2: Residual from regression.

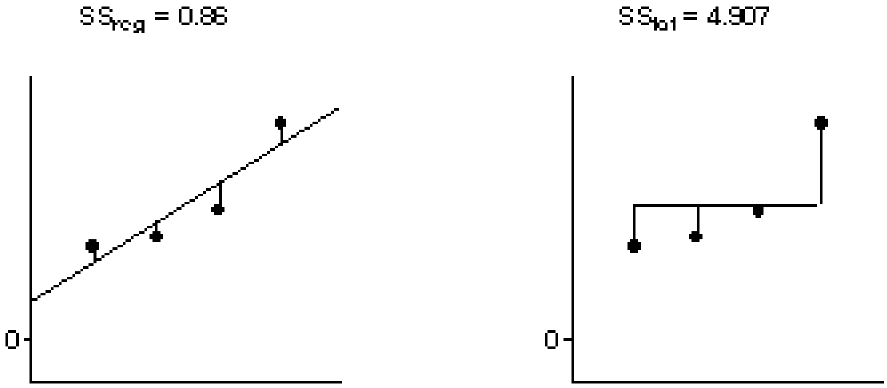

Figure A.3: Matlab computation of r^2.

$$r^2 = 1 - \frac{SS_{reg}}{SS_{tot}} = 1 - \frac{0.86}{4.91} = 0.83 \; . \tag{A.4}$$

Figs. A.2 and A.3 show the best–fit linear regression line. This line minimizes the sum–of–squares of the vertical distances of the points from the line. Those vertical distances are also shown on Fig. A.3. In this example, the sum of squares of those distances (SS_{reg}) equals 0.86. To use this value as a measure of goodness–of–fit, you must compare it to something.

The right half of the figure shows the null hypothesis – a horizontal line through the mean of all the Y values. Goodness–of–fit of this model (SS_{tot}) is also calculated as the sum of squares of the vertical distances of the points from the line, 4.907 in this example. The ratio of the two sum–of–squares values compares the regression model with the null hypothesis model. The equation to compute r^2 is shown in the figure. In this example r^2 is 0.8248. The regression model fits the data much better than the null hypothesis, so SS_{reg} is much smaller than SS_{tot}, and r^2 is near 1.0. If the regression model were not much better than the null hypothesis, r^2 would be near zero.

You can think of r^2 as the fraction of the total variance of Y that is "explained" by variation in X. The value of r^2 (unlike the regression line itself) would be the same if X and Y were swapped [Mot03]. So r^2 is also the fraction of the variance in X that is "explained" by variation in Y. In other words, r^2 is the fraction of the variation that is shared between X and Y.

In this example, 84% of the total variance in Y is "explained" by the linear regression model. That leaves the rest of the variance (16% of the total) as variability of the data from the model (SS_{tot})

Appendix B

Singular Value Decomposition

In linear algebra Singular Value Decomposition (SVD) is an important factorization of a rectangular real or complex matrix, with several applications in signal processing and statistics. In some respect this matrix decomposition is similar to the diagonalization of symmetric or Hermitian matrices using a basis of eigenvectors given by the spectral theorem, but the two decompositions have in general rather different characters and should not be confused even though they are related.

Suppose $\mathbf{M}$ is an m–by–n matrix whose entries come from the field $\mathbf{K}$, which is either the field of real numbers or the field of complex numbers. Then there exists a factorization of the form:

$$\mathbf{M} = \mathbf{U}\mathbf{S}\mathbf{V}^{\mathbf{T}} \,, \tag{B.1}$$

where $\mathbf{U}$ is an m–by–m unitary matrix over $\mathbf{K}$, the matrix $\mathbf{S}$ is m–by–n with nonnegative numbers on the diagonal and zeros off the diagonal, and $\mathbf{V}^T$ denotes the conjugate transpose of $\mathbf{V}$, an n–by–n unitary matrix over $\mathbf{K}$. Such a factorization is called a singular–value decomposition of $\mathbf{M}$.

- ☐ The matrix **V** thus contains a set of orthogonal ”input” or ”analyzing” base–vector directions for **M**
- ☐ The matrix **U** contains a set of orthogonal ”output” base–vector directions for **M**
- ☐ The matrix **S** contains the singular values, which can be thought of as scalar ”gain controls” by which each corresponding input is multiplied to give a corresponding output.

One commonly insists that the values $\mathbf{S_{i,j}}$ be ordered in non–increasing fashion. In this case, the diagonal matrix **S** is uniquely determined by **M** (though the matrices **U** and **V** are not).

B.1 Singular values, singular vectors, and their relation to the SVD

A non–negative real number σ is a singular value for **M** if and only if there exist normalized vectors **u** in $\mathbf{K}^m$ and **v** in $\mathbf{K}^n$ such that:

$$\mathbf{Mv} = \sigma\mathbf{u} \quad \textit{and} \quad \mathbf{M}^T\ \mathbf{u} = \sigma\mathbf{u}\ . \tag{B.2}$$

The vectors **u** and **v** are called *left–singular* and *right–singular* vectors for σ, respectively. In any singular value decomposition $\mathbf{M} = \mathbf{USV}^T$ the diagonal entries of **S** are necessarily equal to the singular values of **M**. The columns of **U** and **V** are left– resp. right–singular vectors for the corresponding singular values. Consequently, the above theorem states that

- An $m \times n$ matrix **M** has at least one and at most $p = min(m, n)$ distinct singular values.

- It is always possible to find a unitary basis for $\mathbf{K}^m$ consisting of left–singular vectors of $\mathbf{M}$.
- It is always possible to find a unitary basis for $\mathbf{K}^n$ consisting of right–singular vectors of $\mathbf{M}$.

A singular value for which we can find two left (or right) singular vectors that are not linearly dependent is called *degenerate*.

Non–degenerate singular values always have unique left and right singular vectors, up to multiplication by a unit phase factor $e^{i\phi}$ (for the real case up to sign). Consequently, if all singular values of $\mathbf{M}$ are non–degenerate and non–zero, then its singular value decomposition is unique, up to multiplication of a column of $\mathbf{U}$ by a unit phase factor and simultaneous multiplication of the corresponding column of $\mathbf{V}$ by the same unit phase factor.

Degenerate singular values, by definition, have non–unique singular vectors. Furthermore, if $\mathbf{u}_1$ and $\mathbf{u}_2$ are two left–singular vectors which both correspond to the singular value σ, then any normalized linear combination of the two vectors is also a left singular vector corresponding to the singular value σ. The similar statement is true for right singular vectors. Consequently, if $\mathbf{M}$ has degenerate singular values, then its singular value decomposition is not unique.

B.2 Relation to eigenvalue decomposition

The singular value decomposition is very general in the sense that it can be applied to any $m \times n$ matrix. The eigenvalue decomposition, on the other hand, can only be applied to (certain classes of) square matrices. Nevertheless, the two decompositions are related.

In the special case that $\mathbf{M}$ is a *Hermitian* matrix which is positive semi–definite, i.e., all its eigenvalues are real and non–negative, then the singular values and singular vectors coincide with the eigenvalues and eigenvectors of $\mathbf{M}$,

$$\mathbf{M} = \mathbf{V}\boldsymbol{\Lambda}\mathbf{V}^T \ . \tag{B.3}$$

More generally, given an SVD of $\mathbf{M}$, the following two relations hold:

$$\begin{aligned} \mathbf{M}^T\,\mathbf{M} &= \mathbf{V}\mathbf{S}^T\,\mathbf{U}^T\,\mathbf{U}\mathbf{S}\mathbf{V}^T\ = \mathbf{V}(\mathbf{S}^T\,\mathbf{S})\mathbf{V}^T \\ \mathbf{M}\mathbf{M}^T\ &= \mathbf{U}\mathbf{S}\mathbf{V}^T\,\mathbf{V}\mathbf{S}^T\,\mathbf{U}^T\ = \mathbf{U}(\mathbf{S}\mathbf{S}^T\ )\mathbf{U}^T \end{aligned} \tag{B.4}$$

The right hand sides of these relations describe the eigenvalue decompositions of the left hand sides. Consequently, the squares of the non–zero singular values of $\mathbf{M}$ are equal to the non–zero eigenvalues of either $\mathbf{M}^T\,\mathbf{M}$ or $\mathbf{M}\mathbf{M}^T$. Furthermore, the columns of $\mathbf{U}$ (left singular vectors) are eigenvectors of $\mathbf{M}\mathbf{M}^T$ and the columns of $\mathbf{V}$ (right singular vectors) are eigenvectors of $\mathbf{M}^T\mathbf{M}$.

B.3 Geometric meaning

Because $\mathbf{U}$ and $\mathbf{V}$ are unitary, we know that the columns $\mathbf{u}_1, ..., \mathbf{u}_m$ of $\mathbf{U}$ yield an orthonormal basis of $\mathbf{K}^m$ and the columns $\mathbf{v}_1, ..., \mathbf{v}_n$ of $\mathbf{V}$ yield an orthonormal basis of $\mathbf{K}^n$ (with respect to the standard scalar products on these spaces).

The linear transformation $T : \mathbf{K}^n \rightarrow \mathbf{K}^m$ that takes a vector $\mathbf{x}$ to $\mathbf{M}\mathbf{x}$ has a particularly simple description with respect to these orthonormal bases: we have $T(\mathbf{v}_i) = \sigma_i\mathbf{u}_i$, for $i = 1, ..., min(m, n)$, where σ_i is the i^{th} diagonal entry of $\mathbf{S}$, and $T(\mathbf{v}_i) = 0$ for $i > min(m, n)$.

The geometric content of the SVD theorem can thus be summarized as follows: for every linear map $T : \mathbf{K}^n \rightarrow \mathbf{K}^m$ one can find orthonormal bases of $\mathbf{K}^n$ and $\mathbf{K}^m$ such that T maps the i^{th} basis vector of $\mathbf{K}^n$ to a non–negative multiple of the i^{th} basis vector of $\mathbf{K}^m$, and sends the left–over basis vectors to zero. With respect to these bases, the map T is therefore represented by a diagonal matrix with non–negative real diagonal entries.

Bibliography

[Bab01] N. Baboi, *Studies on Higher Order Modes in Acelerating Structures for Linear Colliders*, DESY–THESIS–2001–052 (2001).

[Ban83] K. Bane, T. Weiland, SLAC/AP–1 (1983).

[Ban85] K.L.F. Bane, P.B. Wilson, *Physiscs of High–Energy Particle Accelerators*, AIP Conf. Proc. No.127 (1985).

[Bri97] R. Brinkmann, G. Materlick, J. Rossbach and A. Wagner Editors, *TESLA Conceptual Report*, DESY 1997–048 (1997).

[Bri01] R. Brinkmann, K. Flöttmann, J. Rossbach, P. Schmüser, N. Walker and H. Weise (eds.), *TESLA. The Superconducting Electron–Positron Linear Collider with an Integrated X–Ray Laser Laboratory.* Technical Design Report, Part II: *The Accelerator*, DESY Report: DESY 2001–011, ECFA 2001–209, TESLA Report 2001–23, TESLA–FEL 2001–05(2001).

[Bry92] P.J. Bryant, *Beam Transfer Lines*, CERN ACCELERATOR SCHOOL, CERN-94-01-V-1, Finland (1992).

[Buo92] J. Buon, *Beam Phase Space an Emittance*, in Proc. CERN Accelerator School, University of Jyväskylä, Finland, p.89(1992).

[Bur94] B. Burke for the FFTB Collaboration, *Results from the Final Focus Test Beam*, Proc. 4^{th} EPAC, London (1994), Vol. I, p. 23.

[Cha75] A.W. Chao, P.L. Morton, PEP–105, SLAC (1975).

[Cha93] A. Chao, *Physiscs of Collective Beam Instabilities in High Energy Accelerators*, Wiley (1993).

[Che91] P.Chen and K. Yokoya, *Beam-Beam Phenomena in Linear Collider*, KEK–report 91–2,(1991).

[Chm65] E. Chambers, *Stanford High Energy Physics Laboratory Report* (1965).

[Far99] S. Fartoukh at al., *Evidence for a Strongly Coupled Dipole Mode with Insufficient Damping in TTF First Accelerating Module*, PAC Conf. Proc. (1999).

[Faa02] B. Faatz for the FEL team, *The SASE FEL at the TESLA Test Facility as User Facility*, FEL 2002 Proceedings, Argonne (2002).

[Mon85] A.A. Mondelli et al., *Frequency scaling of RF linacs*, Nuclear Science, Vol. NS 32, No.5 (1985).

[Mot03] H. Motulsky, A. Christopoulos, *Fitting Models to Biological Data using Linear and Nonlinear Regression*, GraphPad (2003).

[Irw99] J. Irwin et al., *Model–independent beam dynamics analysis*, Phys. Rev. Lett. 82, 1684 (1999).

[Jac75] Jackson, *Classical Electrogynamics*, 2nd. Ed., p.818 (1975).

[Jac02] David J. Jackson, Dong Su, and Fred J. Wickens, *Internal alignment of the SLD vertex detector using a matrix singular value decomposition technique*, Nucl. Instrum. Meth., A491:351–365, SLAC–PUB–90092 (2002).

[Lie01] M.U. Liepe, *Superconductiong Multicell Cavities for Linear Colliders*, (2001) Hamburg: DESY.

[Mor69] P. Morse, H. Feshbach, *Methods of Theoretical Physics*, McGraw–Hill, New York (1953).

[Mul88] G. Müller, Proc. 3^{rd} Workshop on RFSuperconductivity, ANL–PHY–88–1, edited by K.W. Shepard, Argonne, USA,p. 331(1988).

[Pal94] L. Palumbo, V.G. Vaccaro, M. Zobov, *Wake Field and Impedance*, LNF-94/041(P) (1994).

[Rau91] T. Raubenheimer, *The Generation and Acceleration of Low Emittance Flat Beams for Future Linear Collider*, PhD Thesis at the Stanford University, California, USA; SLAC Report: SLAC-387 (1991).

[Rei93] J.R. Reitz, F.J. Milfort, R.W. Christy, *Foundations of Electromagnetic Theory*, p.365 (1993).

[Ros92] J. Rossbach,*Basic Course on Accelerator Optics*, in Proc. CERN Accelerator School, University of Jyväskylä, Finland, p.17(1992).

[Ros03] M. Ross, et al. *RF Cavity BPM's as Beam Angle and Beam Correlation Monitors*, PAC 2003, Portland OR.

[Sla50] J.C. Slater *Microwave Electronics*, D. Van Nostrand Company, Princeton, (1950).

[Ten03] P. Tenenbaum, *Fields in Waveguides – a Guide for Pedestrian*, USPAS lectures, June 2003, Santa Barbara.

[Wat58] D. Watkins, *Topics in Electromagnetic Theory*, John Wiley and Sons, New York (1958).

[Wan01] R. Wanzenberg, *Monopole, Dipole, and Quadrupole Passbands of the TESLA 9–cell Cavity*, TESLA report 2001–33 (2001).

[Wei81] T. Weiland, B. Zotter, *Particle Accelerators*11, 143 (1981).

[Wie93] H. Wiedeman, *Particle Accelerator Physics*, Vol.I, Springer-Verlag, Berlin Heidelberg, Germany (1993).

Acknowledgments

Now is the time to look back over the last three years and the people close to me who have helped and supported me.

First, I'd like to thank Jacques Payet and Olivier Napoly and their families, who made me so welcome during my first weeks in Paris. I should also like to thank all my friends and colleagues at CEA/Saclay and the secretary, Éliane Cotteverte, for their companionship and help; everyone in the DAPNIA/LEDA group; my team-mates from the two CEA volleyball tournaments with whom I had so much fun; Véronique Masse, Maria Durante and Julien Tajeb for their friendship and the encouragement they gave me in difficult moments.

Once settled into work and the French way of life, I met a lot of people at CEA and DESY and here I must give mention to my supervisors, Olivier Napoly (this time for his professional support) and Reinhard Brinkmann, and all my colleagues from the DESY/MPY-MDI groups, and give special thanks to Nicoleta Baboi, my professional guide throughout my PhD thesis.

This thesis was the result of experimental work made in collaboration with SLAC and FERMILAB, where I would like to give particular thanks to Marc Ross, who taught me so much about analysis, and who stimulated my enthusiasm for studying and discovery, and to Joe Frisch, Tony Smith, Douglas McCormik, Stephen Molloy, Justin May, Linda Hendrickson, Nathan Eddy, Sergei Nagaitsev, and all the countless others whose names are on the tip of my tongue.

During my life at DESY, I've met a lot of new friends, from Italy and the rest of the world. They helped me to relax, to have fun and to discover Hamburg by day and night.

I've greatly enjoyed my time with the HERMES crew, especially the HERMES TARGET group, Paolo Lenisa with his anecdotes about Russia and Russian culture, Davide Reggiani and his wife, Riccardo Fabbri, all the Ferrara INFN target group, Pasquale Di Nezza, Ignazio Vilardi, and finally Erika Garutti and Marius Groll (also for the "Zaira and house plants sitting"!).

I would not have had the chance to be here and know all these wonderful people without the help and support of my family, so… *grazie papà, mamma e Emanuele.*

A big thank you to Diego Gamba and to Werner Herr for their encouragement and constant moral support and help.

I must also mention all the CAS crew for their informative lectures, and for giving me the opportunity to know MarCo; Barbara Preger, Tatania Pieloni and Peder Eliasson, and all my course-mates for the fun we had together in Baden and Trieste.

To the Capiluppi family I would like to extend my thanks for their friendship and warmth over the last two years.

I must also thank Nicholas Lusty for his help correcting my English and always supporting me materially and morally.

And last, but not least, I would like to thank my great love, my guide, my shining example, my pride, the person with whom I hope to see every sunrise and sunset for the rest of my life, my sweet dream, MarCo, for his help, his support and his love.

We acknowledge the partial support of the European Community-Research Infrastructure Activity under the FP6 "Structuring the European Research Area" programme (CARE, contract number RII3-CT-2003-506395)